Universidade de São Paulo
Instituto de Física

O papel das Teorias de Campo Efetivas na procura da física além do Modelo Padrão

Martín Dionisio Arteaga Tupia

Orientador: Prof. Dr. Enrico Bertuzzo

Tese de doutorado apresentada ao Instituto de Física como requisito parcial para a obtenção do título de Doutor em Ciências.

Banca Examinadora:

Prof(a). Dr(a). Enrico Bertuzzo - Orientador (IFUSP)

Prof(a). Dr(a). Oscar José Pinto Éboli (IFUSP)

Prof(a). Dr(a). Nicolás Bernal (Universidad Antonio Nariño)

Prof(a). Dr(a). Ricardo D'Elia Matheus (IFT UNESP)

Prof(a). Dr(a). Celso Chikahiro Nishi (UFABC)

São Paulo

2021

FICHA CATALOGRÁFICA
Preparada pelo Serviço de Biblioteca e Informação
do Instituto de Física da Universidade de São Paulo

Arteaga Tupia, Martin Dionisio

O papel das teorias de campo efetivas na procura da física além do modelo padrão. São Paulo, 2021.

Tese (Doutorado) – Universidade de São Paulo. Instituto de Física. Depto. de Física Matemática.

Orientador: Prof. Dr. Enrico Bertuzzo
Área de Concentração: Física de Partículas

Unitermos: 1. Física de partículas; 2. Física de alta energia; 3. Física teórica.

USP/IF/SBI-040/2021

University of São Paulo
Physics Institute

The role of Effective Field Theories in the search for Beyond Standard Model physics

Martín Dionisio Arteaga Tupia

Supervisor: Prof. Dr. Enrico Bertuzzo

Thesis submitted to the Physics Institute of the University of São Paulo in partial fulfillment of the requirements for the degree of Doctor of Science.

Examining Committee:

Prof. Dr. Enrico Bertuzzo - Supervisor (IFUSP)

Prof. Dr. Oscar José Pinto Éboli (IFUSP)

Prof. Dr. Nicolás Bernal (Universidad Antonio Nariño)

Prof. Dr. Ricardo D'Elia Matheus (IFT UNESP)

Prof. Dr. Celso Chikahiro Nishi (UFABC)

São Paulo

2021

Para *Mamita*.

Acknowledgements

I would like to thank to my advisor, Dr. Enrico Bertuzzo, because without his guidance it would have been impossible to achieve the results of the present research. I am also grateful to the Particle Physics Group of **IFUSP** for all the knowledge gained with the discussions in the seminars.

I would like to give my deep and sincere gratitude to my family for their continuous and unparalleled love, help and support. I am grateful to my sister Fiorella, for always being there for me as a friend. I am forever indebted to my parents Juana and Dionisio, for giving me the opportunities and experiences that have made me who I am. I am also grateful to my grandmother Isidora, who would have been loved to be here to share together the end of this adventure. I would also like to give a special thanks to: Homeira, Gustavo, Silvia, Irving, Giuliana, Ana Rocío, Yugo, Lisandra, Joseph, Ana Luiza, and Fernando for their invaluable support whenever I needed.

Finally, this work was supported by **CNPq** (Conselho Nacional de Desenvolvimento Científico e Tecnológico) under contract 140884/2017-3/CNPq.

Abstract

In this work we explore some uses of effective field theories (EFT's) to shed some light on modern problems in high energy physics, such as neutrino masses, dark matter/dark sectors and the hierarchy problem. In particular, we will analyze the problem of the detection of cosmic background neutrinos (and how the presence of physics beyond the standard model can affect it), the renormalization group properties of dark sectors that communicate with the standard model via mediators that carry a flavor charge and, finally, the gravitational imprints of a candidate to solve the hierarchy problem, the relaxion.

Keywords: Effective Field Theory, Cosmic Neutrino Background, Dark Sectors, Hierarchy Problem, Gravitational Waves.

Resumo

Neste trabalho exploramos alguns usos das teorias efetivas de campos (EFT's) para dar alguma luz sobre problemas modernos na física de altas energias, tais como as massas dos neutrinos, a matéria escura e os setores escuros. Em particular, vamos analisar o problema da detecção do fundo cósmico de neutrinos (e como a presença da física além do modelo padrão pode afetá-lo), as propriedades do grupo de renormalização dos setores escuros que se comunicam com o modelo padrão via mediadores que carregam uma carga de sabor e, finalmente, os sinais gravitationais de um candidato a resolver o problema da hierarquia, o relaxion.

Palavras-chaves: Teorias Efetivas de Campos, Fundo Cósmico de Neutrinos, Setores Escuros, Problema da Hierarquia, Ondas Gravitacionais.

Contents

Publications

As part of the doctoral program I did research in different areas of high energy physics: neutrino physics, dark sectors, the hierarchy problem and gravitational waves. The research produced the following publications:

1. M. Arteaga, E. Bertuzzo, Y. F. Perez-Gonzalez, and R. Zukanovich Funchal, *Impact of Beyond the Standard Model Physics in the Detection of the Cosmic Neutrino Background*, JHEP, vol. 09, p. 124, 2017.

2. M. Arteaga, E. Bertuzzo, C. Caniu Barros, and Z. Tabrizi, *Operators from flavored dark sectors running to low energy*, Phys. Rev., vol. D99, no. 3, p. 035022, 2019.

3. D. Barducci, E. Bertuzzo, M. Arteaga, *Gravitational tests of electroweak relaxation*, arXiv 2011.05795, 2020. Accepted by JHEP.

Chapter 1

Introduction

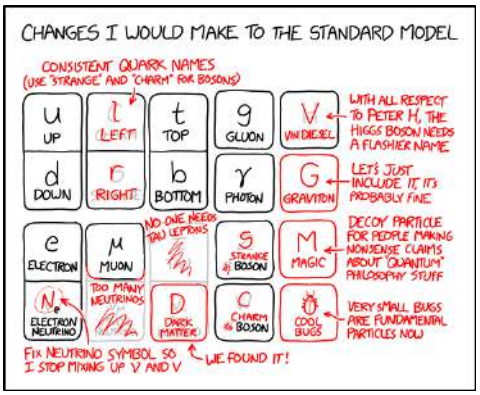

Credits to Ref. [1].

So far, the best known description of the universe at the microscopic level is given by the Standard Model of Particle Physics (abbreviated SM) which is a gauge theory based on the gauge group $SU(3)_c \times SU(2)_L \times U(1)_Y$. Despite the fact that it does not take into account the gravity sector, it describes *almost* all the high energy physics phenomena that we know until a few TeV.

However, there are some high energy phenomena that do not have a satisfactory explanation in the framework of the SM. Additionally, there are also theoretical problems that escapes from the scope of the explanations given by the SM. In this context, the following quote, by Gripaios in Ref.[2], "*There must be something, but we don't know what it is!* " seems to be very appropriate to describe the current situation of Particle physics. Between the many interesting phenomena that are not explained by the SM, we will focus on the following three:

1. Neutrino masses, and their properties;
2. Existence of Dark Matter/Dark Sectors;
3. the Hierarchy problem.

Models that extend the theoretical framework of the SM trying to explain phenomena as the ones listed above are called Beyond the Standard Model theories (BSM) [2; 3; 4; 5; 6]. In

order to deal, in a model independent way, with the problems mentioned above we shall use the effective field theory approach (EFT).

In Chapter 2 we introduce the basics of the EFT approach. This framework will be fundamental for the analysis of subsequent Chapters. We choose to present the EFTs by first introducing the Appelquiest-Carrazone theorem and through the classical example of Fermi theory. This theory was originally postulated by E. Fermi in 1933 [7; 8; 9] in order to give an explanation to the beta decay process. After studying a toy model version of Fermi theory, we extend the main ideas learned to construct a more general structure. This structure will be identified as the EFT approach.

In Chapter 3 we consider the following question: if neutrinos have new BSM interactions, how would this affect the relic neutrino detection? In order to answer that question, we allow for non-standard interactions in the lagrangian at the weak scale. Such terms are described by an EFT in which we consider dimension six-operators that are $SU(2)_L \times U(1)_Y$ invariant, including also right-handed neutrinos and neutrino masses. The analysis of the detection of the relic neutrinos is done by studying their capture on tritium in a PTOLEMY-like detector (Princeton Tritium Observatory for Light, Early-Universe, Massive-Neutrino Yield) [10; 11]. In the first part of the chapter we introduce some useful concepts and relations from Cosmology and Particle physics, and also discuss the PTOLEMY experiment. In the last part of the chapter we instead describe how the presence of new interactions may affect the detection of the cosmic neutrino background.

Chapter 4 is devoted to the analysis of generic dark sectors, their interaction with the SM and their running to low energies. In recent years, dark sectors have become more relevant in high energy physics, since null results from LHC and other experiments motivate the search for new unconventional signatures. Another reason why dark sectors have attracted much attention is their implicit presence in dark matter (DM) models. In order to be as model independent as possible our focus will be on a generic dark sector communicating with the SM via an unspecified heavy and flavorful mediator, X. The effects of the renormalization group flow on the Wilson coefficients are computed and as expected they have a non-trivial impact in the theory. The first part of the chapter is focused on developing the formalism of

effective field theory needed for posterior analysis and computation. We finalize the chapter by presenting our results for the RGE's of the operators.

Chapter 5 studies the possible gravitational wave signal associated with the condensation of a dark strong sector that generates the relaxion potential. The relaxion mechanism is a possible solution to the hierarchy problem. In contrast to previous solutions such as supersymmetry or extradimensions, the relaxion solves the hierarchy problem by dynamical evolution. We also study how a second phase of rolling induced by reheating could affect the performance of the mechanism to solve the hierarchy problem. At the end of this chapter we analyse the GW signatures of this model. For this we consider the detectability region of various near-future experiments.

In Chapter 6, we finally present our conclusions.

Chapter 2

Effective Field Theory

Based on "Effective Field Theory for Turtles" by Quantum Diaries [12].

2.1 Introduction

One of the most interesting facts about our universe is our ability to explain the phenomena occurring in nature through the use of physical models. However, all the known physical models have an intrinsic range of validity. Perhaps the best known example is the comparison between quantum mechanics and general relativity. While quantum mechanics is used to study micro-phenomena, general relativity is appropriate to study macroscopic phenomena. Obviously, this is a very rough description, as there are many other technical differences; nevertheless, the point is that each model is valid only for a finite energy (or scale) regime.

During the evolution of particle physics we learned that, as we go to smaller and smaller scales, new particles usually appear at some particular energies. This means that, before the appearance of such a new particles, we can use an *effective* theory that is valid up to a cutoff scale Λ_c, and for energies beyond that cutoff those new particles appear. That effective theory would be a simplified model of a more fundamental description. By depending on the energy range that we are interested in, that fundamental theory could be either perturbative or non-perturbative. Two examples: the electroweak theory, which is a perturbative model and QCD that is perturbative at scales higher than $\sim$ 200 MeV, but non-perturbative for

lower energies. Independent on the perturbative nature of the model, there is an important theorem that tell us what is the effect of the higher degrees of freedom once we go to the simplified effective description, this is the Appelquist-Carazzone theorem [13].

The structure of the chapter is as follows: due to its importance in Section 2.2 we first introduce the Appelquist-Carazzone decoupling Theorem. Section 2.3 is devoted to the study of the effective description of perturbative models. Finally, in Section 2.4 the sigma model is introduced as an effective description of non-perturbative theories.

2.2 The Appelquist-Carazzone Decoupling Theorem

The Decoupling Theorem states that in a renormalizable quantum field theory with different mass scales, the only role played by the heavy fields at low-momentum is to contribute to the coupling constant and field strength renormalization [13]. In other words, at low momentum the only relevant degrees of freedom are the light fields.

In their original paper T. Appelquist and J. Carrazzone [13] used a non-abelian gauge theory coupled to a heavy massive fermionic field. This is done in order to prove the theorem in a concrete case, but the validity of the theorem is general [13].

Following the same purpose, in this section we reproduce the argument given in Ref.[13].

The Lagragian choosen to work with is

$$\mathcal{L} = -\frac{1}{4} F_{\alpha\rho\nu} F_{\alpha}^{\rho\nu} - i\overline{\Psi}\gamma_{\rho} D^{\rho}\Psi - m\overline{\Psi}\Psi \tag{2.1}$$

where $F_{\alpha}^{\rho\nu}$ is the field strength tensor, ρ, ν are Lorentz indices and α is a flavor index. By working in the Ladau gauge, the renormalization group equations of the coupling g in this theory and for general momentum k is

$$g_k \equiv g_k \left(\frac{k^2}{\mu^2}, \frac{m^2}{\mu^2}, g_\mu \right), \tag{2.2}$$

where μ is the renormalization scale, and for $k = \mu$ we have the renormalization condition

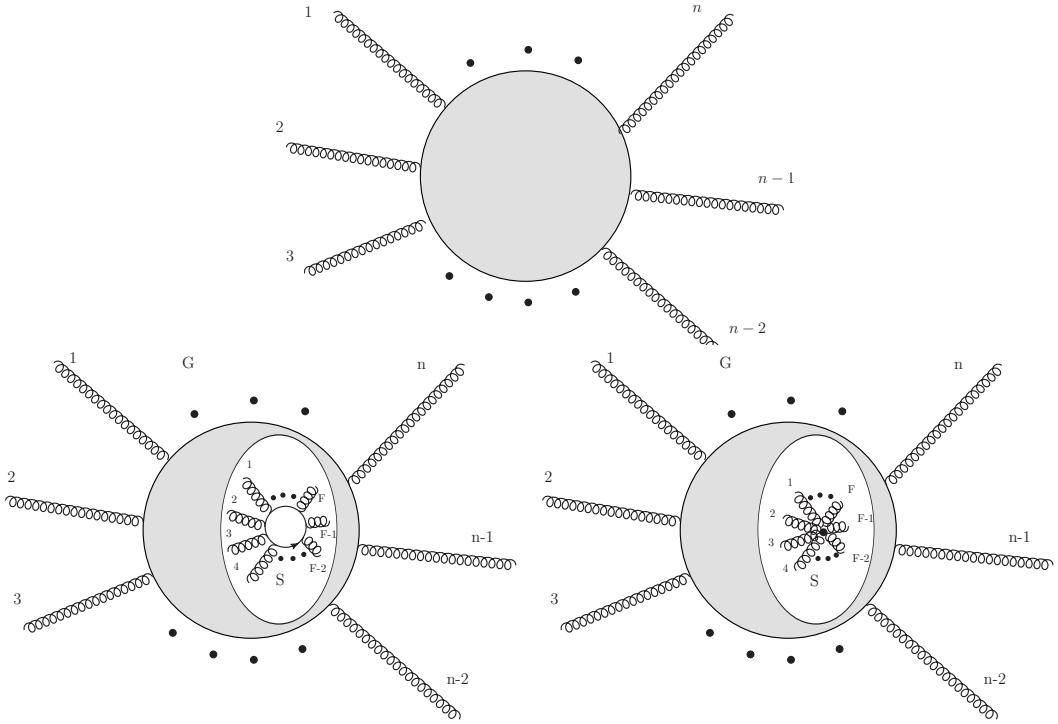

Figure 2.1: 1PI Feynman graphs with n external legs used in the present section. (Top) Graph containing no fermion lines. (Bottom-left) Graph containing fermion lines inside. (Bottom-right) Graph where fermion loops were shrunk to a point, $m \to \infty$ [13].

$g_k(1, m^2/\mu^2, g_\mu) = g_\mu$. Eq.(2.2) satisfies

$$\beta\left(\frac{m^2}{k^2}, g_k\right) = k^2 \frac{\partial g_k}{\partial k^2} \tag{2.3}$$

For the subsequent analysis, we consider arbitrary 1PI Feynman graph with n external legs, see Fig.2.1. To begin with let us consider $n \geq 5$. If the graph contains no divergent subgraphs, the degree of divergence is $d = 4 - n$. Hence, if there are no fermion lines inside the graph and external momenta are of order k, the amplitude of the graph is

$$\mathcal{A} \sim k^{4-n}. \tag{2.4}$$

For $k \ll m$, we now consider the case where there are internal fermion lines inside the graph.

Suppose that any fermion loop inside the graph can be severed by cutting F vector lines, see Fig.2.1. We also define that f is the *minimum* number of severings required. The analysis is separated in two cases: $f \geq n$ and $f < n$. In the former case, the subgraph S containing the fermion loop behaves like m^{4-F} as m goes to infinity. The last limit of $m \to \infty$ is equivalent to shrinking S to a point, see Fig.2.1. In this reduced graph the degree of divergence is $F-n$. Since $f \geq n$, $F-n$ is the maximum degree of divergence in the graph. Therefore, for $k \ll m$ the behavior of the entire graph is

$$\mathcal{A} \sim m^{4-F} m^{F-n} = m^{4-n}. \tag{2.5}$$

This amplitude is strongly suppressed with respect to Eq.(2.4).

The second case, $f < n$, is similar. Here, f severings are needed to separate the fermion loop. Therefore, the graph containing the fermion loop behaves like m^{4-f}. However, the graph in the limit $m \to \infty$ behaves like k^{f-n}. And the entire graph has the amplitude behaving like

$$m^{4-f} k^{f-n} = k^{4-n} \left(\frac{m}{k}\right)^{4-f} \ll k^{4-n}, \tag{2.6}$$

since $f \geq 5$.

In the case of $n = 2$ and $n = 3$, the degree of divergence is reduced to zero by appealing to the transverse structure of the propagator and the tensor structure of the three-point vertex [13]. Together with any graph there is a set of counterterms that reduce further the degree of divergence to -1. Since the subtractions are evaluated at a scale $\mu \ll m$, the cut-off momentum is also small compared to m. As in Eq.(2.4), for comparison purposes, the amplitude without internal fermions behaves like k^{4-n}, up to logarithms as noted in Ref.[13]. The analysis of graphs with internal fermions follows the same line as before. In the regime $k \ll m$, if $F \leq 4$ the behavior of the subgraphs containing the fermion lines together with their counterterms is

$$\mathcal{A} \sim k^{4-F} \times \mathcal{O}(\frac{k}{m}, \frac{\mu}{m}). \tag{2.7}$$

We note that the first factor has no n dependence, this follows from the use of the transversal-

ity of he propagator and the tensor structure of the three-point function. The second factor follows from the counterterms $\left[\log\frac{\Lambda}{m}+\mathcal{O}(\frac{k}{m})\right]-\left[\log\frac{\Lambda}{m}+\mathcal{O}(\frac{\mu}{m})\right]=\mathcal{O}(\frac{k}{m},\frac{\mu}{m})$.

Therefore, the low energy observables behave as if the heavy field are being omitted. A consequence of the decoupling theorem is that the beta function of the theory will be reduced to the pure Yang-Mills beta function as $k \ll m$ [13]

$$\beta\left(\frac{m^2}{k^2}, g_k\right) \xrightarrow[(\frac{\mu^2}{m^2}),(\frac{k^2}{m^2})\to 0]{} \beta_{\mathrm{YM}}(g_k). \tag{2.8}$$

There are two other important examples of the application of these ideas: Fermi theory and the sigma model [13]. Fermi's phenomenological model had a great relevance in giving support to the effective approach. We talk about this model in the following section. We postpone the discussion of the sigma model to the subsequent section.

2.3 EFTs: Perturbative models

2.3.1 Fermi theory

E. Fermi in 1933 and 1934 [7; 8; 9] first proposed a theory to explain the beta-decay. The beta-decay is a process in which a neutron transforms into a proton with the emission of an electron and an antineutrino, $n \to p + e^- + \overline{\nu}_e$. His theory posits the direct interaction between four fermions: neutron, electron, proton and antineutrino. Therefore, for the description of the Fermi theory as a realistic model of interacting particles, one needs to specify the type of fermions involved in the computations.

However, we are interested only in the general idea behind Fermi theory. To this end, let us consider the following toy-model. In the UV, we have a renormalizable theory of a fermion (ψ) and a scalar field (ϕ). Such a theory has lagrangian $\mathcal{L}_{\mathrm{UV}}$ with a Yukawa term

$$\mathcal{L}_{\mathrm{UV}} \supset -\lambda\,\phi\,\overline{\psi}\,\psi. \tag{2.9}$$

This term defines the vertex interaction between scalar and fermions. In the language of Feynman diagrams, it defines the vertex showed in Fig. 2.2. Now, as we go to lower scales,

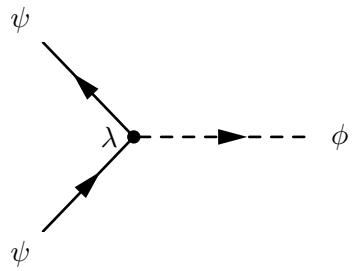

Figure 2.2: Feynman diagram associated with the yukawa term defined by Eq. (2.9).

we observe that below the scale $\Lambda \sim m_\phi$ the scalar particle, ϕ, cannot appear anymore as an external state, since there is no energy to create it on-shell. However, the scalar can still mediate a four-fermion interaction. Hence, below the scale Λ, we have an *effective* model of four-fermions interacting according to

$$\mathcal{L}_{\text{EFT}} \supset -G \left[\overline{\psi}\,\psi\right] \left[\overline{\psi}\,\psi\right], \tag{2.10}$$

where G is a dimensionful coupling constant that characterize the strength of the interaction. In $\mathcal{L}_{\text{Fermi}}$, such a constant is called the Fermi coupling, G_F. Based on the measurement of the muon lifetime G_F is determined to have the value of 1.16×10^{-5} GeV^{-2} [14].

In our example the complete UV physics is contained in the lagrangian $\mathcal{L}_{\text{UV}}$, and at energies below the scale $m_\phi \sim \Lambda$ physics can be described by the effective field theory, $\mathcal{L}_{\text{EFT}}$. So, do we need to know both models to give an appropriate description of the low energy physics? Of course not: if the complete UV model is known one could in principle compute whatever observable at the low energy scale, as long as the coupling constant can be treated perturbatively[1]. However, due to the EFT computations are drastically simpler, we prefer the effective description even if the complete theory is known.

In order to make explicit the link between $\mathcal{L}_{\text{UV}}$ and $\mathcal{L}_{\text{EFT}}$, consider the tree level diagram showed in Fig. 2.3. In the left side of the figure we observe that between the two vertices appears the propagator of the scalar field, $\frac{i}{p^2 - m_\phi^2}$, communicating the interaction between fermions, thus acting like a mediator. In the right side of the figure the four fermions interact directly between them. As we go to lower energies, we go into the region $p^2 \ll m_\phi^2$. In this

[1]Things are different for QCD or in general for strongly interacting gauge theories, which will be the subject of study in the following section.

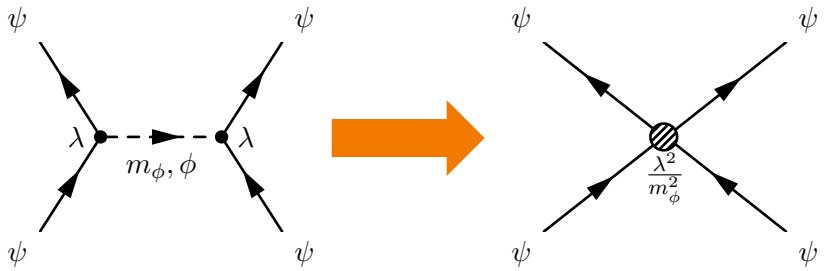

Figure 2.3: Here we show how the four fermion interaction appears in the UV model (left side of the figure) and in the effective theory (right side of the figure).

situation the scalar propagator becomes

$$\frac{i}{p^2 - m_\phi^2} \to -\frac{i}{m_\phi^2} + \mathcal{O}(\frac{p^2}{m_\phi^2}). \tag{2.11}$$

Hence, at leading order the vertex becomes independent on the momentum of the scalar field. Furthermore, it gets a value that only depends on the Yukawa coupling λ and the mass of the scalar field m_ϕ

$$G \sim \frac{\lambda^2}{m_\phi^2}. \tag{2.12}$$

It is important to note that as the energy of the process grows and becomes comparable to the mass of the mediator, $E \simeq m_\phi \sim \Lambda$, the expansion showed in Eq. (2.11) breaks down.

What if instead the UV model is not known? In this case, we are still able to describe the low energy physics up to Λ, but we must include all possible terms involving the light degrees of freedom, which are invariant under the low energy symmetries of the EFT. These object are called higher dimensional effective operators. The following subsection is devoted to a discussion of their properties.

2.3.2 EFTs: Higher dimensional effective operators

Every term in the effective lagrangian has to be Lorentz invariant, respect the symmetries of the theory, and, because the action S_{eff} is dimensionless must have dimension four, $[\mathcal{L}_{\text{eff}}] = 4$. This means that in the effective lagrangian the operators of dimension higher than four have to be properly normalized to respect this condition. The only dimensionful parameter that

can appear in the higher dimensional operators is the cutoff of the theory, Λ.

In order to be clearer in our construction, let us separate the complete set of fields in the UV in two subsets represented by φ_L and φ_H, where the labels mean *light* and *heavy* modes (with masses above and below the scale Λ, respectively):

$$\mathcal{L}_{\rm UV} \;=\; \mathcal{L}(\varphi_L, \varphi_H). \tag{2.13}$$

As we know from previous sections, after we cross the cutoff scale going to lower energies, the heavy fields have to be integrated out, and then we write an EFT based on the light fields only. Therefore, we write the effective lagrangian as

$$\mathcal{L}_{\rm eff}(\varphi_L) \;=\; \mathcal{L}_{d\leq 4} + \sum_{n>4} \frac{C_n}{\Lambda^{\dim(\mathcal{O}_n)-4}}\, \mathcal{O}_n(x), \tag{2.14}$$

where the coefficients C_n are called the *Wilson coefficients*, $\mathcal{O}_n(x)$ are local operators of dimension higher than four, Λ is the cutoff of the theory and finally $\dim(\mathcal{O}_n)$ is the dimension of the operator.

If the UV theory is known, we can use the path integral formalism to integrate out the heavy fields in the following way

$$\int \mathcal{D}\left[\varphi_H\right]\, e^{i\int \mathcal{L}(\varphi_L,\varphi_H)} \;=\; e^{i\int \mathcal{L}_{\rm eff}(\varphi_L)}, \tag{2.15}$$

and thus finding the effective lagrangian. It is worthwhile to stress that a crucial point in writing the effective lagrangian is that all terms in the expansion have to be *local* terms in space-time. Consequently, our framework is only applicable to process at energies lower than the masses of the heavy fields φ_H.

If instead the UV theory is not known, then in Eq. (2.14) we write all possible local operators which are invariant under Lorentz symmetry and any symmetry which is relevant below the cutoff Λ.

The lagrangian $\mathcal{L}_{d\leq 4}$ contains terms that are renormalizable, including the kinetic terms of the fields φ_L and any possible interaction. The second part of Eq. (2.14) contains all

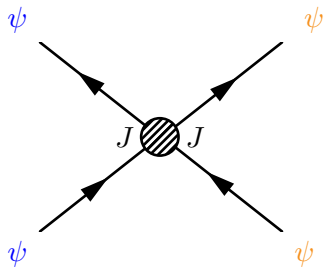

Figure 2.4: This figure schematically shows the interaction between four light fields in the EFT. It corresponds to the non-renormalizable operator $\mathcal{O}(x) \equiv J(x)\, J(x)$.

operators that have dimension higher than four, normalized by an appropriate power of the cutoff scale Λ. In the toy model considered in the previous section, we can write our effective operator as

$$\mathcal{O}(x) \equiv J(x)\, J(x), \tag{2.16}$$

where $J(x) = \left(\overline{\psi}\,\psi\right)$ is a fermionic scalar current. For effective theories that come from weakly interacting physics in the UV, the total dimension of the operator, $\dim(\mathcal{O})$, is the algebraic sum of the dimension of the current $J(x)$. Not all effective operators are necessarily built as products of currents, for example the dimension five Weinberg Operator. More in general, currents can be built up from bosonic or fermionic fields, with vector (V), axial (A), scalar (S), pseudoscalar (P) or tensor (T) Lorentz structures. Fig. 2.4 schematically shows the interaction between four light fields in the EFT. It corresponds to the non-renormalizable operator $\mathcal{O}(x) \equiv J(x)\, J(x)$.

From the phenomenological side it is necessary to use only a finite set of operators $\mathcal{O}_n(x)$. In order to see this explicitly, let us suppose that the accuracy of a given experiment is parametrized by ε. The order of the coefficients of each interaction in the effective lagrangian is

$$\sim \frac{E^n}{\Lambda^n}, \tag{2.17}$$

with $E < \Lambda$, being E the typical energy of the experiment. The contribution of a given operator of dimension n is of order E^n. Hence, considering the accuracy of the experiment

we only need to include terms up to n_ϵ

$$\left(\frac{E}{\Lambda}\right)^{n_\varepsilon} \approx \varepsilon \Rightarrow n_\varepsilon \approx \frac{\log\left(1/\varepsilon\right)}{\log\left(\Lambda/E\right)}, \tag{2.18}$$

which, of course, is a finite quantity.

If the building blocks of the EFT in Eq.(2.14) are only the SM particles[1], the resulting model is called the Standard Model Effective Field Theory (SMEFT). In the following subsection we will explore some special aspects of higher dimensional effective operators in SMEFT. Let us introduce some definitions first: D will stand for the covariant derivative, X for $\{G^A, W^I, B\}$, ψ for general fermion content, and $L(R)$ for $SU(2)_L$- doublets (singlets). We defer to Appendix A.1 a discussion of the conventions used for the SM fields.

2.3.3 SMEFT Operators

In SMEFT the problem of counting the number of effective operators of a given dimension is known to be not simple. In fact, the first counting of dimension-six operators presented by W. Buchmüller and D. Wyler in Ref.[15] gave a total of 80 operators. Later that result was corrected by B. Grzadkowski *et al.* in Ref.[16] resulting in the famous result of 59 dimension-six operators [2].

The reason behind this difficulty lies in the possibility of performing field redefinitions (equivalently apply the equations of motion (EoMs) [16; 17]) and integration by parts (IBP) [17]. The use of EoM and IBP allows the equivalence of different operators [16; 17]. For example, the operator $\left(\bar{l}_p\gamma_\mu\tau^A l_r\right)\left(\bar{l}_s\gamma_\mu\tau^A l_t\right)$[3] can be expressed as a linear combination of other operators:

$$\left(\bar{l}_p\gamma_\mu\tau^A l_r\right)\left(\bar{l}_s\gamma_\mu\tau^A l_t\right) = 2Q_{ll}^{ptsr} - Q_{ll}^{prst},$$

where we used the identity $\tau^A_{jk}\tau^A_{mn} = 2\delta_{jn}\delta_{mk} - \delta_{jk}\delta_{mn}$ and the six dimensional operator Q_{ll} is defined in Table 2.1. Considering this, in Ref.[16] was introduced the so called Warsaw

[1] It implies that $\mathcal{L}_{d\leq 4} \equiv \mathcal{L}_{SM}$.
[2] In both counting it was disregarded flavour structure and Hermitian conjugation.
[3] The $SU(2)_L$ generators are denoted with τ^A.

X^3		φ^6 and $\varphi^4 D^2$		$\psi^2\varphi^3$	
Q_G	$f^{ABC}G_\mu^{A\nu}G_\nu^{B\rho}G_\rho^{C\mu}$	Q_φ	$(\varphi^\dagger\varphi)^3$	$Q_{e\varphi}$	$(\varphi^\dagger\varphi)(\bar{l}_p e_r \varphi)$
$Q_{\tilde{G}}$	$f^{ABC}\widetilde{G}_\mu^{A\nu}G_\nu^{B\rho}G_\rho^{C\mu}$	$Q_{\varphi\Box}$	$(\varphi^\dagger\varphi)\Box(\varphi^\dagger\varphi)$	$Q_{u\varphi}$	$(\varphi^\dagger\varphi)(\bar{q}_p u_r \widetilde{\varphi})$
Q_W	$\varepsilon^{IJK}W_\mu^{I\nu}W_\nu^{J\rho}W_\rho^{K\mu}$	$Q_{\varphi D}$	$\left(\varphi^\dagger D^\mu\varphi\right)^*\left(\varphi^\dagger D_\mu\varphi\right)$	$Q_{d\varphi}$	$(\varphi^\dagger\varphi)(\bar{q}_p d_r \varphi)$
$Q_{\widetilde{W}}$	$\varepsilon^{IJK}\widetilde{W}_\mu^{I\nu}W_\nu^{J\rho}W_\rho^{K\mu}$				

$X^2\varphi^2$		$\psi^2 X\varphi$		$\psi^2\varphi^2 D$	
$Q_{\varphi G}$	$\varphi^\dagger\varphi\, G_{\mu\nu}^A G^{A\mu\nu}$	Q_{eW}	$(\bar{l}_p\sigma^{\mu\nu}e_r)\tau^I\varphi W_{\mu\nu}^I$	$Q_{\varphi l}^{(1)}$	$(\varphi^\dagger i\overleftrightarrow{D}_\mu\varphi)(\bar{l}_p\gamma^\mu l_r)$
$Q_{\varphi\widetilde{G}}$	$\varphi^\dagger\varphi\,\widetilde{G}_{\mu\nu}^A G^{A\mu\nu}$	Q_{eB}	$(\bar{l}_p\sigma^{\mu\nu}e_r)\varphi B_{\mu\nu}$	$Q_{\varphi l}^{(3)}$	$(\varphi^\dagger i\overleftrightarrow{D}_\mu^I\varphi)(\bar{l}_p\tau^I\gamma^\mu l_r)$
$Q_{\varphi W}$	$\varphi^\dagger\varphi\, W_{\mu\nu}^I W^{I\mu\nu}$	Q_{uG}	$(\bar{q}_p\sigma^{\mu\nu}T^A u_r)\widetilde{\varphi}\, G_{\mu\nu}^A$	$Q_{\varphi e}$	$(\varphi^\dagger i\overleftrightarrow{D}_\mu\varphi)(\bar{e}_p\gamma^\mu e_r)$
$Q_{\varphi\widetilde{W}}$	$\varphi^\dagger\varphi\,\widetilde{W}_{\mu\nu}^I W^{I\mu\nu}$	Q_{uW}	$(\bar{q}_p\sigma^{\mu\nu}u_r)\tau^I\widetilde{\varphi}\, W_{\mu\nu}^I$	$Q_{\varphi q}^{(1)}$	$(\varphi^\dagger i\overleftrightarrow{D}_\mu\varphi)(\bar{q}_p\gamma^\mu q_r)$
$Q_{\varphi B}$	$\varphi^\dagger\varphi\, B_{\mu\nu}B^{\mu\nu}$	Q_{uB}	$(\bar{q}_p\sigma^{\mu\nu}u_r)\widetilde{\varphi}\, B_{\mu\nu}$	$Q_{\varphi q}^{(3)}$	$(\varphi^\dagger i\overleftrightarrow{D}_\mu^I\varphi)(\bar{q}_p\tau^I\gamma^\mu q_r)$
$Q_{\varphi\widetilde{B}}$	$\varphi^\dagger\varphi\,\widetilde{B}_{\mu\nu}B^{\mu\nu}$	Q_{dG}	$(\bar{q}_p\sigma^{\mu\nu}T^A d_r)\varphi\, G_{\mu\nu}^A$	$Q_{\varphi u}$	$(\varphi^\dagger i\overleftrightarrow{D}_\mu\varphi)(\bar{u}_p\gamma^\mu u_r)$
$Q_{\varphi WB}$	$\varphi^\dagger\tau^I\varphi\, W_{\mu\nu}^I B^{\mu\nu}$	Q_{dW}	$(\bar{q}_p\sigma^{\mu\nu}d_r)\tau^I\varphi\, W_{\mu\nu}^I$	$Q_{\varphi d}$	$(\varphi^\dagger i\overleftrightarrow{D}_\mu\varphi)(\bar{d}_p\gamma^\mu d_r)$
$Q_{\varphi\widetilde{W}B}$	$\varphi^\dagger\tau^I\varphi\,\widetilde{W}_{\mu\nu}^I B^{\mu\nu}$	Q_{dB}	$(\bar{q}_p\sigma^{\mu\nu}d_r)\varphi\, B_{\mu\nu}$	$Q_{\varphi ud}$	$i(\widetilde{\varphi}^\dagger D_\mu\varphi)(\bar{u}_p\gamma^\mu d_r)$

$(\bar{L}L)(\bar{L}L)$		$(\bar{R}R)(\bar{R}R)$		$(\bar{L}L)(\bar{R}R)$	
Q_{ll}	$(\bar{l}_p\gamma_\mu l_r)(\bar{l}_s\gamma^\mu l_t)$	Q_{ee}	$(\bar{e}_p\gamma_\mu e_r)(\bar{e}_s\gamma^\mu e_t)$	Q_{le}	$(\bar{l}_p\gamma_\mu l_r)(\bar{e}_s\gamma^\mu e_t)$
$Q_{qq}^{(1)}$	$(\bar{q}_p\gamma_\mu q_r)(\bar{q}_s\gamma^\mu q_t)$	Q_{uu}	$(\bar{u}_p\gamma_\mu u_r)(\bar{u}_s\gamma^\mu u_t)$	Q_{lu}	$(\bar{l}_p\gamma_\mu l_r)(\bar{u}_s\gamma^\mu u_t)$
$Q_{qq}^{(3)}$	$(\bar{q}_p\gamma_\mu\tau^I q_r)(\bar{q}_s\gamma^\mu\tau^I q_t)$	Q_{dd}	$(\bar{d}_p\gamma_\mu d_r)(\bar{d}_s\gamma^\mu d_t)$	Q_{ld}	$(\bar{l}_p\gamma_\mu l_r)(\bar{d}_s\gamma^\mu d_t)$
$Q_{lq}^{(1)}$	$(\bar{l}_p\gamma_\mu l_r)(\bar{q}_s\gamma^\mu q_t)$	Q_{eu}	$(\bar{e}_p\gamma_\mu e_r)(\bar{u}_s\gamma^\mu u_t)$	Q_{qe}	$(\bar{q}_p\gamma_\mu q_r)(\bar{e}_s\gamma^\mu e_t)$
$Q_{lq}^{(3)}$	$(\bar{l}_p\gamma_\mu\tau^I l_r)(\bar{q}_s\gamma^\mu\tau^I q_t)$	Q_{ed}	$(\bar{e}_p\gamma_\mu e_r)(\bar{d}_s\gamma^\mu d_t)$	$Q_{qu}^{(1)}$	$(\bar{q}_p\gamma_\mu q_r)(\bar{u}_s\gamma^\mu u_t)$
		$Q_{ud}^{(1)}$	$(\bar{u}_p\gamma_\mu u_r)(\bar{d}_s\gamma^\mu d_t)$	$Q_{qu}^{(8)}$	$(\bar{q}_p\gamma_\mu T^A q_r)(\bar{u}_s\gamma^\mu T^A u_t)$
		$Q_{ud}^{(8)}$	$(\bar{u}_p\gamma_\mu T^A u_r)(\bar{d}_s\gamma^\mu T^A d_t)$	$Q_{qd}^{(1)}$	$(\bar{q}_p\gamma_\mu q_r)(\bar{d}_s\gamma^\mu d_t)$
				$Q_{qd}^{(8)}$	$(\bar{q}_p\gamma_\mu T^A q_r)(\bar{d}_s\gamma^\mu T^A d_t)$

$(\bar{L}R)(\bar{R}L)$ and $(\bar{L}R)(\bar{L}R)$		B-violating	
Q_{ledq}	$(\bar{l}_p^j e_r)(\bar{d}_s q_t^j)$	Q_{duq}	$\varepsilon^{\alpha\beta\gamma}\varepsilon_{jk}\left[(d_p^\alpha)^T C u_r^\beta\right]\left[(q_s^{\gamma j})^T C l_t^k\right]$
$Q_{quqd}^{(1)}$	$(\bar{q}_p^j u_r)\varepsilon_{jk}(\bar{q}_s^k d_t)$	Q_{qqu}	$\varepsilon^{\alpha\beta\gamma}\varepsilon_{jk}\left[(q_p^{\alpha j})^T C q_r^{\beta k}\right]\left[(u_s^\gamma)^T C e_t\right]$
$Q_{quqd}^{(8)}$	$(\bar{q}_p^j T^A u_r)\varepsilon_{jk}(\bar{q}_s^k T^A d_t)$	Q_{qqq}	$\varepsilon^{\alpha\beta\gamma}\varepsilon_{jn}\varepsilon_{km}\left[(q_p^{\alpha j})^T C q_r^{\beta k}\right]\left[(q_s^{\gamma m})^T C l_t^n\right]$
$Q_{lequ}^{(1)}$	$(\bar{l}_p^j e_r)\varepsilon_{jk}(\bar{q}_s^k u_t)$	Q_{duu}	$\varepsilon^{\alpha\beta\gamma}\left[(d_p^\alpha)^T C u_r^\beta\right]\left[(u_s^\gamma)^T C e_t\right]$
$Q_{lequ}^{(3)}$	$(\bar{l}_p^j\sigma_{\mu\nu}e_r)\varepsilon_{jk}(\bar{q}_s^k\sigma^{\mu\nu}u_t)$		

Table 2.1: List of independent dimension six operators of Warsaw basis as introduced in Ref.[16].

basis for dimension six operators. The complete set of independent operators that forms this basis is given in Table 2.1.

One interesting result about higher dimensional SMEFT was derived in Ref.[18]. For a given operator $\mathcal{O}_n(x)$, we have that

$$\frac{1}{2}\left(\Delta B - \Delta L\right) \equiv n \pmod 2 \tag{2.19}$$

where n is the dimension of the operator. This implies that the dimension five Weinberg

operator always violates lepton number by two units, for instance.

SMEFT: Operators of dimension 5

There is just one single operator of dimension five that could be formed using the standard model particles. This operator is also known as the Weinberg Operator [19]. It can be used to give masses to neutrinos through out the see-saw mechanism. Explicitly this operator is written as

$$\mathcal{L}_{5-\text{dim}} = c_{ij}^{5} \frac{\left(L_i \widetilde{H}\right)\left(\widetilde{H} L_j\right)}{\Lambda}. \tag{2.20}$$

This operator is associated to the diagram shows in Fig.2.5.

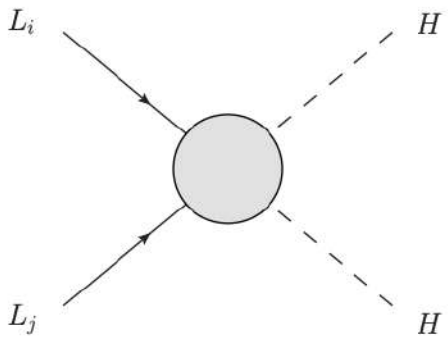

Figure 2.5: Dimension five Weinberg operator responsible for neutrino mass generation [20].

It is a good exercise try to think why there are no pure bosonic operator of dimension five. Since the Higgs is a $SU(2)_L$- doublet, any bosonic operator must contain an even number of H. The same reasoning works for the covariant derivative, because of its Lorentz structure. Hence, the smallest dimension we could form so far is four. Since X has dimension two, we conclude that there are no pure bosonic dimension five operators.

SMEFT: Operators of dimension 6

For one generation ($N_f = 1$), counting Hermitian and non-Hermitian operators just once, and considering $\Delta B = \Delta L = 0$ there are a total of 59 independent operators [16] as shown in Tab.2.1. Sometimes in the literature the condition on Hermitian operators is modified to account operators under Hermitian conjugation as independent operators. In such a case the above counting becomes 76, instead. In addition, if we allow for operators such that $\Delta B = \Delta L = \pm 1$, there are 8 extra operators given a total of $76 + 8 = 84$. For three generations ($N_f = 3$), the above results are modified to 2499 ($\Delta B = \Delta L = 0$) and 546 ($\Delta B = \Delta L = \pm 1$), respectively.

In Ref.[17] is presented the following formula for the total number of independent dimension six operators:

$$\#\text{Dim}\,6 = \left(15 + \frac{135}{4}N_f^2 + \frac{1}{2}N_f^3 + \frac{107}{4}N_f^4\right) + \left(\frac{2}{3}N_f^2 + N_f^3 + \frac{19}{3}N_f^4\right) \tag{2.21}$$

where N_f is the number of generations considered. In Eq.(2.21), the total number of dimension six operators is split in parenthesis as $(\Delta B = 0) + (\Delta B = 1)$.

SMEFT: Operators of dimension $7, 8$ and higher

Operators of higher dimension than six are commonly disregarded because of their smaller contributions to observables. However, there are some interesting comments about these operators [17]:

1. Dimension seven operators violate either baryon or lepton number;
2. Dimension seven operators violate $B - L$;
3. Dimension seven operators could have zero, one or two derivatives;
4. The baryon violating dimension eight operators have $\Delta B = 1$, and all operators preserve $B - L$;
5. Dimension eight operators could have zero, one, two, three or four derivatives.

Currently there is an unsolved mismatch in the counting of dimension seven and eight operators between previous studies [21; 22] and the recent in Ref.[17]. The formulas for the total number of independent dimension 7 and 8 operators as deduced in Ref.[17] are:

$$\#\text{Dim}\,7 = \left(2N_f + \frac{26}{3}N_f^2 + N_f^3 + \frac{31}{3}N_f^4\right) + \left(N_f^3 + 7N_f^4\right), \tag{2.22}$$

$$\#\text{Dim}\,8 = \left(89 + \frac{789}{2}N_f^2 + \frac{823}{2}N_f^4\right) + \left(\frac{2}{3}N_f^2 + N_f^3 + \frac{289}{3}N_f^4\right). \tag{2.23}$$

Eqs.(2.22) and (2.23) are split in parenthesis as $(\Delta B = 0) + (\Delta B = 1)$.

It is worthwhile to comment that Ref.[17], using invariant theory and Hilbert series [17; 23; 24], has presented formulas for the total number of effective operators up to dimension 15. Those formulas only depend on the number of flavors of the theory. Using those results it is possible to generate a plot to see the growth of the number of independent operators in the SMEFT by depending on the dimension of the operator, see Fig.2.6. It is also notable that the exponential behavior of Fig.2.6 has been already predicted 30 years ago in Ref.[25].

2.4 EFTs: Non-Perturbative models

In the previous section we considered perturbative theories. However there are other possible interesting scenarios that do not admit a perturbative analysis, at least in some range of energies. The best known example of this scenario is low energy QCD. The best we can do with such kind of theories is working using lattice theory. However, lattice is unable to go beyond some limited range of low energies below the scale of confinement, lose the dynamical evolution of the theory and has problems to deal with massive fermions. Therefore, in absence of mathematical techniques to deal efficiently from first principles with the low energy physics of strongly interacting theories, some effective models were developed. The following subsection is devoted to a discussion of one such model, the linear Sigma model [26].

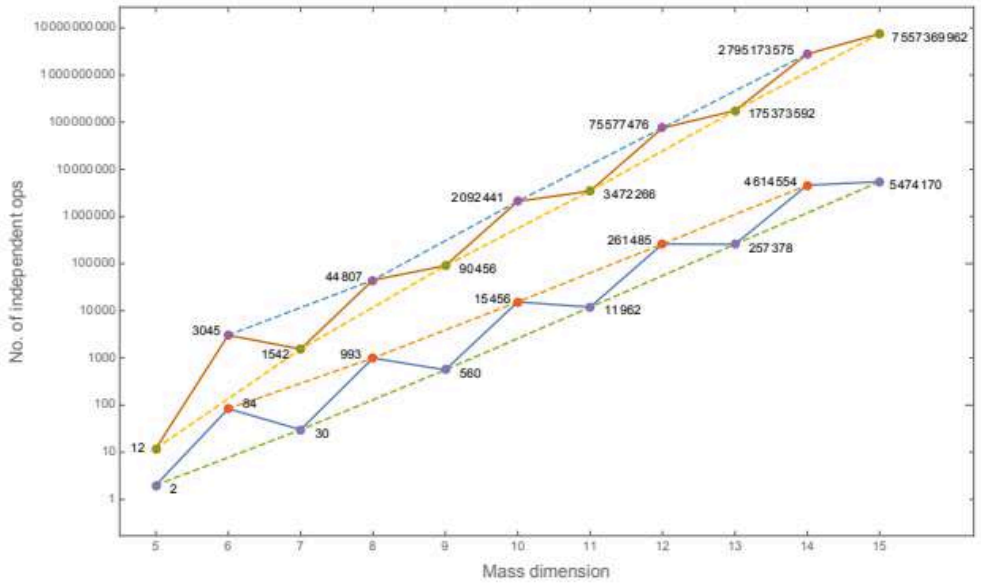

Figure 2.6: In this figure Ref.[17] showed the growth of the number of independent operators in SMEFT. Blue solid line is for $N_f = 1$, and Orange solid line is for $N_f = 3$. Dashed lines link even and odd dimension operators.

2.4.1 Low-energy description: The Linear Sigma Model

In 1960, M. Gell-Mann and M. Levy introduced this effective model in Ref.[26]. The linear sigma model has its origin as an effective model trying to describe the pion decay. The typical Lagrangian of the linear sigma model is written as

$$\mathcal{L} = \frac{1}{2}(\partial_\mu \sigma)^2 + \frac{1}{2}(\partial_\mu \vec{\boldsymbol{\pi}})^2 + \frac{\mu^2}{2}\left(\sigma^2 + \vec{\boldsymbol{\pi}}^2\right) - \frac{\lambda}{4!}\left(\sigma^2 + \vec{\boldsymbol{\pi}}^2\right)^2, \tag{2.24}$$

where the pseudoscalar field $\vec{\boldsymbol{\pi}} = (\pi_1, \pi_2, \pi_3)$ is an isotriplet of pion fields, and σ an isosinglet. We could rewrite the above lagrangian using a multiplet of four real scalar fields $\Phi(x)^T \equiv (\vec{\boldsymbol{\pi}}, \sigma)$, with lagrangian

$$\mathcal{L} = \frac{1}{2}\partial_\mu \Phi^T \, \partial^\mu \Phi + \frac{\mu^2}{2}\Phi^T \Phi - \frac{\lambda}{4!}\left(\Phi^T \Phi\right)^2. \tag{2.25}$$

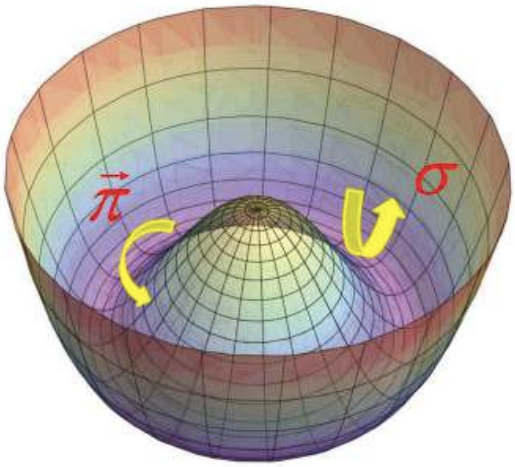

Figure 2.7: Sigma model potential and its radial (angular) mode, σ ($\vec{\boldsymbol{\pi}}$) respectively [27].

This form of the lagrangian allow to see explicitly the invariance under $SO(4)$. For $\mu^2 > 0$, the vacuum expectation value is $v = \sqrt{6\mu^2/\lambda} > 0$. This value characterizes the degenerated ground states of the model. These states can be transformed into each other by a $SO(4)$ transformation. This means that there is a continuous set of degenerate minima satisfying $\Phi^T\Phi = v^2$. A schematic picture of the potential and its degenerate ground states is given in Fig.2.7. We adopt the following vev direction

$$\langle\Phi\rangle^T \quad = \quad (0, \quad 0, \quad 0, \quad v), \tag{2.26}$$

or equivalently, $\langle\vec{\boldsymbol{\pi}}\rangle = \vec{\mathbf{0}}$ and $\langle\sigma\rangle = v$. Hence, our vacuum choice still respects $SO(3)$ rotations. We could also say that the pattern symmetry breaking is

$$SO(4) \to SO(3). \tag{2.27}$$

Due to the Goldstone theorem we know that this pattern gives rise to 3 Nambu-Goldstone bosons (NGB): π^+, π^0 and π^-. More generally, by the same theorem a sigma model with the symmetry breaking pattern $SO(N) \to SO(N-1)$ shall have $N-1$ NGB [27].

We could rewrite the above lagrangians in a even more convenient form. This can be

made using 2×2 matrices, and then defining the Σ field

$$\Sigma \equiv \sigma \, \mathbb{1}_2 + i \, \vec{\tau} \cdot \vec{\pi}, \tag{2.28}$$

where $\vec{\tau}$ are the Pauli matrices. In this way, Eqs.(2.24) and (2.25) become

$$\mathcal{L} \;=\; \frac{1}{4}\langle \partial_\mu \Sigma^\dagger \partial^\mu \Sigma \rangle + \frac{\mu^2}{4}\langle \Sigma^\dagger \Sigma \rangle - \frac{\lambda}{96}\langle \Sigma^\dagger \Sigma \rangle^2, \tag{2.29}$$

where $\langle \dots \rangle$ means trace of a matrix. The above lagrangian is explicitly invariant under $SU(2)_L \otimes SU(2)_R$. The pattern of symmetry breaking is now realized as

$$SU(2)_L \otimes SU(2)_R \to SU(2)_{L+R}. \tag{2.30}$$

However, in this form the linear sigma model is unable to explain light pion masses. In order to incorporate massive pions into the model, we add the extra linear term to $\mathcal{L}$

$$\mathcal{L}_b = \epsilon \, \sigma, \;\; \epsilon \ll 1. \tag{2.31}$$

Such a new term explicitly breaks the $SU(2)_L \otimes SU(2)_R$ symmetry. Hence, the pions become Pseudo Nambu-Goldstone bosons (pNGB). Because pion masses are generated by Eq.(2.31), they should be degenerate and smaller than the scale of chiral symmetry breaking. We also know that as $\epsilon \to 0$, pions must become massless, thus we expect that $m_\pi^2 \sim \epsilon$. To first order in ϵ, a computation of pion masses give

$$m_\pi^2 = \frac{\epsilon}{v}. \tag{2.32}$$

All this formalism can be extended to a more general framework. We develop this in Appendix E.1.1.

It is also possible to write a term that breaks the axial $U(1)_A$ and thus mimics instantons

effects:

$$\mathcal{L} \supset -\mu_\Sigma \left(\det\Sigma + \det\Sigma^\dagger \right). \tag{2.33}$$

Therefore, this term arises trying to imitate the effect of the complex vacuum structure of strongly interacting gauge theories. It will be important in Chapter 5, because there Eq.(2.33) generates the cubic term necessary for first order phase transitions[1]. Another important reason is the relation between this term and the mass of the η', because the ratio between the η' and the scalar mass seems to be related to the spectrum of the gravitational waves produced via the phase transitions mentioned above [28].

In this way this Section provided the basis of EFT that will be used in the following Chapters. In particular in the next one, we shall apply the ideas of EFT developed in Section 2.3 to the possible detection of a special type of neutrinos that are best known as relic neutrinos.

[1] In our $N_f = 3$ case.

Chapter 3

Relic Neutrinos

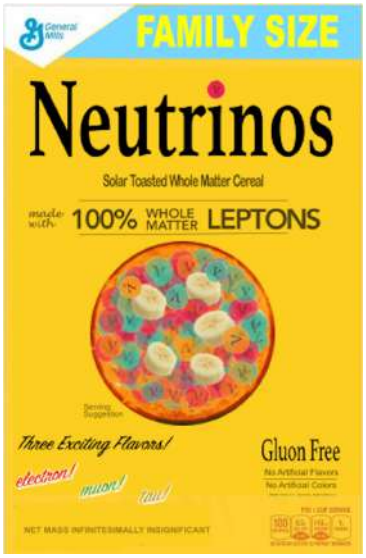

Credits to Ref.[29].

3.1 Introduction

Neutrino physics deserves an important place in any attempt to describe BSM physics. As we already mentioned in Chapter 1, the absence of neutrino masses in the standard model is a clear signal of physics beyond the standard model.

In the present chapter we expand the study of neutrino physics with a special focus on the so called *relic* neutrinos. To this end, we start by discussing the role of neutrinos in the SM. We then move to the definition of relic neutrinos, describing their properties and experimental setups dedicated to their detection. Finally, we parametrize the effect of possible new physics via effective operators and study the effect of such new physics on the relic neutrino detection.

3.2 Neutrinos in the Standard Model

Neutrinos are really interesting particles, they permeate everything around us and are the second more abundant type of particles in the universe. Approximately, a thousand neutrinos from cosmic rays interact with Earth's atmosphere and 10^{14} neutrinos coming from the Sun pass through us each second [30]. There are other natural and artificial sources of neutrinos

on Earth, for example the decay of some radioactive elements [31; 32].

For a long time neutrinos were thought as being massless particles; however, oscillation experiments [33] showed that in fact they are massive. This also implies that neutrinos could decay in other particles. Nevertheless, properties of neutrinos are difficult to test experimentally because they interact very weakly with ordinary matter.

The original idea that the neutrinos were massless, $m_\nu = 0$, was supported by the following argument: In QFT a mass term for Dirac fermions needs the left and right component of the fermion to be linked via[1]

$$m\,\overline{\psi}\,\psi = m\left(\overline{\psi}_L\,\psi_R + \overline{\psi}_R\,\psi_L\right). \tag{3.1}$$

Since, neutrinos produced in charged-current interactions are pure left-handed, thus there is no experimental evidence for the existence of ν_R. Hence, following these arguments we would have a consistent theory of neutrinos by only considering left-handed neutrinos, ν_L, and thus no mass term is present in the lagrangian. The simplest explanation for this fact is that neutrinos would have to be massless particles.

During the decade of 1960, Weinberg, Salam and Glashow proposed the current model that describes and unifies three of the fourth fundamental forces in nature, the Standard Model. The SM is a gauge theory based on the gauge symmetry group $SU(3)_C \times SU(2)_L \times U(1)_Y$. We schematically show an overview of the particle content of the SM in Fig. 3.1. Inside the SM the correct gauge sector that describes the behavior of leptons is the electroweak gauge group $SU(2)_L \times U(1)_Y$. Following the experimental evidence mentioned above, leptons have to be grouped into left-handed doublets

$$l_e = \begin{pmatrix} \nu_e \\ e \end{pmatrix}_L, \; l_\mu = \begin{pmatrix} \nu_\mu \\ \mu \end{pmatrix}_L, \; l_\tau = \begin{pmatrix} \nu_\tau \\ \tau \end{pmatrix}_L, \tag{3.2}$$

[1] We shall talk about Majorana fermions in the following sub-sections.

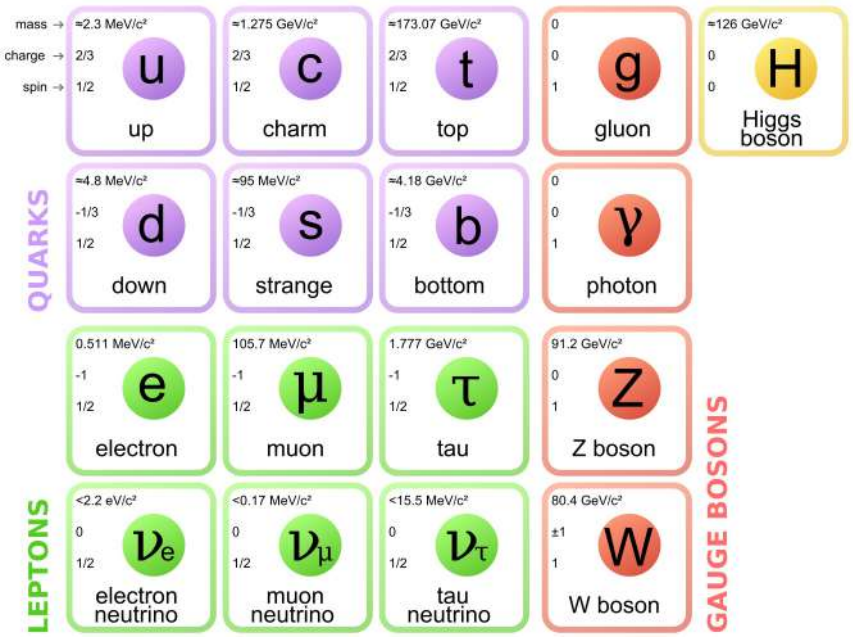

Figure 3.1: Particle content inside the Standard Model. Leptons are represented in green [34].

and there are no right-handed neutrinos, while charged leptons have right-handed components

$$e_R,\ \mu_R,\ \tau_R \tag{3.3}$$

which are singlets under $SU(2)_L$. Some properties of leptons, like their mass and lifetime, are given in Table 3.1. In order to properly understand the results of our research it will be useful to recall the properties of Dirac and Majorana fermions. After that we shall analyze the difference of considering Dirac or Majorana neutrinos by counting their degrees of freedom. Discriminate neutrinos by their nature has a deep impact in their phenomenology. We will return to this point later.

Lepton	Mass	Lifetime
ν_e	< 2 eV	
e^-	0.51 MeV	$> 4.6 \times 10^{26}$ y
ν_μ	< 0.19 MeV	
μ^-	105.65 MeV	2.19×10^{-6} s
ν_τ	< 18.2 MeV	
τ^-	1776.90 MeV	290.6×10^{-15} s

Table 3.1: Properties of leptons in the standard model, mass and lifetime [30].

3.2.1 Dirac fermions

Dirac fermions are solutions of the well known Dirac equation $(i\gamma^\mu \partial_\mu - m)\Psi = 0$. As usual the γ^μ's satisfy the anti-commutation relation

$$\{\gamma^\mu, \gamma^\nu\} \quad = \quad 2\eta^{\mu\nu}, \tag{3.4}$$

where $\eta^{\mu\nu}$ is the Minkowski metric. In the so called Weyl basis of the γ-matrices, they are written as

$$\gamma^0 \quad = \quad \begin{pmatrix} 0 & \mathbb{1} \\ \mathbb{1} & 0 \end{pmatrix}, \; \gamma^k = \begin{pmatrix} 0 & \sigma^k \\ -\sigma^k & 0 \end{pmatrix}, \tag{3.5}$$

where σ^k are the Pauli matrices. The Weyl representation is a $\left(\frac{1}{2}, 0\right) \oplus \left(0, \frac{1}{2}\right)$ representation of the Lorentz group. A general solution of the Dirac equation has the form

$$\Psi_{\mathrm{D}} = \begin{pmatrix} \Psi_L \\ \Psi_R \end{pmatrix}, \tag{3.6}$$

where both the LH and RH spinors Ψ_L and Ψ_R, respectively, are complex objects. Each one of these chiral components is called a Weyl fermion. Weyl fermions are more fundamental in a sense, they are irreducible representations of the Lorentz group. These facts will be important when counting the degrees of freedom.

In the next sub-section we are going to use another reducible representation of the Lorentz

group, the so called *Majorana* representation.

3.2.2 Majorana fermions

We start this subsection with the introduction of Majorana fermions. For a direct definition of these fermions we can go immediately to Eq.(3.16). Instead, a constructive introduction of these fields is as follows: As mentioned at the end of the previous sub-section, we choose γ^μ's that satisfy Eq. (3.4) and that have purely imaginary entries

$$\begin{aligned} \gamma^0 &= \begin{pmatrix} 0 & \sigma^2 \\ \sigma^2 & 0 \end{pmatrix}, \ \gamma^1 = \begin{pmatrix} i\sigma^3 & 0 \\ 0 & i\sigma^3 \end{pmatrix}, \\ \gamma^2 &= \begin{pmatrix} 0 & -\sigma^2 \\ \sigma^2 & 0 \end{pmatrix}, \ \gamma^3 = \begin{pmatrix} -i\sigma^1 & 0 \\ 0 & -i\sigma^1 \end{pmatrix}. \end{aligned} \tag{3.7}$$

The previous γ-matrices define the Majorana representation. Solutions to the Dirac equation with the γ^μ's as defined in Eq. (3.7) are real solutions. Hence, if Ψ is a solution in the Majorana representation, we have

$$\Psi = \Psi^*. \tag{3.8}$$

This solution represents a Majorana fermion. However, we have found such a solution in a particular representation of γ-matrices. More in general, we must relate the γ-matrices in the Majorana representation to an arbitrary representation by a similarity transformation. Hence, given the unitary matrix U we have that

$$\gamma^\mu_{\text{Arb.}} = U\, \gamma^\mu_{\text{Maj.}}\, U^\dagger \tag{3.9}$$

represents the relation between the γ-matrices in two different representations. From the Dirac equation we can easily check that

$$\left(i\gamma^\mu_{\text{Maj.}}\, \partial_\mu - m\right)\, \Psi_{\text{Maj.}} = 0 \ \Rightarrow \ \left(i\, \gamma^\mu_{\text{Arb.}}\, \partial_\mu - m\right)\, \Psi = 0, \tag{3.10}$$

which means that

$$\Psi = U\,\Psi_{\rm Maj.} \tag{3.11}$$

is also a solution. Eqs.(3.9) and (3.11) imply that $U^\dagger\,\Psi = (U^\dagger\,\Psi)^*$. From the latter relation we have

$$\Psi = U\,U^{\rm T}\,\Psi^*. \tag{3.12}$$

Now, it is not difficult to check that the combination $U\,U^{\rm T}$ satisfy $\left(U\,U^{\rm T}\right)^\dagger\,\left(U\,U^{\rm T}\right) = \mathbb{1}$, thus it is also a unitary matrix. It is customary to use this combination of unitary matrices to define the unitary matrix C

$$U\,U^{\rm T} = -i\,\gamma_2\,C. \tag{3.13}$$

Such a matrix is called the charge-conjugation matrix. From Eq.(3.12) we have $\Psi^* = U\,U^{\rm T}\,\Psi$, which implies that $\Psi^* = -i\,\gamma_2\,C\,\Psi$. In this way, we define the operation of charge conjugation

$$C: \;\; \Psi \to -i\,\gamma_2\,\Psi^* \tag{3.14}$$

and the charge-conjugate fermion field:

$$\Psi^C = -i\,\gamma_2\,\Psi^*. \tag{3.15}$$

From this definition and Eq.(3.12), we see that a Majorana fermion is the one which is equal to its own charge-conjugate

$$\Psi^C = \Psi. \tag{3.16}$$

This is also called "reality condition". Physically this means that Majorana fermions are their own antiparticle.

3.2.3 Counting the degrees of freedom

In four dimensions, fermions have four complex degrees of freedom, which turn into 8 real degrees of freedom. However, the Dirac equation imposes a constrain which eliminates a half of them. Hence, for a Dirac fermion we have a total of 4 real DOF. Conversely, Majorana fermions have an additional condition, the reality one, in such a way that the DOF are reduced by a half again, given a total of 2 real DOF.

The generalization of this idea to D-dimensions (being D even) is straightforward. Dirac fermions have $2^{D/2}$ DOF and Majorana ones have $2^{D/2-1}$. In any case, we conclude that

$$\frac{\#\,\text{DOF Majorana Fermions}}{\#\,\text{DOF Dirac Fermions}} = \frac{1}{2}. \tag{3.17}$$

This difference between these two type of fermions is going to make an important impact in the capture rate of neutrinos on tritium, as we are going to see later in this Chapter.

3.2.4 Dirac or Majorana neutrino masses

Since the discovery of neutrino oscillation [33], we know that neutrinos are massive particles. Therefore, we now face the problem of how to introduce mass terms in the SM lagrangian. There are two main proposals about how to fit them. If neutrinos are Dirac fermions, we introduce a mass term through out

$$\mathcal{L} \supset m_\nu\, \overline{\nu}\, \nu = m_\nu\, (\overline{\nu}_L\, \nu_R + \overline{\nu}_R\, \nu_L) \tag{3.18}$$

where the mass m_ν could be generated by the Higgs VEV. Nevertheless, to have $m_\nu \sim \mathcal{O}(0.1\text{eV})$ the Yukawa coupling must be around 10^{-12}, so very small compared to the other SM Yukawas. We also note that because in this scenario the right-handed neutrino is not charged neither under the SM electroweak gauge group (no weak isospin, no hypercharge), nor the strong interaction, it is called *sterile*.

In contrast, for Majorana neutrinos because of the reality condition we have $\nu_R = \nu_L^C$,

$$\mathcal{L} \supset \frac{m_\nu}{2} \left(\overline{\nu}_L \, \nu_L^C + \overline{\nu}_L^C \, \nu_L \right) = \frac{m_\nu}{2} \left(\overline{\nu}_L \, C \, \overline{\nu}_L^{\mathrm{T}} + \nu_L^{\mathrm{T}} \, C \, \nu_L \right). \tag{3.19}$$

Note that while Eq.(3.18) does not violate lepton number, the mass term determined by Eq.3.19 violates lepton number by two units. We discussed about the dimension five Weinberg operator that could generate the mass term given by Eq.(3.19) in Chapter 2.

In sub-section 3.2.3 we saw that the number of DOF is different if neutrinos are Dirac or Majorana. The situation is more subtle in the case of non-relativistic neutrinos, because in this case a distinction between *chirality* and *helicity* appears. Hence, following with the chapter, in the next section we introduce relic neutrinos. We will see that the standard model of Cosmology suggests that for them $p_\nu \ll m_\nu$, thus being non-relativistic.

3.3 What are relic neutrinos?

In 1965, Dicke, Peebles, Roll and Wilkinson published a paper entitled "Cosmic Black-Body Radiation" [35]. In that paper it was proposed a possible thermal history of the universe. In that picture, light neutrinos (produced in the early universe) thermally decoupled from ordinary matter around *one* second after the Big Bang. These are the neutrinos that we call relic neutrinos. The standard model of Cosmology predicts that, if neutrinos are stable particles (at least on cosmological time), their temperature today must be around $\sim 1.7 \times 10^{-4}$ eV. A similar calculation shows that their momentum must be of the order $\sim$ meV, and since neutrino masses are at most of order of some $\sim$ eV [33], it is straightforward to conclude that these neutrinos are non-relativistic today.

An explicit computation of various of these quantities will be given in next section.

3.4 Thermal history of the CνB

In the early stages of the universe after the Big Bang, a hot and dense plasma made of electrons, positrons and photons was in thermal equilibrium with neutrinos via the weak

interaction and through the scatterings $\nu\, e \longleftrightarrow \nu\, e$, see Fig. 3.2, and $e^+\, e^- \longleftrightarrow \nu\, \overline{\nu}$, see Fig. 3.3. Each one of these two scatterings can be described by the Fermi theory. This implies

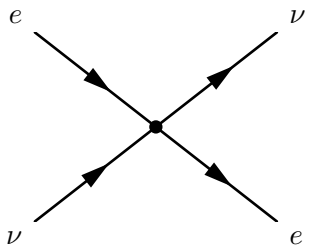

Figure 3.2: Thermal equilibrium through $\nu\, e \longleftrightarrow \nu\, e$.

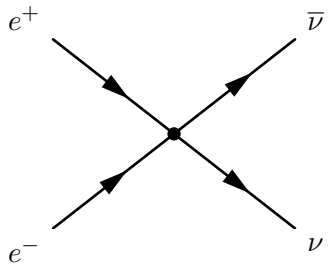

Figure 3.3: Thermal equilibrium through $e^+\, e^- \longleftrightarrow \nu\, \overline{\nu}$.

that the scattering rate of the processes goes like $\Gamma \sim G_{\rm F}^2\, T^5$. Since these scatterings are mediated by the weak interaction, neutrinos appear in these processes as flavor eigenstates: ν_e, ν_μ, ν_τ, $\overline{\nu}_e$, $\overline{\nu}_\mu$, $\overline{\nu}_\tau$. In addition, thermal neutrinos follow a Fermi-Dirac distribution

$$f_{\rm FD}(\mathbf{p}, T) = \frac{1}{1 + e^{E/T}}, \tag{3.20}$$

where $E = \sqrt{\mathbf{p^2} + m_\nu^2}$ and T is the temperature of the plasma. After integrating over all the phase space, we obtain

$$\begin{aligned} n_\nu(T) &= \int \frac{d^3p}{(2\pi)^3}\, f_{\rm FD}(\mathbf{p}, T) \\ &= \frac{3\zeta(3)}{4\pi^2} T^3, \end{aligned} \tag{3.21}$$

which is the number density of neutrinos per degree of freedom.

As mentioned, while the universe was expanding, the thermal equilibrium of neutrinos had been maintained through the processes showed in Figs. 3.2 and 3.3. Quantitatively this

means that the rate of the processes Γ had to be greater than the Hubble expansion rate, H. However, at certain temperature $T_{\rm fo}$, Γ dropped below the Hubble expansion rate, and neutrinos fell out of thermal equilibrium. This moment in the thermal history of the universe is called the neutrino *freeze out*.

We can easily estimate the temperature of neutrino freeze out $T_{\rm fo}$. As we said, the thermal equilibrium was maintained until

$$\begin{aligned} \Gamma &\sim H \\ G_{\rm F}^2\, T_{\rm fo}^5 &\sim \frac{T_{\rm fo}^2}{M_{\rm Pl}} \\ \Rightarrow T_{\rm fo} &\sim \text{MeV}, \end{aligned} \tag{3.22}$$

where $M_{\rm Pl}$ is the Planck mass. After neutrinos fell out of thermal equilibrium, they just started to free stream across the universe. These are the relic neutrinos.

Now, we would like to know about the present abundance of these kind of neutrinos. To this end, we shall use the so called sudden freeze out approximation [36]. In this approximation we just redshift the quantities that define the Fermi-Dirac distribution. We will also discard the neutrino mass contribution in the distribution function, because in addition of being very tiny, it is also suppressed by a factor $(1+z)/(1+z_{\rm fo}) \ll 1$ (here z is an arbitrary redshift and $z_{\rm fo} \simeq 6\times 10^{10}$ is the redshift at neutrino freeze out). Hence, the important quantities are the redshifted neutrino momentum $p(z)$ and the redshifted neutrino temperature, which are respectively given by

$$p(z) = \frac{1+z}{1+z_{\rm fo}}\, p_{\rm fo}, \tag{3.23}$$

$$T_\nu(z) = \frac{1+z}{1+z_{\rm fo}}\, T_{\rm fo}. \tag{3.24}$$

Henceforth, the distribution function after decoupling is given by

$$f_{\rm FD}\left[p(z), T_\nu(z)\right] = \frac{1}{1+e^{p(z)/T_\nu(z)}}, \tag{3.25}$$

and, as usual, after integrating over all phase space, we find the redshifted number density

of neutrinos $n_\nu(z) = \int \frac{d^3p}{(2\pi)^3} f_{\rm FD}\left[p(z), T_\nu(z)\right]$. In addition, at the moment of neutrino freeze out we have that the entropy of neutrinos is exactly the same as the entropy of photons, i.e. $s_\nu(z_{\rm fo}) = s_\gamma(z_{\rm fo})$[1]. Hence, we can write the redshifting of the photon temperature as $T_\gamma(z) = \left(\frac{1+z}{1+z_{\rm fo}}\right)\left(\frac{g_*(z_{\rm fo})}{g_*(z)}\right)^{1/3} T_{\rm fo}$, and with the help of Eq. (3.24), we obtain the following expression that relates the present temperature of the photons (CMB) with the present temperature of the relic neutrinos (CνB),

$$T_\nu = \left(\frac{4}{11}\right)^{1/3} T_\gamma. \tag{3.26}$$

The current CMB temperature is measured to be $T_\gamma = 0.235$ meV [37; 38], and this leads to the indirect measurement $T_\nu = 0.168$ meV. By combining the latter result with Eq. (3.21), the present number density of neutrinos per flavor and spin is

$$n_0 \approx 56\,{\rm cm}^{-3}, \tag{3.27}$$

in such a way that the present number density of neutrinos for the entire CνB is expected to be $6\,n_0 \approx 336\,{\rm cm}^{-3}$. We can also explicitly compute the mean and the root mean square momentum

$$\begin{aligned} \langle p_\nu(z)\rangle &= \frac{\int \frac{d^3p}{(2\pi)^3}\, p(z)\, f_{\rm FD}\left[p(z), T_\nu(z)\right]}{n_\nu(z)} \\ &= \frac{7}{2}\frac{\zeta(4)}{\zeta(3)}\, T_\nu(z), \end{aligned} \tag{3.28}$$

$$\begin{aligned} \langle p_\nu^2(z)\rangle &= \frac{\int \frac{d^3p}{(2\pi)^3}\, p^2(z)\, f_{\rm FD}\left[p(z), T_\nu(z)\right]}{n_\nu(z)} \\ &= 15\,\frac{\zeta(5)}{\zeta(3)}\, T_\nu^2(z). \end{aligned} \tag{3.29}$$

In this way, the present root mean square momentum of neutrinos, $\overline{p}_\nu(0) = \sqrt{\langle p_\nu^2(0)\rangle}$, is

[1] The entropy density $s \equiv S/V$ for relativistic species is $s = \frac{2\pi^2}{45} g_{*\,s}(T) T^3$, where $g_{*\,s}(T) = \sum_{\rm bos} g_i \left(\frac{T_i}{T}\right)^3 + \frac{7}{8}\sum_{\rm fer} g_i \left(\frac{T_i}{T}\right)^3$.

computed to be

$$\overline{p}_\nu(0) \approx 0.603\,\text{meV}. \tag{3.30}$$

From this value of the root mean square momentum, we can infer a very important result. Because oscillation experiments showed that the neutrino masses are at most of the order of $\sim$ eV [33], we have that

$$\overline{p}_\nu(0) \ll m_\nu, \tag{3.31}$$

thus[1]:

Relic neutrinos are non-relativistic particles

We stress that we are considering as massive and degenerated at least two of the three active neutrinos. Knowing that high energy neutrinos interact very weakly with matter, what we should expect from the above conclusion is that relic neutrinos should be basically impossible to detect by direct detection experiments. Nevertheless, as we shall explain in Section 3.6, by using the tritium beta decay as a background, it shall be possible to detect signals of relic neutrinos by capturing them on a tritium target. With this in mind, the following section is devoted to understand how this is possible by analyzing the kinematic of the tritium beta decay, $^3\text{H} \to {}^3\text{He} + e^- + \overline{\nu}$, and the neutrino capture on tritium, $\nu + {}^3\text{H} \to {}^3\text{He} + e^-$.

3.5 Kinematic analysis

An important relation obtained by a simple kinematic analysis of tritium beta decay and neutrino capture on tritium is a shift in the kinetic spectrum of the beta decay. This shift in the spectrum depends on the neutrino mass. In the following computation we will use the rest frame of the tritium nucleus. In the tritium beta decay, see Fig. 3.4, the electron can be emitted within a range of momenta. For the electron to have maximum momentum, we must

[1] This is not necessarily true for the lightest one.

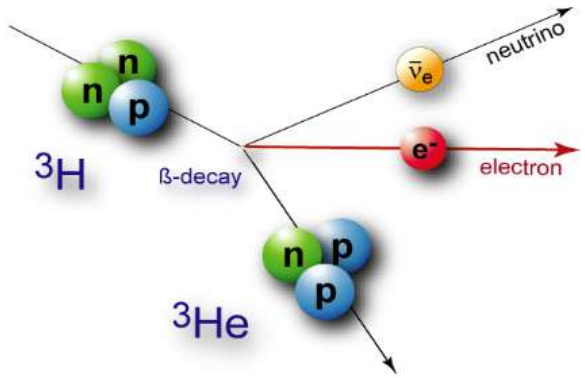

Figure 3.4: Schematic representation of tritium beta-decay, ${}^3\mathrm{H} \to {}^3\mathrm{He} + e^- + \overline{\nu}$ [39].

have the helium-3 and the neutrino going out anti-parallel to the direction of the electron. This situation determines the beta decay endpoint,

$$p_{\mathrm{end}} = \frac{1}{2m_{^3\mathrm{H}}}\sqrt{m_{^3\mathrm{H}}^2 - (m_{^3\mathrm{He}} + m_\nu + m_e)^2}\sqrt{m_{^3\mathrm{H}}^2 - (m_{^3\mathrm{He}} + m_\nu - m_e)^2}. \tag{3.32}$$

From this expression we can obtain the electron kinetic energy endpoint $K_{\mathrm{end}} = \sqrt{p_{\mathrm{end}}^2 + m_e^2} - m_e$. By replacing Eq. (3.32) inside K_{end}, we get

$$K_{\mathrm{end}} = \frac{(m_{^3\mathrm{H}} - m_e)^2 - (m_{^3\mathrm{He}} + m_\nu)^2}{2\, m_{^3\mathrm{H}}}. \tag{3.33}$$

Now, we want to adapt the above computation to the neutrino capture on tritium which is our case of interest,

$$\nu_j + {}^3\mathrm{H} \to {}^3\mathrm{He} + e^-, \tag{3.34}$$

where j is labeling neutrino mass eigenstates. Since, as we saw, typical cosmological neutrinos have $\overline{p}_\nu(0) \approx 6 \times 10^{-4}$ eV, and taking $m_j \approx 0.1$ eV, we neglect the momentum of the incident neutrino in the calculation of the electron kinetic energy. Following the same steps as in the

previous computation for the electron kinetic endpoint we arrive to

$$K_e^{\mathrm{C}\nu\mathrm{B},j} = \frac{(m_{^3\mathrm{H}} - m_e + m_j)^2 - m_{^3\mathrm{He}}^2}{2(m_{^3\mathrm{H}} + m_j)}. \tag{3.35}$$

This is the electron kinetic energy at which the signal of the relic neutrinos would appear. In order to understand how this signal would be detected in the tritium beta decay background, we have to consider the displacement in the energy spectrum. Hence, we have

$$\begin{aligned} \Delta K &= K_e^{\mathrm{C}\nu\mathrm{B},j} - K_{\mathrm{end}} \\ &= \left[\frac{(m_{^3\mathrm{H}} + m_{^3\mathrm{He}} + m_j)^2 - m_e^2}{2m_{^3\mathrm{H}}(m_{^3\mathrm{H}} + m_j)}\right] m_j. \end{aligned} \tag{3.36}$$

Considering that $m_{^3\mathrm{H}} \approx m_{^3\mathrm{He}} \gg m_e \gg m_j$, we arrive to the simple result

$$K_e^{\mathrm{C}\nu\mathrm{B},j} \approx K_{\mathrm{end}} + 2m_j, \tag{3.37}$$

which also means that $\Delta K \approx 2m_j$. This situation is schematically represented in Fig. 3.5. Additionally, for analysis of Fig. 3.5 it is convenient to recognize the form of the electron kinetic energy as $m_j \to 0$,

$$K_{\mathrm{end}}^0 = \frac{(m_{^3\mathrm{H}} - m_e)^2 - m_{^3\mathrm{He}}^2}{2\, m_{^3\mathrm{H}}}. \tag{3.38}$$

This would be the endpoint if neutrinos were massless particles.

3.6 PTOLEMY experiment

In 1962 Steven Weinberg proposed a way to detect relic neutrinos by capturing them on tritium [40], $\nu + {}^3\mathrm{H} \to {}^3\mathrm{He} + e$. The proposal was done in the context of degenerate massless relic neutrinos. Inspired by Weinberg's paper, Cocco, Mangano and Messina in [41] made a very extensive and detailed study of more than two thousands beta decaying nuclei, and found that the uncertainty on the neutrino capture by using a tritium target is constrained to the sub-percent level. In addition, they also found that the cross section times the neutrino

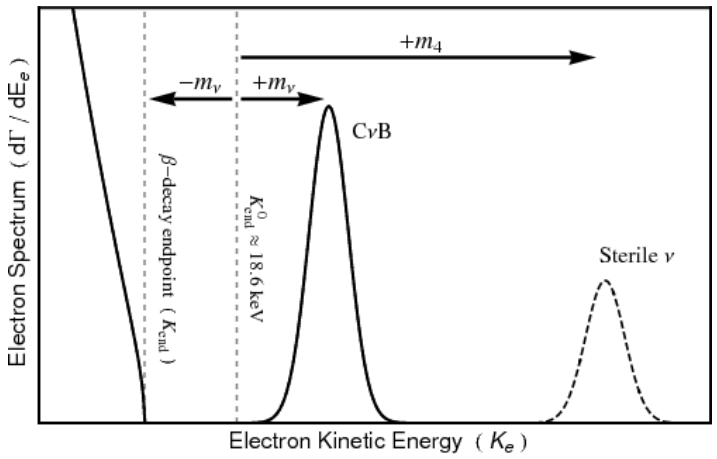

Figure 3.5: In this figure it is illustrated how the signal of the active relic neutrinos would appear as a solid line signal displaced $2\,m_\nu$ from the beta decay end point, we have to stress that in this cartoon it is considered that the masses of the three neutrinos are approximately degenerated $m_j = m_1 \approx m_2 \approx m_3 = m_\nu$. In the limit of $m_\nu = 0$ the electron kinetic energy end point, Eq. (3.38), would appear ending in the vertical gray dashed line. It is also schematically illustrated how the signal of a fourth sterile neutrino would appear [36].

velocity can be of the order of $10^{-42}\,\mathrm{cm}^2$. This implies that the event rate could be very large. For tritium they computed 10 events per year [41]. A more refined calculation [10] predicted 9.51 ± 0.03 events per year.

In 2013 a team of physicist revived this idea with the proposal of the PTOLEMY experiment [10] (Princeton Tritium Observatory for Light, Early-Universe, Massive-Neutrino Yield). The goal of direct detection of relic neutrinos is expected to be reached through a combination of a large area surface-deposition of ^{3}H, filter methods and cryogenic calorimetry. Fig. 3.6 shows schematically the electron trajectory in the PTOLEMY experiment, since electrons leave the Tritium surface-deposition until they arrive to the cryogenic calorimeter [10]. Because the implementation of the PTOLEMY experiment is a technological challenge, the implementation of a prototype is needed. The study of such a prototype shall allow to reach in the near future the goal of 100 gram of tritium target.

In order to validate every aspect in the construction and realization of this future experiment, the entire process has been divided in three main phases [11]:

1. Proof-of-principle demonstrator,

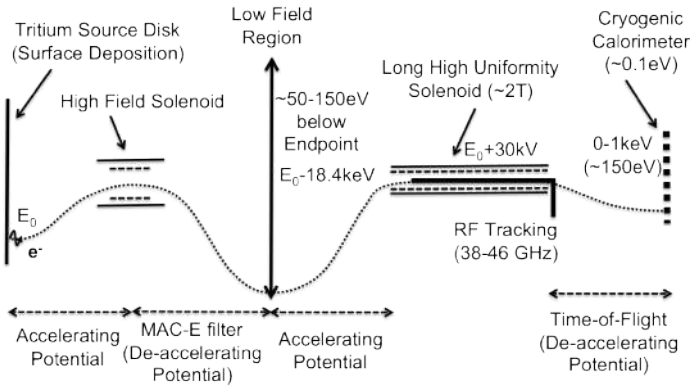

Figure 3.6: Schematic representation of the electron trajectory in the PTOLEMY experiment [10].

2. scalable prototype realization and tests,

3. full detector construction.

The first of these three steps started by moving the equipment and the PTOLEMY prototype from Princeton to the Laboratori Nazionali del Gran Sasso (LNGS) [11]. For the remaining steps we refer to Ref.[11] for more details. In the same reference it is possible to find a detailed time schedule for the installation and operation of the PTOLEMY prototype. However, for reasons beyond our knowledge that schedule (2018) is no longer valid. As the same authors of Ref.[11] describe in the more recent Ref.[42], the PTOLEMY prototype will be built at LNGS in this year, **2021**.

From now on we will be generic about the experiment, this means that in what follows we will focus on a generic PTOLEMY-*like* experiment.

In the following section we introduce the BSM effects trough out six dimensional operators. As we shall see this affect observables such as the capture rate of the neutrino capture by Tritium.

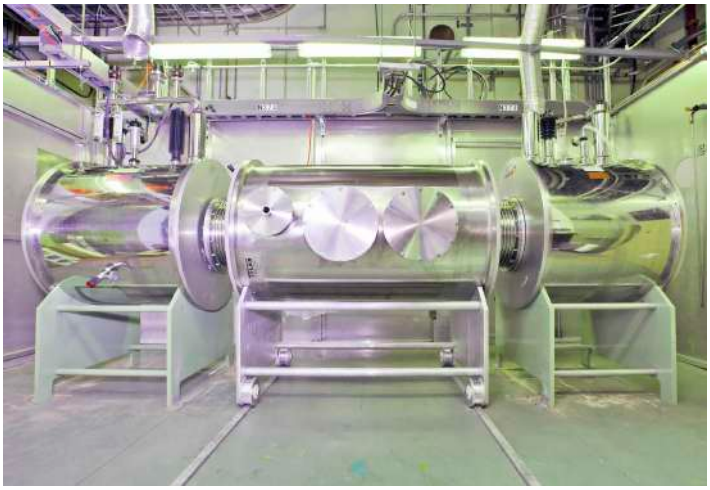

Figure 3.7: Prototype of the PTOLEMY experiment at the Princeton Plasma Physics Laboratory [10] (February, 2013).

Figure 3.8: Prototype of the PTOLEMY experiment at Jadwin Hall Physics Department, Princeton University [11] (June, 2017).

3.7 Impact of Beyond the Standard Model Physics in the Detection of the Cosmic Neutrino Background

3.7.1 Relation between capture rates of Dirac and Majorana neutrinos in the SM

Since we are interested in the capture of relic neutrinos on trititum, in a PTOLEMY-like experiment, the capture rate $\Gamma_{\mathrm{C}\nu\mathrm{B}}$ plays an important role. In Ref. [36] it is calculated the capture rate $\Gamma_{\mathrm{C}\nu\mathrm{B}}$ considering only SM interactions. Such expression is given by

$$\Gamma_{\mathrm{C}\nu\mathrm{B}}^{\mathrm{SM}} = \sum_{j=1}^{3} \left[\sigma_j(+1/2)\, v_{\nu_j}\, n_j(\nu_{h_R}) + \sigma_j(-1/2)\, v_{\nu_j}\, n_j(\nu_{h_L})\right]\, N_{\mathrm{T}}, \tag{3.39}$$

where N_{T} is the number of nuclei in the sample, σ_j and v_{ν_j} are the cross section and velocity for mass eigenstate j, respectively. The subscript h_R (h_L) of neutrino ν means right-helical (left-helical).

Helicity plays an important role in the description of processes involving relic neutrinos. Since in the present relic neutrinos are non-relativistic, chirality and helicity do not coincide. While chirality is not conserved in this regime, helicity commutes with the free hamiltonian and then is a conserved quantity. In contrast, during the neutrino freezeout ($T_{\mathrm{fo}} \gg m_\nu$), neutrinos were ultra-relativistic and thus chirality and helicity coincide. In this scenario, for Dirac neutrinos, we have that only LH neutrinos, or RH anti-neutrinos (the active states) contribute to the processes showed in Figs. 3.2 and 3.3. Hence, these active states have a relic abundance $n_\nu(z)$. In contrast, RH sterile neutrinos and LH sterile anti-neutrinos cannot come into thermal equilibrium with SM, thus their relic abundances are assumed to be negligible [36]. This situation is summarized in table 3.2.

As discussed in subsection 3.2.2, Majorana neutrinos are their own antiparticles. For that reason, the names “neutrino” or “anti-neutrino” are avoided for their classification. Instead, we classify them by their handness, and as active or sterile particles, see table 3.3. As in the Dirac case, the active neutrinos ν_L and ν_R interact weakly, and thus they have also a relic abundance $n_\nu(z)$. Now, in addition to ν_L and ν_R there are two sterile neutrinos, N_R and N_L.

Dirac Neutrinos		Abundances
ν		$n(\nu)$
ν_L	LH active neutrino	$n(\nu_L) = n_\nu(z)$
$\overline{\nu}_R$	RH active anti-neutrino	$n(\overline{\nu}_R) = n_\nu(z)$
ν_R	RH sterile neutrino	$n(\nu_R) \approx 0$
$\overline{\nu}_L$	LH sterile anti-neutrino	$n(\overline{\nu}_L) \approx 0$

Table 3.2: For the Dirac case only LH neutrinos, or RH anti-neutrinos (the active states) contribute to the processes of Figs. 3.2 and 3.3. Hence, these active states have shifted relic abundance $n_\nu(z)$. In a contrary manner for RH sterile neutrinos and LH sterile anti-neutrinos, because they cannot come into thermal equilibrium with SM, their relic abundance is assumed to be negligible [36].

Majorana Neutrino		Abundances
ν		$n(\nu)$
ν_L	LH active neutrino	$n(\nu_L) = n_\nu(z)$
ν_R	RH active neutrino	$n(\overline{\nu}_R) = n_\nu(z)$
N_R	RH sterile neutrino	$n(N_R) = 0$
N_L	LH sterile neutrino	$n(N_L) = 0$

Table 3.3: Left-side of the table shows the classification of Majorana neutrinos by their handedness and if they are active or sterile. Right-side of the table shows their respective abundances $n_\nu(z)$ [36].

However, N_R and N_L are typically heavier than the weak scale [43]. Therefore, they shall decay in lighter particles such as leptons and Higgs bosons at the EW scale [36]. In this way, their relic abundance is expected to be zero, see table 3.3.

As said before, relic neutrinos today are non-relativistic. The importance of helicity in this regime was also stressed. Hence, in the non-relativistic regime neutrinos are labelled by the following subscripts: h_L and h_R, which mean left-helical and right-helical, respectively. In table 3.4, we show the respective relic abundances for the Dirac and Majorana cases. The subscript "0" in the abundance n_0 means that they are the present abundances. With the definitions at hand, now we compute the capture rates for Dirac and Majorana relic neutrinos.

Dirac	Majorana
$n(\nu)$	$n(\nu)$
$n(\nu_{h_L}) = n_0$	$n(\nu_{h_L}) = n_0$
$n(\overline{\nu}_{h_R}) = n_0$	$n(\nu_{h_R}) = n_0$
$n(\nu_{h_R}) \approx 0$	$n(N_{h_R}) = 0$
$n(\overline{\nu}_{h_L}) \approx 0$	$n(N_{h_L}) = 0$

Table 3.4: Here we show the notation for the present relic abundances for Dirac and Majorana neutrinos.

After summing over the mass eigenstates $j = 1, 2, 3$, Eq. (3.39) becomes

$$\Gamma^{\rm SM}_{\rm C\nu B} = \overline{\sigma}\,[n(\nu_{h_R}) + n(\nu_{h_L})]\,N_{\rm T} \tag{3.40}$$

where $\overline{\sigma} = \sum_{j=1,2,3} \sigma_j(s_\nu = \pm 1/2)\, v_{\nu_j}\Big|_{v_{\nu_j} \ll 1}$ and has the numerical value of $\overline{\sigma} \simeq 3.834 \times 10^{-45}\,{\rm cm}^2$ [36]. As a result, Eq. (3.40) gives

$$\Gamma^{\rm SM}_{\rm C\nu B} = n_0\,\overline{\sigma}\,N_{\rm T}, \text{ Dirac case} \tag{3.41}$$

$$\Gamma^{\rm SM}_{\rm C\nu B} = 2\,n_0\,\overline{\sigma}\,N_{\rm T}, \text{ Majorana case.} \tag{3.42}$$

Thus, the capture rate depends on the nature of relic neutrinos. In this way, in the SM the capture rate for Majorana relic neutrinos, $\Gamma^{\rm M}_{\rm C\nu B}$, is expected to be twice the value of Dirac relic neutrinos, $\Gamma^{\rm D}_{\rm C\nu B}$, so we write

$$\Gamma^{\rm M}_{\rm C\nu B} = 2\,\Gamma^{\rm D}_{\rm C\nu B}. \tag{3.43}$$

In the rest of the chapter we will analyze how the introduction of new physics would modify the relation given in Eq. (3.43).

3.7.2 Effective lagrangian approach for the BSM neutrino interactions

In the SM, the weak interactions have a purely $V - A$ Lorentz structure. Since the simple fact that neutrinos have a non-zero mass constitutes already an evidence for BSM physics,

Four-fermion Operators		Vertex Corrections
$Q^{(6)}_{\nu_L}$	$Q^{(6)}_{\nu_R}$	$Q^{(6)}_{\Phi}$
$Q_1 = (\overline{l_L} e_R)(\overline{d_R} q_L)$	$Q_5 = (\overline{l_L}\nu_R)\varepsilon(\overline{q_L} d_R)$	$Q_9 = i(\Phi^T \varepsilon D_\mu \Phi)(\overline{u_R}\gamma_\mu d_R)$
$Q_2 = (\overline{l_L} e_R)\varepsilon(\overline{q_L} u_R)$	$Q_6 = (\overline{\nu_R} l_L)(\overline{q_L} u_R)$	$Q_{10} = i(\Phi^T \varepsilon D_\mu \Phi)(\overline{\nu_R}\gamma^\mu e_R)$
$Q_3 = (\overline{l_L}\gamma^\mu \tau^A l_L)(\overline{q_L}\gamma_\mu \tau^A q_L)$	$Q_7 = (\overline{e_R}\gamma^\mu \nu_R)(\overline{u_R}\gamma_\mu d_R)$	$Q_{11} = (\Phi^\dagger i \overleftrightarrow{D^a_\mu} \Phi)(\overline{q_L}\gamma_\mu \tau^A q_L)$
$Q_4 = (\overline{l_L}\sigma^{\mu\rho} e_R)\varepsilon(\overline{q_L}\sigma_{\mu\rho} u_R)$	$Q_8 = (\overline{l_L}\sigma^{\mu\rho}\nu_R)\varepsilon(\overline{q_L}\sigma_{\mu\rho} d_R)$	$Q_{12} = (\Phi^\dagger i \overleftrightarrow{D^a_\mu} \Phi)(\overline{l_L}\gamma^\mu \tau^A l_L)$

Table 3.5: Dimension-six operators relevant for neutrino capture. Here l_L, q_L are the SM lepton and quark $\mathrm{SU}(2)_L$ doublets while u_R, d_R, e_R, ν_R are the corresponding SM singlets. The $\mathrm{SU}(2)_L$ generators are denoted with τ^A while ε_{ij} is the totally antisymmetric tensor with $\varepsilon_{12} = +1$. We do not include the invariant operator $(\overline{\nu_R}\sigma^{\mu\rho} l_L)(\overline{q_L}\sigma_{\mu\rho} u_R)$ in the list because it does not contribute to the relic capture.

we will allow here for other possibilities. This can be done in a model independent fashion using an effective field theory approach. We will consider dimension-six operators which are $\mathrm{SU}(2)_L \times \mathrm{U}(1)_Y$ invariant, but which also include right-handed neutrinos [16; 44; 45]. More precisely, we write

$$\mathscr{L}_{\mathrm{BSM}} = \mathscr{L}^{(4)}_{\mathrm{SM}} + \mathscr{L}_{m_\nu} + \frac{1}{\Lambda^2}\sum_{k=1}^{12} c^{(6)}_k Q^{(6)}_k, \tag{3.44}$$

where $\mathscr{L}^{(4)}_{\mathrm{SM}}$ is the dimension-four SM lagrangian, $\mathscr{L}_{m_\nu}$ is the neutrino mass lagrangian, which can either come from a dimension 4 operator involving right handed neutrinos or from the dimension 5 Weinberg operator; Λ is the maximum energy scale at which the theory is still valid; and the $c^{(6)}_k$ are dimensionless coupling constants. The set of operators with left- and right-handed neutrinos, $Q^{(6)}_k = \{Q^{(6)}_k(\nu_L), Q^{(6)}_k(\nu_R)\}$, is given in table 3.5. The terms relevant for our calculation of the BSM relic neutrino capture rate on β-decaying tritium can be obtained writing eq. (3.44) in terms of mass eigenstates

$$\mathscr{L}_{\mathrm{eff}} = -\frac{G_F}{\sqrt{2}} V_{ud}\, U_{ej} \left\{ [\bar{e}\gamma^\mu(1-\gamma^5)\nu_j][\bar{u}\gamma_\mu(1-\gamma^5)d] + \sum_{l,q} \epsilon_{lq}[\bar{e}\mathscr{O}_l \nu_j][\bar{u}\mathscr{O}_q d] \right\} + \mathrm{h.c.}, \tag{3.45}$$

where a sum over the three neutrino mass eigenstates $j = 1, 2, 3$ is implied. The couplings ϵ_{lq}, related to the dimensionless couplings $c_k^{(6)}$ (see ref. [44]), parametrize the BSM physics effects, with l (q) labelling the Lorentz structure of the lepton (quark) current, as given by $\mathscr{O}_l$ ($\mathscr{O}_q$) in table 3.6. V_{ud} and U_{ej} correspond to the Cabibbo-Kobayashi-Maskawa (CKM) and Pontecorvo-Maki-Nakagawa-Sakata (PMNS) mixing matrices elements relevant to the process, respectively.

Equation (3.45) can be used to calculate the neutrino absorption on tritium

$$\nu_j + {}^3\mathrm{H} \rightarrow {}^3\mathrm{He} + e^- ,$$

in the presence of BSM interactions. To this end, we need to properly define the hadronic matrix elements involving the quark current in eq. (3.45). Following ref. [46], we have

$$\begin{aligned}
\langle p(p_p)|\bar{u}\gamma^\mu(1\pm\gamma^5)d|n(p_n)\rangle &= \overline{u_p}(p_p)\gamma^\mu[g_V(q^2)\pm g_A(q^2)\gamma^5]u_n(p_n),\\
\langle p(p_p)|\bar{u}d|n(p_n)\rangle &= g_S(q^2)\,\overline{u_p}(p_p)\,u_n(p_n),\\
\langle p(p_p)|\bar{u}\gamma^5 d|n(p_n)\rangle &= g_P(q^2)\,\overline{u_p}(p_p)\gamma^5 u_n(p_n),\\
\langle p(p_p)|\bar{u}\sigma^{\mu\nu}(1\pm\gamma^5)d|n(p_n)\rangle &= g_T(q^2)\,\overline{u_p}(p_p)\sigma^{\mu\nu}(1\pm\gamma^5)u_n(p_n).
\end{aligned} \tag{3.46}$$

We have introduced the hadronic form factors $g_h(q^2)$, with $h = V, A, S, P, T$ corresponding to the vector, axial, scalar, pseudoscalar and tensor Lorentz structures, respectively.[1] Although these form factors depend on the transferred momentum $q^2 = (p_n - p_p)^2$, for the capture rate we are only interested in the $q^2 \simeq 0$ limit. In our numerical analysis we will use the values shown in table 3.7 [47; 48; 49]. Following the calculation of ref. [36], the capture cross section for a neutrino mass eigenstate j, with helicity $h_j = \pm 1$ and velocity v_j including BSM effects is given by

$$\sigma_j^{\mathrm{BSM}}(h_j)v_j = \frac{G_F^2}{2\pi}\,|V_{ud}|^2\,|U_{ej}|^2\,F_Z(E_e)\,\frac{m_{^3\mathrm{He}}}{m_{^3\mathrm{H}}}E_e\,p_e\,T_j(h_j,\epsilon_{lq}), \tag{3.47}$$

[1] Since it does not contribute to the CνB capture, we do not include the weak magnetic term

$$\langle p(p_p)|\bar{u}\gamma_\mu d|n(p_n)\rangle_{\mathrm{WM}} = -i\frac{g_{\mathrm{WM}}}{2M_N}\overline{u_p}(p_p)\sigma_{\mu\nu}(p_n - p_p)^\nu u_n(p_n).$$

ϵ_{lq}	$\mathscr{O}_l$	$\mathscr{O}_q$
ϵ_{LL}	$\gamma^\mu(1-\gamma^5)$	$\gamma_\mu(1-\gamma^5)$
ϵ_{LR}	$\gamma^\mu(1-\gamma^5)$	$\gamma_\mu(1+\gamma^5)$
ϵ_{RL}	$\gamma^\mu(1+\gamma^5)$	$\gamma_\mu(1-\gamma^5)$
ϵ_{RR}	$\gamma^\mu(1+\gamma^5)$	$\gamma_\mu(1+\gamma^5)$
ϵ_{LS}	$1-\gamma^5$	1
ϵ_{RS}	$1+\gamma^5$	1
ϵ_{LP}	$1-\gamma^5$	$-\gamma^5$
ϵ_{RP}	$1+\gamma^5$	$-\gamma^5$
ϵ_{LT}	$\sigma^{\mu\nu}(1-\gamma^5)$	$\sigma_{\mu\nu}(1-\gamma^5)$
ϵ_{RT}	$\sigma^{\mu\nu}(1+\gamma^5)$	$\sigma_{\mu\nu}(1+\gamma^5)$

Table 3.6: Parameters and their corresponding Lorentz structures for the BSM currents considered in this work.

where $m_{^3\mathrm{He}}$ and $m_{^3\mathrm{H}}$ are the helium and tritium masses, and E_e, m_e, p_e are the electron energy, mass and momentum, respectively. The $T_j(h_j, \epsilon_{lq})$ function contains the dependence on the neutrino helicity and on the ϵ_{lq} parameters,

$$
\begin{aligned}
T_j(h_j,\epsilon_{lq}) = \mathcal{A}(h_j)\Big[& g_V^2\,(\epsilon_{LL}+\epsilon_{LR}+1)^2 + 3\,g_A^2\,(\epsilon_{LL}-\epsilon_{LR}+1)^2 + g_S^2\,\epsilon_{LS}^2 + 48\,g_T^2\,\epsilon_{LT}^2 \\
& + \frac{2m_e}{E_e}\left[g_S\,g_V\,\epsilon_{LS}\,(\epsilon_{LL}+\epsilon_{LR}+1) - 12\,g_A\,g_T\,\epsilon_{LT}\,(\epsilon_{LL}-\epsilon_{LR}+1)\right]\Big] \\
+ \mathcal{A}(-h_j)\Big[& g_V^2\,(\epsilon_{RR}+\epsilon_{RL})^2 + 3\,g_A^2\,(\epsilon_{RR}-\epsilon_{RL})^2 + g_S^2\,\epsilon_{RS}^2 + 48\,g_T^2\,\epsilon_{RT}^2 \\
& + \frac{2m_e}{E_e}\left[g_S\,g_V\,\epsilon_{RS}\,(\epsilon_{RR}+\epsilon_{RL}) - 12\,g_A\,g_T\,\epsilon_{RT}\,(\epsilon_{RR}-\epsilon_{RL})\right]\Big] \\
+ 2\,\frac{m_j}{E_j}\,\{ & g_S\,g_V\,\epsilon_{RS}\,(\epsilon_{LL}+\epsilon_{LR}+1) + \epsilon_{LS}\,(\epsilon_{RR}+\epsilon_{RL})) \\
& -12\,g_A\,g_T(\epsilon_{RT}\,(\epsilon_{LL}-\epsilon_{LR}+1) + \epsilon_{LT}\,(\epsilon_{RR}-\epsilon_{RL}))\} \\
+ 2\,\frac{m_j m_e}{E_j E_e}\,\big\{ & g_V^2\,(\epsilon_{LL}+\epsilon_{LR}+1)(\epsilon_{RR}+\epsilon_{RL}) + 3\,g_A^2\,(\epsilon_{LL}-\epsilon_{LR}+1)(\epsilon_{RR}-\epsilon_{RL}) \\
& + g_S^2\,\epsilon_{RS}\,\epsilon_{LS} + 48\,g_T^2\,\epsilon_{RT}\,\epsilon_{LT}\big\}\,,
\end{aligned}
\tag{3.48}
$$

with m_j, E_j the mass and energy of the j-th neutrino mass eigenstate and $\mathcal{A}(h_j) = 1 - 2h_j v_j$.

Form Factor	Value	Reference
$g_V(0)$	1	[50; 51]
$g_A(0)/g_V(0)$	1.2646 ± 0.0035	[47]
$g_S(0)$	1.02 ± 0.11	[48]
$g_P(0)$	349 ± 9	[48]
$g_T(0)$	1.020 ± 0.076	[49]

Table 3.7: Hadronic form factors considered in this work.

Let us note that $\mathcal{A}(h_j) \simeq 1$ for non-relativistic neutrinos, corresponding to the case on which we will focus in section 3.7.3. Furthermore, notice that the capture rate is independent of the pseudoscalar couplings ϵ_{lP}. The Fermi function $F_Z(E_e)$, which takes cares of the enhancement of the cross section due to the Coulomb attraction between the proton and electron, is given by

$$F_Z(E_e) = \frac{2\pi Z\alpha E_e}{p_e\left[1 - e^{\frac{-2\pi Z\alpha E_e}{p_e}}\right]}\,. \tag{3.49}$$

Summing over all the neutrino mass eigenstates, one can calculate the total ^{3}H capture rate

$$\Gamma^{\rm BSM}_{\rm C\nu B} = N_T \sum_{j=1}^{3} \Gamma^{\rm BSM}_{\rm C\nu B}(j) = N_T \sum_{j=1}^{3} \left[\sigma_j^{\rm BSM}(+1)\, v_j\, n_{\nu_+^j} + \sigma_j^{\rm BSM}(-1)\, v_j\, n_{\nu_-^j}\right], \tag{3.50}$$

where N_T is the number of nuclei present in the sample and $n_{\nu_\pm^j}$ the number density at the present time of the helical state $\nu_\pm^j$.

3.7.3 Detection of the CνB by a PTOLEMY-like detector

As discussed in Section 3.6 a PTOLEMY-like experiment [10] aims to detect the CνB through the neutrino capture by tritium, a reaction that has no energy threshold. We can safely assume that CνB neutrinos are non-relativistic today[1] as their root mean momentum is $\overline{p}_\nu(0) \approx 0.6$ meV $\ll m_j$ [40]. This has two crucial consequences. First, the neutrino flavour eigenstates have suffered decoherence into their mass eigenstates, so a detector would, in

[1] As we know from oscillation experiments, only one neutrino can be massless.

fact, measure the contribution of each neutrino mass eigenstate. Second, at the time of the creation of the CνB, i.e. when neutrinos decoupled from the primordial plasma, they were ultrarelativistic, making chiral and helical eigenstates effectively equal. However, as neutrinos evolved into a non-relativistic state due to the expansion of the Universe, chirality and helicity became different. Since neutrinos were free streaming, it was helicity, not chirality, that was conserved in the process.[1] This implies that the neutrino number density is $n_{\nu_+^j} = n_{\nu_-^j} = n_0 \approx 56\ \mathrm{cm}^{-3}$ in the Majorana case, while $n_{\nu_-^j} = n_0$ and $n_{\nu_+^j} = 0$ in the Dirac case. If no BSM interactions are present, the function $T_j(h_j, \epsilon_{lq})$ reduces to

$$T_j(h_j, 0) = \mathcal{A}(h_j)\left[g_V^2 + 3\, g_A^2\right],$$

from which, using eq. (3.50), we conclude that

$$\Gamma^{\mathrm{M}}_{\mathrm{C}\nu\mathrm{B}} = 2\,\Gamma^{\mathrm{D}}_{\mathrm{C}\nu\mathrm{B}} = 85.7\ [\mathrm{kg\,yr}]^{-1}, \tag{3.51}$$

where $\Gamma^{\mathrm{M}}_{\mathrm{C}\nu\mathrm{B}}$ and $\Gamma^{\mathrm{D}}_{\mathrm{C}\nu\mathrm{B}}$ are the Majorana and Dirac capture rates. We will consider in section 3.7.5 the modifications to the neutrino abundance due to BSM physics.

The signature of relic neutrinos in a PTOLEMY-like detector is given by the electron created in the capture process. Nonetheless, tritium can also undergo β-decay, giving rise to a continuous electron spectrum. As a consequence, one needs to discriminate the electrons produced by the CνB neutrino capture from the electrons produced by β-decays. Using kinematics, the electrons produced by the ν_j relic neutrinos capture will have a definite energy [36] (see the discussion in Section 3.5)

$$E_e^{\mathrm{C}\nu\mathrm{B},j} \simeq m_e + K^0_{\mathrm{end}} + 2\, m_j, \tag{3.52}$$

where K^0_{end} corresponds to the β-decay endpoint energy. This implies that relic neutrinos could produce one or more peaks in the electron energy spectrum at energies larger than the endpoint one. If so, CνB and β-decay events can in principle be discriminated from each

[1] If neutrinos underwent a clustering process, helicity would not be conserved either. We will comment more on this possibility in section 3.7.5.

other. It is clear that the finite energy resolution of the real detector plays an essential role in establishing whether the two signals can be separated or not. In order to estimate the signal in a more realistic way we will follow [36] and convolute the CνB capture rate of eq. (3.50) and the β-decay background with a Gaussian function

$$\frac{d\Gamma^{\rm BSM}_{\rm C\nu B}}{dE_e} = \frac{1}{\sqrt{2\pi\sigma^2}} \sum_{j=1}^{3} \int_{-\infty}^{\infty} dE'_e\, \Gamma^{\rm BSM}_{\rm C\nu B}(j)\, \exp\left[-\frac{(E'_e - E_e)^2}{2\sigma^2}\right] \delta(E'_e - E_e^{{\rm C\nu B},j}), \tag{3.53a}$$

$$\frac{d\Gamma_\beta}{dE_e} = \frac{1}{\sqrt{2\pi\sigma^2}} \int_{-\infty}^{\infty} dE'_e\, \frac{d\Gamma_\beta}{dE'_e}\, \exp\left[-\frac{(E'_e - E_e)^2}{2\sigma^2}\right], \tag{3.53b}$$

where σ is the expected experimental energy resolution. The complete expression for the β-decay rate $\dfrac{d\Gamma_\beta}{dE'_e}$ is [46]

$$\begin{aligned} \frac{d\Gamma_\beta}{dE'_e} &= \frac{2G_F^2 \left|V_{ud}\right|^2}{\pi^3} p_e\, E'_e \left(m_{^3{\rm H}} - m_{^3{\rm He}} - E'_e\right)^2 \times \\ &\times \left(\sum_j |U_{ej}|^2 \sqrt{1 - \frac{m_j^2}{\left(m_{^3{\rm H}} - m_{^3{\rm He}} - E'_e\right)^2}}\, \widetilde{\Theta}_j \right) \end{aligned} \tag{3.54}$$

where $\widetilde{\Theta}_j \equiv \Theta\left(E_e^{\rm max}(m_j) - E'_e\right)\Theta\left(m_{^3{\rm H}} - m_{^3{\rm He}} - m_e - m_j\right)$ and $E_e^{\rm max} = \frac{m_{^3{\rm H}}^2 + m_e^2 - \left(m_{^3{\rm He}} + m_j\right)^2}{2m_{^3{\rm H}}}$. In order to estimate the total number of events produced by the CνB and β-decay in the region in which we expect a CνB signal, we define the full width at half maximum (FWHM) of the Gaussian function as $\Delta = \sqrt{8\ln 2}\,\sigma$. With this definition, we have

$$\mathcal{N}^{\rm BSM}_{\rm C\nu B}(\Delta) = \int_{E_e^{\rm C\nu B} - \Delta/2}^{E_e^{\rm C\nu B} + \Delta/2} dE_e \frac{d\Gamma^{\rm BSM}_{\rm C\nu B}}{dE_e}, \tag{3.55a}$$

$$\mathcal{N}_\beta(\Delta) = \int_{E_e^{\rm C\nu B} - \Delta/2}^{E_e^{\rm C\nu B} + \Delta/2} dE_e \frac{d\Gamma_\beta}{dE_e}, \tag{3.55b}$$

which can be used to define the ratio

$$r_{\rm C\nu B} = \frac{\mathcal{N}^{\rm BSM}_{\rm C\nu B}(\Delta)}{\sqrt{\mathcal{N}_\beta(\Delta)}}. \tag{3.56}$$

We will consider that the signal can be discriminated from the background when $r_{\rm C\nu B} \geq 5$.

The future PTOLEMY experiment is expected to have $\Delta = 0.15$ eV [10] in such a way that a single peak is expected if the sum of the neutrino masses is about 0.1 eV. For smaller masses, a smaller value of Δ would be needed to discriminate the signal from the background. We study more in detail the interplay between Δ, neutrino masses and the position of the peaks observed at PTOLEMY-like detectors in Appendix B.

3.7.4 On the contributions of BSM physics to CνB capture rate

The BSM lagrangian of eq. (3.45) generates not only new contributions to the neutrino capture by tritium, but also modifies other low energy processes. To assess the size of the modification to the neutrino CνB capture rate, we first need to take into account the experimental bounds on the ϵ_{lq} coefficients. Limits from Cabbibo Universality [52], radiative pion decay [53] and neutron decays [54] put bounds on the ϵ_{Lq} left-chiral couplings; meanwhile, limits coming from the β-decay of several nuclei have been reviewed in ref. [55]. A complete compendium of the limits regarding low energy decays is given in refs. [44; 45]. For our purposes, we will consider the cases considered in ref. [55], as they include couplings with right-handed neutrinos. The constraints are given in terms of the following combinations of couplings:

$$\begin{aligned}
C_V &= g_V(1+\epsilon_{LL}+\epsilon_{LR}+\epsilon_{RL}+\epsilon_{RR}), & C'_V &= g_V(1+\epsilon_{LL}+\epsilon_{LR}-\epsilon_{RL}-\epsilon_{RR}),\\
C_A &= -g_A(1+\epsilon_{LL}-\epsilon_{LR}-\epsilon_{RL}+\epsilon_{RR}), & C'_A &= -g_A(1+\epsilon_{LL}-\epsilon_{LR}+\epsilon_{RL}-\epsilon_{RR}),\\
C_S &= g_S(\epsilon_{LS}+\epsilon_{RS}), & C'_S &= g_S(\epsilon_{LS}-\epsilon_{RS}),\\
C_T &= 4\,g_T(\epsilon_{LT}+\epsilon_{RT}), & C'_T &= 4\,g_T(\epsilon_{LT}-\epsilon_{RT}).
\end{aligned} \tag{3.57}$$

Accordingly, we need to convert the bounds on the $C_i^{(\prime)}$ into bounds on ϵ_{lq} at 3σ C.L. To this end, we have performed a scan over the ranges

$$\begin{aligned}
-10^{-3} \leq &\epsilon_{LL} \leq 10^{-3}\,, & -10^{-3} \leq &\epsilon_{LR} \leq 10^{-3}\,,\\
-2.8\times 10^{-3} \leq &\epsilon_{LS} \leq 5\times 10^{-3}\,, & -2\times 10^{-3} \leq &\epsilon_{LT} \leq 2.1\times 10^{-3}\,,
\end{aligned} \tag{3.58}$$

and

$$|\epsilon_{Rq}| \leq 10^{-1}, \tag{3.59}$$

keeping only the points consistent with each of the allowed regions of the $C_h^{(\prime)}$ in ref. [55]. Let us notice that, to translate the limits into contraints on the ϵ_{lq} parameters, we also scanned over the $g_A(0)/g_V(0)$ value given in table 3.7 since such parameter is affected by the presence of BSM [56]. The ranges in which the scan is performed have been chosen to include the constraints of refs. [52; 53; 54] in the left-chiral coefficients at the 3σ level. Although stronger limits can be imposed on right-handed couplings using pion decay [57], we will not include them as they are strongly dependent on the flavour structure of the model [44; 45]. Finally, LHC bounds coming from $pp \to e + X + \not{E}_T$ have been studied in refs. [44; 54]. However, the analysis is performed supposing the interactions of eq. (3.45) remain pointlike up to the LHC energies, i.e. up to a few TeV. To allow for the possibility that BSM physics appears just above the electroweak scale, in our analysis we will use only the bounds coming from low energy experiments.

We found that the parameters ϵ_{LL} and ϵ_{LR} are unconstrained by the experimental data as it has been previously noted in ref. [56]. For reference we summarize here the bounds without the correlations — which have been included in our numerical analysis — :

1. *Only left-chiral couplings* allowed in the fit ($\epsilon_{Rq} = 0$). The scalar and tensor terms have distinct dependence on the electron energy and mass, because of the different Lorentz structure. Computing the total capture rate $\Gamma_{\mathrm{C}\nu\mathrm{B}}^{BSM}$ using the points that pass the low energy experimental constraints, we find

$$0.985\,\Gamma_{\mathrm{C}\nu\mathrm{B}}^{\mathrm{D}} \lesssim \Gamma_{\mathrm{C}\nu\mathrm{B}}^{\mathrm{BSM}} \lesssim 1.02\,\Gamma_{\mathrm{C}\nu\mathrm{B}}^{\mathrm{D}},$$

   where $\Gamma_{\mathrm{C}\nu\mathrm{B}}^{D}$ is the capture rate for Dirac neutrinos with only SM interactions.

2. *Only vector-axial-vector couplings* allowed in the fit ($\epsilon_{LS} = \epsilon_{RS} = \epsilon_{LT} = \epsilon_{RT} = 0$): in this case we get $|\epsilon_{RL}| \lesssim 8 \times 10^{-2}$ and $|\epsilon_{RR}| \lesssim 5 \times 10^{-2}$ at 3σ level. Let us notice that

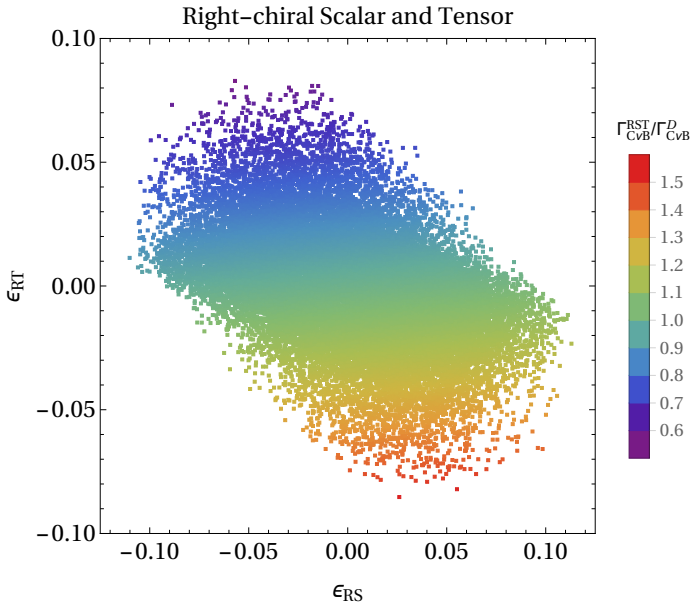

Figure 3.9: Ratio between the BSM capture rate for the right-chiral scalar and tensor couplings scenario with respect to the SM Dirac case in the plane (ϵ_{RS} versus ϵ_{RT}). We use a color code to indicate the range of values of the ratio.

the term linear in the right-handed couplings in eq. (3.48) is proportional to m_j/E_j, so it would be negligible for an ultrarelativistic neutrino. This term comes from the interference of the SM contribution with the right-handed neutrino current. The terms proportional to $(\epsilon_{RR} \pm \epsilon_{RL})^2$ come from the square of the right-handed currents, and are proportional to $\mathcal{A}(-h_j)$. Using the experimentally allowed range for $\epsilon_{RR,RL}$, we find

$$0.89\,\Gamma^{\rm D}_{C\nu B} \lesssim \Gamma^{\rm BSM}_{C\nu B} \lesssim 1.11\,\Gamma^{\rm D}_{C\nu B}.$$

3. *Only right-chiral scalar and tensor couplings* allowed in the fit ($\epsilon_{LS} = \epsilon_{LT} = \epsilon_{RL} = \epsilon_{RR} = 0$): in this case we get $|\epsilon_{RS}| \lesssim 1.1 \times 10^{-1}$ and $|\epsilon_{RT}| \lesssim 8 \times 10^{-2}$ at 3σ. Again the term proportional to the neutrino mass comes from the interference between SM and right-handed currents. Furthermore, we observe that this interference term does not depend on the neutrino helicity. This is due to the different Lorentz structures that

appear in the BSM lagrangian. Considering the allowed parameter space, we find

$$0.61\,\Gamma^{\rm D}_{\rm C\nu B} \lesssim \Gamma^{\rm BSM}_{\rm C\nu B} \lesssim 1.52\,\Gamma^{\rm D}_{\rm C\nu B}.$$

Since in this case the parameter space is highly correlated due to the correlations coming from the β-decay bounds, we show in figure 3.9 the rate between the BSM capture rate and the SM Dirac case in the $(\epsilon_{RS}, \epsilon_{RT})$ plane.

4. *Five free couplings* allowed in the fit: in this case we get $|\epsilon_{RS}| \lesssim 10^{-1}$ and $|\epsilon_{RT}| \lesssim 8 \times 10^{-2}$ at 3σ. Here the interference term proportional to the neutrino mass depends on the product between $\epsilon_{LS,LT}$ and $\epsilon_{RS,RT}$. We show in figure 3.10 the ratio between the BSM capture rate and the SM Dirac rate in the $(\epsilon_{RS}, \epsilon_{RT})$ plane, in which we find the strongest correlation between the couplings. We find that the ratio can be at the most 2.2 times the SM one, which is interesting as in this case Dirac neutrinos with BSM interactions can mimic Majorana neutrinos in the SM. However, there are regions in parameter space in which the rate is considerably lower than the SM one.

Let us conclude stressing that pure Majorana neutrinos fall in the "only left-chiral couplings" category (case 1 above), with only a small modification of order 2% allowed in the capture rate. Dirac neutrinos have instead a much richer phenomenology, with all the above cases possible (depending on the gauge invariant operators of table 3.5 generated in the UV theory). On the other hand, one could also worry about possible modifications of the tritium β-decay spectrum generated by BSM interactions, which could make the CνB detection more involved. Nevertheless, it has been shown in ref. [46] that the endpoint of the β-decay spectrum is not significantly modified by BSM physics; thus, in principle, relic neutrino detection would be still possible in this case.

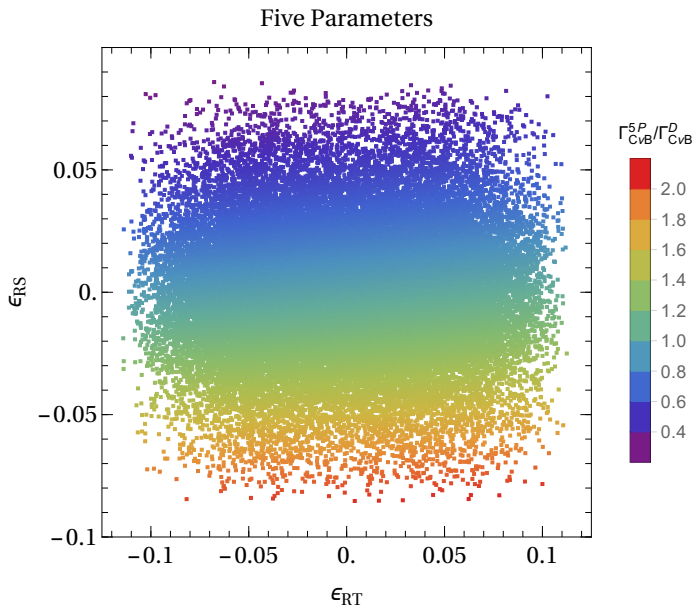

Figure 3.10: Ratio between the BSM capture rate with respect to the SM Dirac case for the five free couplings scenario in the plane (ϵ_{RS} versus ϵ_{RT}). The maximum (minimum) value of the ratio is 2.2 (0.3).

3.7.5 On the relic right-handed neutrino abundance

As we have seen in section 3.7.3, without BSM contributions the neutrino number density today is expected to be

$$\begin{aligned} n_{\nu_-^j} &= n_0, \quad n_{\nu_+^j} = n_0 \quad \text{(Majorana)}, \\ n_{\nu_-^j} &= n_0, \quad n_{\nu_+^j} = 0 \quad \text{(Dirac)}, \end{aligned} \tag{3.60}$$

with the capture rate in both cases given in eq. (3.51). There are three ways in which this result can be modified: (i) if neutrinos underwent a gravitational clustering process, (ii) if BSM interactions are present, and (iii) if an initial abundance of right-handed neutrinos was present in the early universe.

Neutrino motion in the Dark Matter gravitational potential has the effect of modifying the direction of the neutrino momentum without affecting its spin [58]. The immediate consequence is that neutrinos undergo a process of gravitational clustering that tends to

equilibrate the $h_j = +1$ and $h_j = -1$ populations. Since for Majorana neutrinos there is already equilibrium, eq. (3.60) is still valid. The situation is different for Dirac neutrinos, for which we get

$$n_{\nu_-^j} = n_0/2, \qquad n_{\nu_+^j} = n_0/2 \qquad \text{(Dirac, clustering)}. \tag{3.61}$$

Nevertheless, eq. (3.51) is still valid since the additional right-handed neutrino population in the Dirac case with clustering compensates for the loss in the left-handed neutrino population. Very recently, an N-body simulation has been considered in ref. [59] to estimate the relic neutrino density enhancement on Earth. The main result is that the clustering effect is negligible in the minimal Normal Ordering case while, for minimal Inverted Ordering, the capture rate can be increased up to 20% for both Dirac and Majorana neutrinos.

We now turn to the case in which BSM interactions are present. Since BSM physics modify the electroweak rates, this could potentially affect the left-handed neutrino abundance. As we have seen in section 3.7.4, we must have at most $\epsilon_{lq} \lesssim 10^{-1}$ to be compatible with β-decay and other low energy experimental bounds (with many parameters much smaller). As such, the active neutrinos were maintained in equilibrium with the plasma mainly by SM interactions, and we do not expect a significant change in the left-handed neutrino number density $n_{\nu_+^j}$.

Let us finally consider the case in which an initial abundance of right-handed neutrinos is present. Such abundance can be either thermal or non-thermal. A thermal population can be achieved by non-standard interactions or in the presence of a tiny neutrino magnetic moment [60; 61; 62]. Following [62], when the expansion of Universe becomes faster than the interaction rate, the right-handed neutrinos decouple as usual. At this freeze out temperature, T_R, the number densities of left- and right-handed neutrinos must be equal

$$n_{\nu_R^j}(T_R) = n_{\nu_L^j}(T_R). \tag{3.62}$$

Using entropy conservation, we can relate the right-handed neutrino abundance at late times

with the left-handed abundance, obtaining [62]

$$\frac{n_{\nu_R^j}(T_\nu)}{n_{\nu_R^j}(T_R)} = \frac{g_{*S}(T_\nu)}{g_{*S}(T_R)} \left(\frac{T_\nu}{T_R}\right)^3, \tag{3.63}$$

where $g_{*S}(T)$ is the number of relativistic degree of freedom in entropy at the temperature T. Choosing T_ν in eq. (3.63) to be the left-handed neutrino decoupling temperature, and using the definition of the effective number of thermal neutrino species $N_{\rm eff}$, one obtains [60; 61; 62]

$$n_{\nu_R^j}(T_\nu) = \left(\frac{1}{3}\Delta N_{\rm eff}\right)^{\frac{3}{4}} n_{\nu_L^j}(T_\nu), \tag{3.64}$$

where $\Delta N_{\rm eff} = N_{\rm eff}^{\rm exp} - 3.046$ and $N_{\rm eff} = 3.046$ is the SM value with 3 left-handed neutrinos. The experimental determination of $N_{\rm eff}$ by the Planck collaboration gives [63]

$$N_{\rm eff}^{\rm exp} = 3.14^{+0.44}_{-0.43} \qquad \text{He + Planck TT + low P + BAO} \qquad \text{at 95\% C.L.}$$

Combining eq. (3.64) with the experimental result, we get that the maximum density of right-handed neutrinos is [62]

$$n_{\nu_+^j} = n_{(\nu_-^j)^c} = n_0^R \simeq 16 \text{ cm}^{-3}. \tag{3.65}$$

The relic population of RH neutrinos modifies eq. (3.51) even for vanishing non-standard interactions. In the pure SM case, since the capture rate is proportional to $\mathcal{A}(h_j) = 1$ for both left- and right-handed neutrinos, we can have an increase in $\Gamma^{\rm D}_{\rm C\nu B}$ up to 28% [62]. The difference is even larger if BSM interactions are turned on, although it depends crucially on the case considered. For instance, in the vector-axial-vector scenario, the capture rate is increased by roughly 30%, while in the five parameter scenario the increase can be up to 70%. In this case, we have that the CνB rate can be as large as $2.8\,\Gamma^{\rm D}_{\rm C\nu B}$, reinforcing our results on the possibility of having Dirac neutrinos with a relic capture rate numerically similar to the Majorana one.

The last possibility consists in having an initial non-thermal right-handed neutrino abun-

dance. Following [64], we will suppose that right-handed Dirac neutrinos initially form a degenerated Fermi gas, decoupled from the thermal bath. In this case, the right-handed neutrino density is related to the photon density n_γ by

$$n_{\nu_R^j}(T_\gamma) = \frac{1}{6\zeta(3)} \frac{g_{*S}(T_\gamma)}{g_{*S}(T_R)} \vartheta \, n_\gamma, \tag{3.66}$$

where $\vartheta = \varepsilon_F / T_R$, ε_F the Fermi energy and T_R the freeze out temperature of the right-handed neutrinos. The experimental limit on ϑ obtained using Planck data is $\vartheta \lesssim 3.26$, from which we get that the maximum right-handed neutrino density is [64]

$$n_{\nu_+^j} = n_{(\nu_-^j)^c} \simeq 36 \text{ cm}^{-3}. \tag{3.67}$$

Since in this case we can have a larger right-handed neutrino population with respect to the thermal case, we expect larger modification in the capture rate. In the vector-axial-vector BSM case we find that the rate is increased between 40 and 90%, getting closer to the value expected for Majorana neutrinos in the SM. For the other three scenarios we found larger modifications. In the right-handed scalar-tensor case, the BSM capture rate has a maximum value of about $2.5\,\Gamma^{\text{D}}_{\text{C}\nu\text{B}}$, while in the five-parameter case we obtain $3.5\,\Gamma^{\text{D}}_{\text{C}\nu\text{B}}$. We conclude noticing that, in all the cases in which a right-handed neutrino population (either thermal or non-thermal) is present, the increase in the number of neutrinos lead to an increase in the capture rate.

The following Chapter is another scenario where the same ideas of the EFT for perturbative models are applied. As in this Chapter, we shall be mainly interested in dimension six operators and their effects at low energies, when the renormalization group flow is taking into account.

Chapter 4

Dark Sectors

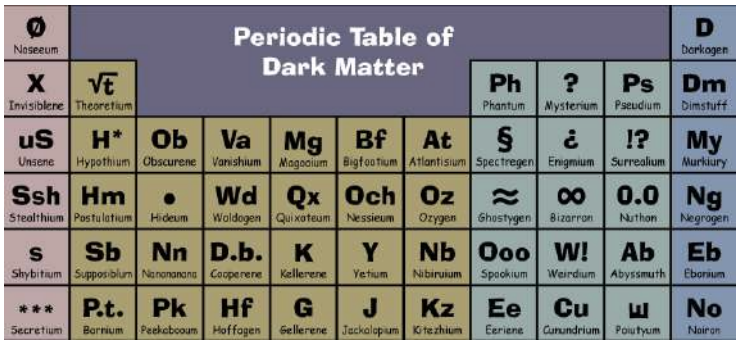

Credits to Ref. [65].

4.1 Dark Sectors

Over the last few years, dark sectors have started to play an increasingly important role in Beyond the Standard Model physics. The reason is twofold: on one hand, the null results from the LHC and other experiments are pushing 'traditional' BSM theories to more and more tuned regions of their parameter space, motivating the search for new unconventional signatures [66; 67; 68]. On the other hand, dark sectors are implicitly present in many Dark Matter (DM) models (especially in connection with light mediators, see for instance [69]), and are starting to appear in more recent solutions of the Hierarchy Problem like Twin Higgs [70], Folded SUSY [71] and the relaxation of the electroweak (EW) scale [72]. In addition, many dark sectors predict the existence of Long-Lived Particles (LLPs), for which a new extensive experimental program is being developed (see for instance [73]).

Of course, given the plethora of possible dark sectors with different symmetries and particles, a general analysis is impossible, and some broad assumption must be made. What we consider in this Chapter is a generic dark sector, communicating with the SM via some unspecified mediator X whose interactions are allowed to be flavor off-diagonal. If the mediator is somewhat heavier than the typical energy scale of low energy experiments (say a

few GeV), then the mediator can be integrated out, see Fig.4.1, generating effective contact interactions of the type

$$\mathcal{L}_{EFT} \supset c J_{\mathcal{D}} J_{SM} \,, \tag{4.1}$$

where $J_{\mathcal{D}}$ and J_{SM} are currents involving, respectively, dark and SM fields only, c is an appropriate coefficient ensuring the right dimensions, and we do not write possible Lorentz indices. This generic framework resembles typical Hidden Valley constructions [66; 74], and

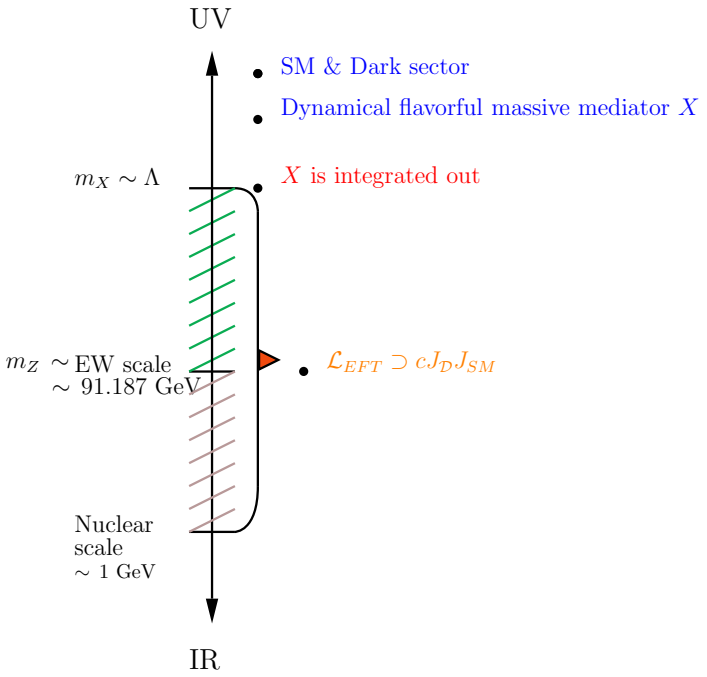

Figure 4.1: Evolution of our model from the UV to IR. We can see explicitly important cut-off scales.

can be obtained with a variety of mediators [68]. Also, the nature of the dark current depends crucially on the details of the dark sector, as it can be composed by elementary or composite fields. Since we will remain agnostic about the details of the dark sector, we dub the Effective Field Theory (EFT) defined in Eq. (4.1) by 'dark sector EFT'. Specific cases have already been analyzed in the literature, as we are going to see.

In order to compare the Wilson coefficients in Eq. (4.1) with experimental data, care

must be taken with the fact that renormalization group effects can (and generically will) be important. The running and mixing of operators written in the form of Eq. (4.1) has been studied in detail in the case in which J_{SM} is diagonal in flavor space and $J_{\mathcal{D}}$ is a Dark Matter current [75; 76; 77; 78; 79; 80; 81; 82; 83; 84; 85], and has been applied to the case of DM with mass in the MeV range in Ref. [86]. Some code has also been publicly released [87; 88], computing numerically the solution to the Renormalization Group Equations (RGE's). As a matter of fact, as long as we do not consider dark particles in the loops, the results of Refs. [80; 88] can be applied to any dark sector coupling to the SM via some flavor-blind heavy mediator, and not only to the case of Dark Matter currents.

The purpose of this chapter is to extend the analysis of the running and mixing of the dark sector EFT operators *supposing the mediator to be heavy and flavorful*. Such a mediator has already been considered in the framework of flavored Dark Matter (see for instance [89; 90; 91; 92; 93; 94; 95; 96; 97; 98; 99; 100; 101; 102]), but the running of the EFT has never been considered before. We keep our analysis as general as possible, without committing to a specific dark sector or requiring Dark Matter to be present. We restrict our analysis to the mixing of effective operators written as in Eq. (4.1). Of course, this is still not the complete renormalization of the dark sector EFT. Once the dimension of the operators to be included in the Lagrangian is fixed (*i.e.* the nature of the dark current is specified), we also need to include operators constructed out of SM fields only. In addition, loops of dark particles will contribute to the renormalization of the complete EFT, and the effect may be important. This has been recently studied in the context of Dirac Fermion DM EFT in Ref. [103], and in the case of flavorful mediators could, for instance, generate contributions to meson mixing operators. The information is of course fundamental for the comparison between data and theory but depends strongly on the nature of the particles running in the loops. As such, we decided to focus here only on the *model independent* information that can be extracted from the running and mixing of the dark sector EFT operators. We will study elsewhere the effects of dark particles in the loops.

The chapter is organized as follows: in Section 4.2 we build the dark sector Effective Field Theory, describing the operators considered above and below the EW scale. In Section 4.3

	q_L^i	u_R^i	d_R^i	l_L^i	e_R^i	H
$SU(3)_c$	**3**	**3**	**3**	**1**	**1**	**1**
$SU(2)_L$	**2**	**1**	**1**	**2**	**1**	**2**
$U(1)_Y$	+1/6	+2/3	-1/3	-1/2	-1	+1/2

Table 4.1: Charges and gauge representations of the SM fields above the EW scale. The index i is a family index.

we discuss the RGE's and show the matching needed in evolving the Wilson coefficients from high to low energy. Finally, Section 4.4.1 is devoted to the numerical results and to possible phenomenological applications.

4.2 Dark Sector Effective Field Theory

We start in this Section with the definition of our framework. The effective Lagrangian contains the SM Lagrangian, the kinetic term for the dark fields and the interactions between the dark sector and the SM particles. As explained in the Introduction, we will work with interactions which are products of a dark and of a SM current,

$$\mathcal{L}_{int} \supset \frac{(C_a)_{ij}}{\Lambda^n} J_{\mathcal{D}}^a J_{SM}^{a,(ij)} + h.c. \tag{4.2}$$

The index a runs over all possible currents, while (i, j) are SM family indices. We do not write explicitly possible Lorentz indices. The dark currents can have a variety of forms, depending on the nature of the dark sector. For instance, they can be constructed out of fundamental fermions (like $J_{\mathcal{D}}^\mu = \overline{\chi}\gamma^\mu\chi$ or $J_{\mathcal{D}} = \overline{\chi}\chi$), out of fundamental scalars (like $J_{\mathcal{D}}^\mu = \phi^\dagger \overleftrightarrow{\partial}^\mu \phi$ or $J_{\mathcal{D}} = \phi^\dagger\phi$), or they can be constructed out of composite objects (pions or baryons) if the dark sector is strongly interacting at low energies [84; 104; 105]. Depending on the dimension of the currents, the appropriate n must be chosen. Since we do not want our conclusions to depend on the nature of the dark sector, in this work we will leave unspecified the nature of the dark current, making only the broad assumption that it is a complete gauge singlet. Our conventions for the SM fields are presented in Table 4.1 and in Appendix A.1.

Let us first consider the EFT *above* the Electroweak scale. In this case, we demand the

dimensions	currents	Wilson coefficient	flavor transformation
$d=2$	$H^\dagger H$	$C_{H\ portal}$	singlet
	$B_{\mu\nu}$	$C_{Y\ portal}$	singlet
	$\tilde{B}_{\mu\nu}$	$\tilde{C}_{Y\ portal}$	singlet
$d=5/2$	$\overline{\ell}_L \tilde{H}$	$C_{N\ portal}$	$\mathbf{3}$ of $SU(3)_{\ell_L}$
$d=3$	$\overline{q}_L \gamma^\mu q_L$	C_{q_L}	$(\mathbf{3},\overline{\mathbf{3}})$ of $SU(3)_{q_L} \times SU(3)_{q_L}$
	$\overline{u}_R \gamma^\mu u_R$	C_{u_R}	$(\mathbf{3},\overline{\mathbf{3}})$ of $SU(3)_{u_R} \times SU(3)_{u_R}$
	$\overline{d}_R \gamma^\mu d_R$	C_{d_R}	$(\mathbf{3},\overline{\mathbf{3}})$ of $SU(3)_{d_R} \times SU(3)_{d_R}$
	$\overline{\ell}_L \gamma^\mu \ell_L$	C_{ℓ_L}	$(\mathbf{3},\overline{\mathbf{3}})$ of $SU(3)_{\ell_L} \times SU(3)_{\ell_L}$
	$\overline{e}_R \gamma^\mu e_R$	C_{e_R}	$(\mathbf{3},\overline{\mathbf{3}})$ of $SU(3)_{e_R} \times SU(3)_{e_R}$
	$iH^\dagger \overleftrightarrow{D}_\mu H$	C_H	singlet
	$\partial_\nu B^{\nu\mu}$	C_B	singlet

Table 4.2: List of $d < 4$ currents constructed out of SM fields to be used in Eq. (4.2) only above the EW scale. We have suppressed all flavor indices. In our analysis we will focus on the running and mixing of $d = 3$ currents.

SM currents J^a_{SM} to be complete gauge singlets under $SU(3)_c \times SU(2)_L \times U(1)_Y$, with particle contents and charges given in Table 4.1. The assumption can of course be relaxed, see for instance Ref. [81]. The SM currents can be classified according to their dimensions, while the coefficients $(C_a)_{ij}$ in Eq. (4.2) can be classified based on their transformation properties under the SM flavor group $SU(3)_{q_L} \times SU(3)_{u_R} \times SU(3)_{d_R} \times SU(3)_{\ell_L} \times SU(3)_{e_R}$ (explicitly broken by the Yukawa couplings). This is shown in Table 4.2. At the level of $d = 2$ and $d = 5/2$ we have the scalar Higgs, hypercharge and neutrino portals, which are the only currents that allow for renormalizable portals between the SM and the dark sector. These currents have been extensively used in the context of sub-GeV Dark Matter (see for instance [106; 107; 108]) and, more recently, for the generation of neutrino masses [109]. From the point of view of running, none of these currents mix with the others. As long as the nature of the dark sector is not specified, the only relevant effects would be the thresholds corrections coming from wave function renormalization, that can be easily computed using Appendix C.3. Since in this research we will focus on the case of heavy mediators (*i.e.* on the case of non-renormalizable interactions between the SM and the dark sector), we will not consider these currents in the rest of the chapter. Moving on, non-trivial structures with both lepton and quark flavors appear at the level of $d = 3$, and these are the currents on which we will focus from now on.

dimensions	currents	Wilson coefficient	flavor transformation
$d = 3/2$	ν_L	$C_{\nu\ dark}$	$\mathbf{3}$ of $SU(3)_{\nu_L}$
$d = 2$	$F_{\mu\nu}$	$C_{A\ portal}$	singlet
	$\tilde{F}_{\mu\nu}$	$\tilde{C}_{A\ portal}$	singlet
$d = 3$	$\overline{u}\gamma^\mu u$	C_{V_u}	$(\mathbf{2}, \overline{\mathbf{2}})$ of $SU(3)_u \times SU(3)_u$
	$\overline{d}\gamma^\mu d$	C_{V_d}	$(\mathbf{3}, \overline{\mathbf{3}})$ of $SU(3)_d \times SU(3)_d$
	$\overline{e}\gamma^\mu e$	C_{V_e}	$(\mathbf{3}, \overline{\mathbf{3}})$ of $SU(3)_e \times SU(3)_e$
	$\overline{\nu_L}\gamma^\mu \nu_L$	$C_{V_{L\nu}}$	$(\mathbf{3}, \overline{\mathbf{3}})$ of $SU(3)_{\nu_L} \times SU(3)_{\nu_L}$
	$\overline{u}\gamma^\mu\gamma_5 u$	C_{A_u}	$(\mathbf{2}, \overline{\mathbf{2}})$ of $SU(3)_u \times SU(3)_u$
	$\overline{d}\gamma^\mu\gamma_5 d$	C_{A_d}	$(\mathbf{3}, \overline{\mathbf{3}})$ of $SU(3)_d \times SU(3)_d$
	$\overline{e}\gamma^\mu\gamma_5 e$	C_{A_e}	$(\mathbf{3}, \overline{\mathbf{3}})$ of $SU(3)_e \times SU(3)_e$
	$\partial_\nu F^{\nu\mu}$	C_γ	singlet

Table 4.3: List of $d < 4$ currents constructed out of SM fields to be used in Eq. (4.2) only below the EW scale. $F_{\mu\nu}$ denotes the photon field strength, while u, d and e are Dirac fermions. We have suppressed all flavor indices.

Of course, more currents with non-trivial flavor structure appear with $d \geq 4$, but since their effects are suppressed by higher powers of Λ, we will not consider them in the remainder of the chapter.

It is interesting to count the number of parameters in the dark sector EFT, focusing on the $d = 3$ currents. For the fermion bilinears, the Wilson coefficients shown in Table 4.2 are 3×3 matrices in flavor space. Moreover, it should be noted that the current $\partial_\nu B^{\nu\mu}$ is redundant, since it can be eliminated using the Equation of Motion (EoM) of the hypercharge field, see Eq. A.2. This leaves us with a total of 46 independent currents to be probed above the EW scale.

Moving to the EFT *below* the EW scale, we use Dirac fermions to construct currents that are gauge singlets under $SU(3)_c \times U(1)_{em}$. The possible currents up to dimension 3 are shown in Table 4.3. The flavor symmetry is now $SU(2)_u \times SU(3)_d \times SU(3)_e \times SU(3)_{\nu_L}$, explicitly broken by fermion masses, leaving a total of 53 independent currents to be probed below the EW scale. Notice that we do not introduce right-handed neutrinos in the low energy EFT, and we leave unspecified the mechanism behind neutrino masses. As we did above the EW scale, we will focus in the following on the running and mixing of the $d = 3$ currents, again

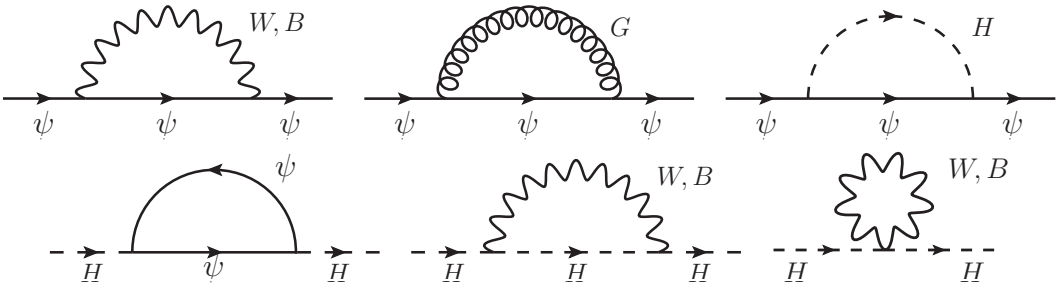

Figure 4.2: Feynman diagrams contributing to the wave function renormalization of fermions ψ and of the Higgs doublet H.

ignoring all possible renormalizable portals.

Our set up will be the following. We will assume the operators in Eq. (4.2) to be generated at some scale Λ, to be roughly identified with the mass of some flavorful mediator. We present in Appendix C.2 some specific examples using models present in the literature, see Eq. (C.6). If $\Lambda > \Lambda_{EW} \simeq m_Z$, we will use the $d = 3$ SM currents presented in Table 4.2, while if $\Lambda < \Lambda_{EW}$ we will use the $d = 3$ currents from Table 4.3. In both cases, we will leave the flavor structure of the Wilson coefficients $(C_a)_{ij}$ completely generic. In the next section we will compute the running and mixing of such currents from the scale Λ at which the operators are generated down to $E \ll \Lambda_{EW}$.

4.3 Renormalization group equations for the dark sector EFT

We start considering the EFT above the EW scale. To be explicit, the Lagrangian we consider is

$$\begin{aligned}\mathcal{L} = \frac{1}{\Lambda^n} J_{\mathcal{D}\mu} \Big[& \overline{q}_L \gamma^\mu C_{q_L} q_L + \overline{u}_R \gamma^\mu C_{u_R} u_R + \overline{d}_R \gamma^\mu C_{d_R} d_R \\ & + \overline{\ell}_L \gamma^\mu C_{\ell_L} \ell_L + \overline{e}_R \gamma^\mu C_{e_R} e_R + C_H i H^\dagger \overleftrightarrow{D}_\mu H \Big] ,\end{aligned} \tag{4.3}$$

where all the Wilson coefficients except C_H are matrices in flavor space. To be conservative, we suppose that the same dark current is coupled to all the SM terms, but it is easy to extend the analysis to more general cases. Notice that we do not include the current $\partial_\nu B^{\nu\mu}$ since it

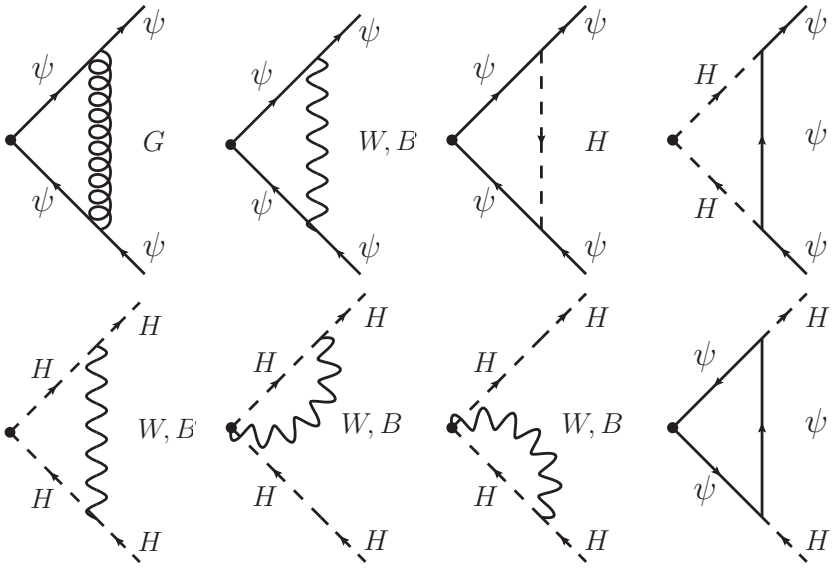

Figure 4.3: Feynman diagrams contributing to the current corrections for pure fermions ψ and Higgs currents.

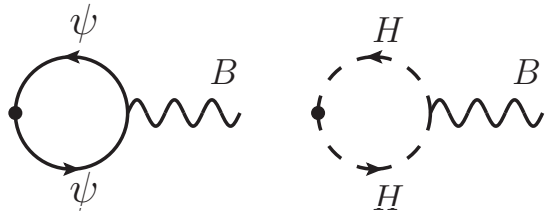

Figure 4.4: Feynman diagrams contributing to the redundant current $\partial_\nu B^{\nu\mu}$.

is redundant, see Eq. A.2.

Since the dark sector is a gauge singlet of the SM symmetry, only the SM fields and interactions are involved in the computation of the RGE's. Here we take into account the wave function renormalization of the fermion and Higgs fields (see Fig. 4.2), as well as the 'pure' current corrections shown in Fig. 4.3. The top diagrams in Fig. 4.3 are corrections to the fermion currents due to gauge and Yukawa interactions, while the bottom diagrams represent the loop contributions to the Higgs current. Divergencies induced by gauge interactions in the self-energy contributions and in the vertex corrections explicitly cancel one against the other in the final result, leaving only corrections proportional to the Yukawa matrices squared. However, additional care must be taken since, as shown in Fig 4.4, radiative corrections

generate the redundant current $\partial_\nu B^{\nu\mu}$. This contribution must be redefined away again using the equation of motion after the theory has been renormalized. For each Wilson coefficient, this produces an extra correction proportional to the hypercharge y_ψ. More details are presented in Appendix C.3. The complete computation gives

$$\begin{aligned}
(4\pi)^2\frac{dC_{q_L}}{d\log\mu} &= \frac{1}{2}\left[C_{q_L}Y_q^2 + Y_q^2 C_{q_L}\right] - \left[Y_u C_{u_R} Y_u^\dagger + Y_d C_{d_R} Y_d^\dagger - Y_q^2 C_H\right] + y_{q_L} T\mathbb{1}, \\
(4\pi)^2\frac{dC_{u_R}}{d\log\mu} &= \left[C_{u_R}Y_u^\dagger Y_u + Y_u^\dagger Y_u C_{u_R}\right] - 2\left[Y_u^\dagger C_{q_L} Y_u - Y_u^\dagger Y_u C_H\right] + y_{u_R} T\mathbb{1}\,, \\
(4\pi)^2\frac{dC_{d_R}}{d\log\mu} &= \left[C_{d_R}Y_d^\dagger Y_d + Y_d^\dagger Y_d C_{d_R}\right] - 2\left[Y_d^\dagger C_{q_L} Y_d - Y_d^\dagger Y_d C_H\right] + y_{d_R} T\mathbb{1}\,, \\
(4\pi)^2\frac{dC_{\ell_L}}{d\log\mu} &= \frac{1}{2}\left[C_{\ell_L}Y_e Y_e^\dagger + Y_e Y_e^\dagger C_{\ell_L}\right] - \left[Y_e C_{e_R} Y_e^\dagger - Y_e Y_e^\dagger C_H\right] + y_{\ell_L} T\mathbb{1}\,, \\
(4\pi)^2\frac{dC_{e_R}}{d\log\mu} &= \left[C_{e_R}Y_e^\dagger Y_e + Y_e^\dagger Y_e C_{e_R}\right] - 2\left[Y_e^\dagger C_{\ell_L} Y_e - Y_e^\dagger Y_e C_H\right] + y_{e_R} T\mathbb{1}\,, \\
(4\pi)^2\frac{dC_H}{d\log\mu} &= 2\Big(3\,\mathrm{tr}\left[C_{q_L}\hat{Y}_q^2\right] - 3\,\mathrm{tr}[Y_u C_{u_R} Y_u^\dagger] + 3\,\mathrm{tr}[Y_d C_{d_R} Y_d^\dagger] \\
&\qquad - \mathrm{tr}[Y_e^\dagger C_{\ell_L} Y_e] + \mathrm{tr}[Y_e C_{e_R} Y_e^\dagger]\Big) + 2\,\mathrm{tr}\left[3\,Y_q^2 + Y_e^\dagger Y_e\right] C_H + y_H T\,,
\end{aligned} \tag{4.4}$$

where Y_ψ are non-diagonal Yukawa matrices, and we have defined the useful quantities

$$Y_q^2 \equiv Y_u Y_u^\dagger + Y_d Y_d^\dagger\,, \qquad \hat{Y}_q^2 \equiv Y_u Y_u^\dagger - Y_d Y_d^\dagger\,, \tag{4.5}$$

and

$$\begin{aligned}
T \equiv \frac{4}{3}g'^2\Big(&6y_{q_L}\mathrm{tr}[C_{q_L}] + 3y_{u_R}\mathrm{tr}[C_{u_R}] + 3y_{d_R}\mathrm{tr}[C_{d_R}] \\
&+ 2y_{\ell_L}\mathrm{tr}[C_{\ell_L}] + y_{e_R}\mathrm{tr}[C_{e_R}] + y_H C_H\Big)\,.
\end{aligned} \tag{4.6}$$

Notice that all the equations in Eq. (4.4) contain a term proportional to T generated in the redefinition of the redundant operator. This term is a function of all diagonal elements of the Wilson Coefficients and implies that a coupling between the dark current and a lepton (or quark) current is generated even if not present at the scale Λ. This fact has been used in the

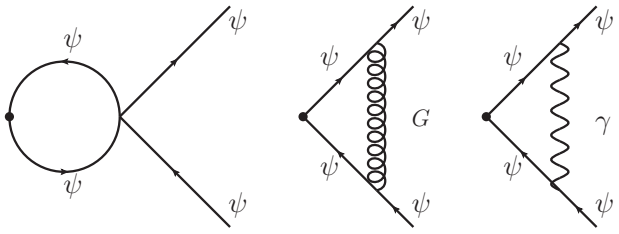

Figure 4.5: Feynman diagrams contributing to the current renormalization below the EW scale.

last years to put bounds coming from hadron or lepton collider on leptophilic and leptophobic Dark Matter models [78; 79; 80; 110]. We have explicitly checked that our results match with those of Ref. [79] once we restrict to flavor diagonal currents. Let us however remark that the contribution proportional to T is absent in flavor off-diagonal currents. In addition, we expect the largest flavor violating effects to appear on the RGE's involving the top-Yukawa coupling, *i.e.* those of the Wilson coefficients $C^{i3}_{q_L}$, $C^{3i}_{q_L}$, $C^{i3}_{u_R}$ or $C^{3i}_{u_R}$ $(i = 1, 2)$. In the numerical solution of the RGE's (see Section 4.4.1) we will consider the running of both the gauge and Yukawa couplings at 1-loop as taken from Refs. [111; 112].

Let us now turn to the RGE's *below* the EW scale, which we roughly identify with the Z boson mass. At this scale we integrate out the heavy fields W, Z, H and the *top* quark. The Lagrangian we consider is

$$\begin{aligned}\mathcal{L} = \frac{1}{\Lambda^n} J_{\mathcal{D}\mu} \Big[& \overline{u}\gamma^\mu C_{V_u} u + \overline{d}\gamma^\mu C_{V_d} d + \overline{e}\gamma^\mu C_{V_e} e + \overline{\nu}_L \gamma^\mu C_{V_{L\nu}} \nu_L \\ & + \overline{u}\gamma^\mu\gamma_5 C_{A_u} u + \overline{d}\gamma^\mu\gamma_5 C_{A_d} d + \overline{e}\gamma^\mu\gamma_5 C_{A_e} e \Big] ,\end{aligned} \tag{4.7}$$

where C_{V_u} and C_{A_u} are 2×2 matrices in the up-type quark flavor space, while all the other matrices are 3×3 in flavor space. Notice that we are not considering the current $\partial_\nu F^{\nu\mu}$ since it can be redefined away using the photon equations of motion. The procedure to obtain the RGE's is as before. The corrections due to the wave function renormalization are now due only to strong and electromagnetic interactions, and again they cancel against the vertex corrections in Fig. 4.5. What remains of the vertex corrections are the Fermi contributions, with flavor diagonal and off-diagonal contributions coming from neutral and charged current

interactions, respectively. Again, we need to take care of the redundant current $\partial_\nu F^{\nu\mu}$ which is generated radiatively by diagrams similar to those shown in Fig. 4.4 (with a photon in the external leg instead of a B vector), eliminating it via the EoM of the photon field. Again, more details are shown in Appendix C.3. The RGE's are given by

$$\begin{aligned}
(4\pi)^2\frac{dC_{V_u}}{d\log\mu} &= g_{V_u}\mathcal{F}_u + G_{Fud}V\big(\mathcal{M}^2_{V_d} - \mathcal{M}^2_{A_d}\big)V^\dagger + Q_u\mathcal{Q},\\
(4\pi)^2\frac{dC_{V_d}}{d\log\mu} &= g_{V_d}\mathcal{F}_d + G_{Fdu}V^\dagger\big(\mathcal{M}^2_{V_u} - \mathcal{M}^2_{A_u}\big)V + Q_d\mathcal{Q},\\
(4\pi)^2\frac{dC_{V_e}}{d\log\mu} &= g_{V_e}\mathcal{F}_e + Q_e\mathcal{Q},\\
(4\pi)^2\frac{dC_{V_{L\nu}}}{d\log\mu} &= g_{V_\nu}\mathcal{F}_\nu + G_{F\nu e}\left(\mathcal{M}^2_{V_e} - \mathcal{M}^2_{A_e}\right),\\
(4\pi)^2\frac{dC_{A_u}}{d\log\mu} &= g_{A_u}\mathcal{F}_u - G_{Fud}V\big(\mathcal{M}^2_{V_d} - \mathcal{M}^2_{A_d}\big)V^\dagger,\\
(4\pi)^2\frac{dC_{A_d}}{d\log\mu} &= g_{A_d}\mathcal{F}_d - G_{Fdu}V^\dagger\big(\mathcal{M}^2_{V_u} - \mathcal{M}^2_{A_u}\big)V,\\
(4\pi)^2\frac{dC_{A_e}}{d\log\mu} &= g_{A_e}\mathcal{F}_e,
\end{aligned} \tag{4.8}$$

where V is the CKM matrix, and we have used the definitions

$$\begin{aligned}
\mathcal{M}^2_{V_i} &= 2\sqrt{2}\left(C_{V_i}M_i^2 + M_i^2C_{V_i} - 2M_iC_{V_i}M_i\right),\\
\mathcal{M}^2_{A_i} &= 2\sqrt{2}\left(C_{A_i}M_i^2 + M_i^2C_{A_i} + 2M_iC_{A_i}M_i\right).
\end{aligned} \tag{4.9}$$

The matrix M_i is the diagonal mass matrix for the fermions of type i, and we have defined

$$\begin{aligned}
\mathcal{Q} &= \frac{8}{3}e^2\big[3Q_u\mathrm{tr}[C_{V_u}] + 3Q_d\mathrm{tr}[C_{V_d}] + Q_e\mathrm{tr}[C_{V_e}]\big]\mathbb{1},\\
\mathcal{F}_i &= 16\sqrt{2}\big[3g_{A_u}G_{Fiu}\mathrm{tr}[M_u^2C_{A_u}]\\
&\qquad + 3g_{A_d}G_{Fid}\mathrm{tr}[M_d^2C_{A_d}] + g_{A_e}G_{Fie}\mathrm{tr}[M_e^2C_{A_e}]\big]\mathbb{1}.
\end{aligned} \tag{4.10}$$

The coefficients $g_{V_i} = T_i^3 - 2s_w^2Q_i$ and $g_{A_i} = -T_i^3$ are the vector and axial couplings (T_i^3 is the third component of the isospin, Q_i is the electric charge and s_w is the sine of the weak angle), while the Fermi couplings $G_{Fff'}$ are defined in Eqs. (C.2) and (C.3). It should be

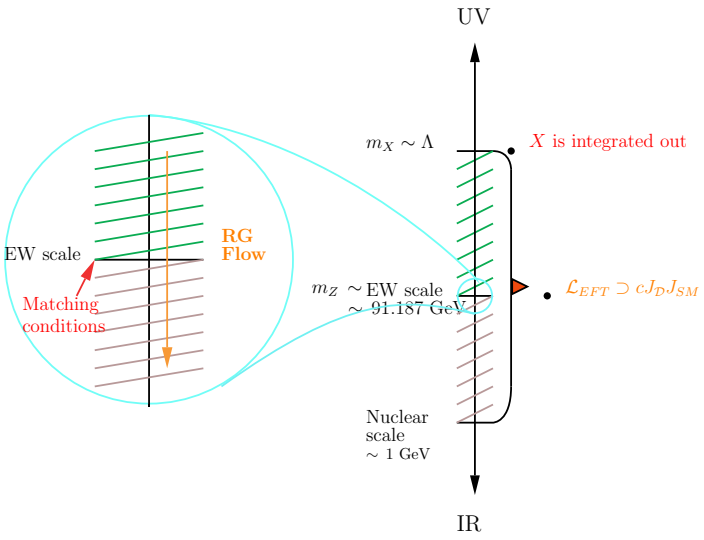

Figure 4.6: Matching conditions in our model at electroweak scale.

noted that, below the EW scale, not only the fermion masses run, but we need also to take into account the running of $G_{Fff'}$, and the running depends on the fermion type f and f' involved, justifying in this way the fact that we do not write a unique Fermi coupling. We use Ref. [113] for the running of the masses, and show in Appendix C.4 more details on the running of $G_{Fff'}$.

Before closing this Section, let us comment on how the two theories match onto each other. More specifically, when the scale Λ at which the dark sector EFT is generated is above the EW scale, the operators of Eq. (4.3) run and mix according to Eq. (4.4) down to $\Lambda_{EW} \simeq m_Z$. At this scale, the operators must be matched onto the Lagrangian of Eq. (4.7) before continuing with the running of Eq. (4.8) down to low energies. In Fig.4.6 we schematically show this situation. This procedure was presented in detail in Ref. [79] for flavor diagonal Wilson coefficients. In our case, the only new feature is that once we cross the EW threshold, all the fermions must be rotated into the mass basis. Explicitly, we write this transformation as

$$f_L \to L_f f_L\,, \qquad f_R \to R_f f_R\,, \tag{4.11}$$

where the matrices L_f and R_f diagonalize the Yukawa matrices. The matching then results

$$
\begin{aligned}
C_{V_u}(\Lambda_{EW}) &= \frac{1}{2}\Big(L_q^\dagger C_{q_L}(\Lambda_{EW}) L_q + R_u^\dagger C_{u_R}(\Lambda_{EW}) R_u \Big) + g_{V_u}\, C_H(\Lambda_{EW}) \mathbb{1}\,, \\
C_{V_d}(\Lambda_{EW}) &= \frac{1}{2}\Big(L_q^\dagger C_{q_L}(\Lambda_{EW}) L_q + R_d^\dagger C_{d_R}(\Lambda_{EW}) R_d \Big) + g_{V_d}\, C_H(\Lambda_{EW}) \mathbb{1}\,, \\
C_{V_{L\nu}}(\Lambda_{EW}) &= \frac{1}{2} L_\ell^\dagger C_{\ell_L}(\Lambda_{EW}) L_\ell + g_{V_\nu}\, C_H(\Lambda_{EW}) \mathbb{1}\,, \\
C_{V_e}(\Lambda_{EW}) &= \frac{1}{2}\Big(L_\ell^\dagger C_{\ell_L}(\Lambda_{EW}) L_\ell + R_e^\dagger C_{e_R}(\Lambda_{EW}) R_e \Big) + g_{V_e}\, C_H(\Lambda_{EW}) \mathbb{1}\,, \\
C_{A_u}(\Lambda_{EW}) &= \frac{1}{2}\Big(- L_q^\dagger C_{q_L}(\Lambda_{EW}) L_q + R_u^\dagger C_{u_R}(\Lambda_{EW}) R_u \Big) + g_{A_u}\, C_H(\Lambda_{EW}) \mathbb{1}\,, \\
C_{A_d}(\Lambda_{EW}) &= \frac{1}{2}\Big(- L_q^\dagger C_{q_L}(\Lambda_{EW}) L_q + R_d^\dagger C_{d_R}(\Lambda_{EW}) R_d \Big) + g_{A_d}\, C_H(\Lambda_{EW}) \mathbb{1}\,, \\
C_{A_e}(\Lambda_{EW}) &= \frac{1}{2}\Big(- L_\ell^\dagger C_{\ell_L}(\Lambda_{EW}) L_\ell + R_e^\dagger C_{e_R}(\Lambda_{EW}) R_e \Big) + g_{A_e}\, C_H(\Lambda_{EW}) \mathbb{1}\,.
\end{aligned}
\tag{4.12}
$$

Notice in particular that the term induced by C_H affects only the diagonal Wilson coefficients. In the following Section we will solve numerically the RGE's and show the numerical impact of turning on off-diagonal currents at the scale Λ.

4.4 Operators from flavored dark sectors running to low energy

4.4.1 Numerical results and possible applications

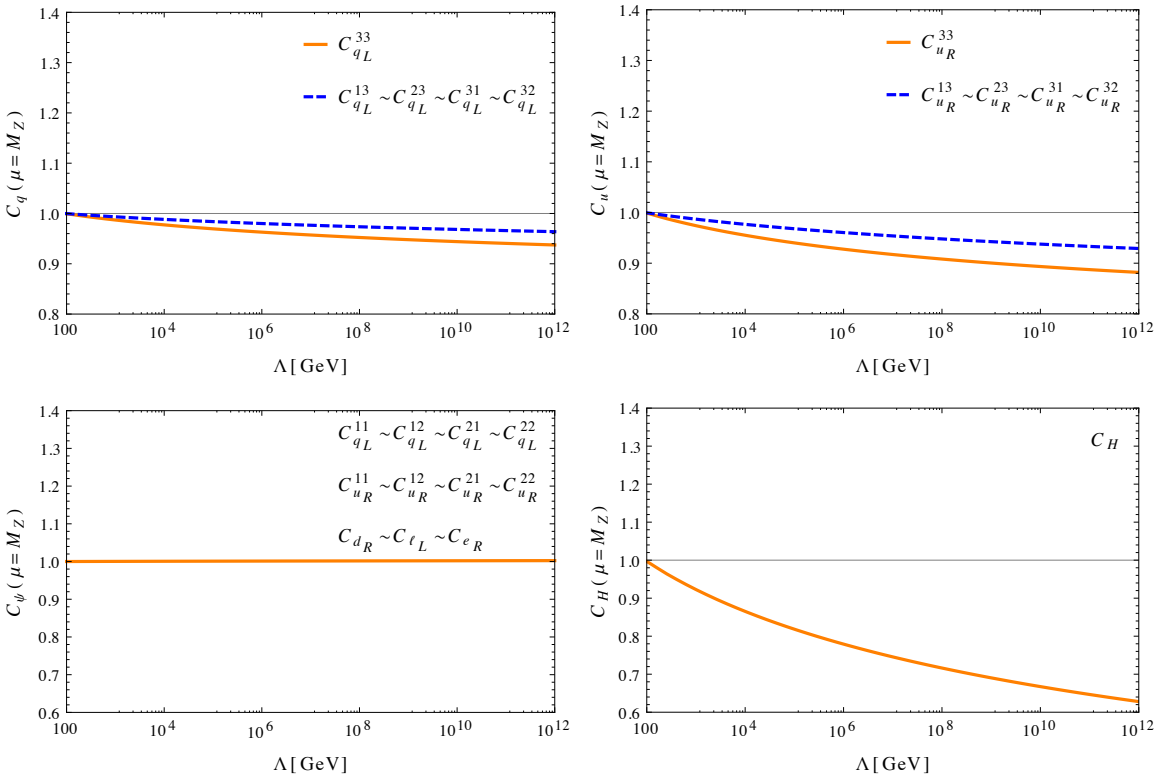

Figure 4.7: Running of the Wilson Coefficients above the EW scale, taking as initial condition $(C_a)_{ij}(\Lambda) = 1$ for all the values of a, i and j. In the bottom left panel, $C_{d_R} \sim C_{\ell_L} \sim C_{e_R}$ applies to all the matrix elements, with no difference for those involving the third generation.

We turn in this section to the numerical solution of the RGE's presented in Eqs. (4.4) and (4.8). As already mentioned, in solving Eqs. (4.4) and (4.8) we not only take into account the EW threshold if needed, but we also consider the running of the gauge and Yukawa couplings (for the theory above the EW scale) and the running of the Fermi coupling and fermion masses (for the theory below the EW scale). We show in Fig. 4.7 the value of the Wilson coefficients at the EW scale as a function of Λ, considering the "flavor-democratic"

initial condition

$$(C_a)_{ij}(\Lambda) = 1\,, \qquad \text{for all } a, i \text{ and } j\,. \tag{4.13}$$

As expected, the effect of the running is more important for the currents constructed out of top-quarks (with Wilson coefficients $C^{3i}_{q_L}$, $C^{i3}_{q_L}$, $C^{3i}_{u_R}$ and $C^{i3}_{u_R}$, with $i = 1, 2, 3$) and for C_H, in which the top Yukawa coupling enters. The result can be easily understood inspecting Eq. (4.4). In the limit in which only the top-Yukawa coupling is turned on, we have

$$\begin{aligned}
&\frac{dC^{i3}_{q_L}}{d\log\mu} \simeq \frac{y_t^2}{32\pi^2} C^{i3}_{q_L}\,, \quad \frac{dC^{3i}_{q_L}}{d\log\mu} \simeq \frac{y_t^2}{32\pi^2} C^{3i}_{q_L}\,, \quad \frac{dC^{33}_{q_L}}{d\log\mu} \simeq \frac{y_t^2}{16\pi^2}\left(C_H + C^{33}_{q_L} - C^{33}_{u_R}\right)\,, \\
&\frac{dC^{i3}_{u_R}}{d\log\mu} \simeq \frac{y_t^2}{16\pi^2} C^{i3}_{u_R}\,, \quad \frac{dC^{3i}_{u_R}}{d\log\mu} \simeq \frac{y_t^2}{16\pi^2} C^{3i}_{u_R}\,, \quad \frac{dC^{33}_{u_R}}{d\log\mu} \simeq \frac{y_t^2}{8\pi^2}\left(C_H - C^{33}_{q_L} + C^{33}_{u_R}\right)\,,
\end{aligned} \tag{4.14}$$

with $i = 1, 2$ and all the other RGE's vanishing. The solutions at the scale m_t at which we integrate out the top quark are easily found. For the off-diagonal Wilson coefficients they are

$$\begin{aligned}
C^{i3}_{q_L}(m_t) &\simeq \left(\frac{m_t}{\Lambda}\right)^{y_t^2/32\pi^2} C^{i3}_{q_L}(\Lambda)\,, \quad C^{3i}_{q_L}(m_t) \simeq \left(\frac{m_t}{\Lambda}\right)^{y_t^2/32\pi^2} C^{3i}_{q_L}(\Lambda)\,, \\
C^{i3}_{u_R}(m_t) &\simeq \left(\frac{m_t}{\Lambda}\right)^{y_t^2/16\pi^2} C^{i3}_{u_R}(\Lambda)\,, \quad C^{3i}_{u_R}(m_t) \simeq \left(\frac{m_t}{\Lambda}\right)^{y_t^2/16\pi^2} C^{3i}_{u_R}(\Lambda)\,,
\end{aligned} \tag{4.15}$$

where again $i = 1, 2$, while for the diagonal Wilson coefficients they are

$$\begin{aligned}
C^{33}_{q_L}(m_t) &\simeq C^{33}_{q_L}(\Lambda) + \frac{y_t^2}{16\pi^2}\left[C_H(\Lambda) + C^{33}_{q_L}(\Lambda) - C^{33}_{u_R}(\Lambda)\right]\log\frac{m_t}{\Lambda}\,, \\
C^{33}_{u_R}(m_t) &\simeq C^{33}_{u_R}(\Lambda) + \frac{y_t^2}{8\pi^2}\left[C_H(\Lambda) - C^{33}_{q_L}(\Lambda) + C^{33}_{u_R}(\Lambda)\right]\log\frac{m_t}{\Lambda}\,.
\end{aligned} \tag{4.16}$$

From these equations we get various important informations: (i) the off-diagonal Wilson coefficients can have a substantial running due to y_t, (ii) the renormalization of the flavor-off-diagonal Wilson coefficients is always multiplicative, in the sense that there are no important flavor changing generated during the running to low energy, and (iii) while the running of the flavor-off-diagonal Wilson coefficients is irreducible, the running of the flavor-diagonal coefficients depends strongly on the correlations between the initial conditions of different Wilson coefficients. For instance, we see from Eq. (4.16) that had we considered "flavor-

democratic" initial conditions without generating the Higgs current ($C_H(\Lambda) = 0$), then the diagonal Wilson coefficients would basically not run. This is not true for the off-diagonal coefficients, that once turned on will run independently from the initial conditions of other coefficients. We stress that the analytical expressions of Eqs. (4.15) and (4.16) reproduce accurately the full numerical results.

Moving to the EFT below the EW scale, inspection of Eq. (4.8) shows that the RGE's depend on the Fermi coupling $G_{Fff'}$ and on the electric charge e^2. Both contributions are rather small, and from the practical point of view, all the Wilson coefficients remain basically constant in this energy range. We have confirmed numerically that this is indeed the case. We conclude then that the relevant running happens above m_t, in the energy region in which the top-quark is still a dynamical degree of freedom. For mediators with mass above the EW scale coupling to the top quark, the effect of the running may be important and must thus be taken into account in the comparison with experiments. On the contrary, if the mediator is lighter than the EW scale, or if it does not interact with the top quark, the tree level predictions are usually a good approximation for the extractions of phenomenological bounds.

We conclude this Section with some phenomenological remark. Using Eq. (4.15) we see that the main effect of the running will manifest at low energy in observables related to the B mesons, *i.e.* involving the $\bar{b}\gamma^\mu(\gamma_5)d$ and $\bar{b}\gamma^\mu(\gamma_5)s$ currents. More precisely, the vector and axial coefficients at a scale $\mu \ll m_Z$ are given by

$$\begin{aligned} C^{3i}_{V_d}(\mu) &\simeq \frac{1}{2}\left[\left(\frac{m_t}{\Lambda}\right)^{y_t^2/32\pi^2} C^{i3}_{q_L}(\Lambda) + C^{3i}_{d_R}(\Lambda)\right] , \\ C^{3i}_{A_d}(\mu) &\simeq \frac{1}{2}\left[-\left(\frac{m_t}{\Lambda}\right)^{y_t^2/32\pi^2} C^{i3}_{q_L}(\Lambda) + C^{3i}_{d_R}(\Lambda)\right] , \end{aligned} \tag{4.17}$$

the same result is also valid by changing the order $3 \leftrightarrow i$, with $i = 1, 2$. This is important when the dark sector is light, in such a way that the decays $b \to s +$ invisible and $b \to d +$ invisible are kinematically allowed. These processes were studied in the context of dark sector phenomenology in Ref. [114]. As shown in this Reference, the bounds on the Wilson coefficients depend crucially on the nature of the dark particles appearing in the dark current.

Given this model dependence, we will not explore this matter here. In addition, we remark that more flavor effects would be obtained once dark particles loops are considered, for instance generating contributions to the B mesons mass mixing. As shown in Ref. [103] in the context of flavor diagonal DM EFT, these effects can be important, but since they are model dependent, we defer their study to a future work.

Until now we deal with EFT techniques for perturbative models as described in Section 2.3 of Chapter 2. However, in the following chapter we shall apply the ideas developed in Section 2.4 of the same chapter, this is the framework to tackle non-perturbative models.

Chapter 5

Relaxion Physics & GW

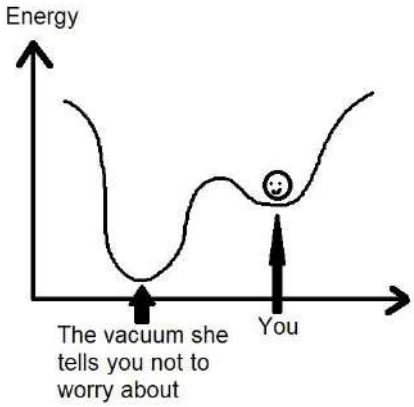

Credits Anonymous.

5.1 Introduction

The 2010s decade has been marked by two scientific milestones: the Higgs discovery at the Large Hadron Collider (LHC) in 2012 by the ATLAS and CMS collaborations [115; 116] and the first direct detection of gravitational waves (GW) on Earth in 2015 by the LIGO and VIRGO collaborations [117; 118]. While the latter has given access to previously unaccessible phenomena, like the merging of black holes binary systems, the first discovery has exacerbated the hierarchy problem, *i.e.* the question of how the electroweak (EW) scale can be so much smaller than the Standard Model (SM) cutoff without the need for a large degree of fine tuning. Traditional symmetry based solutions like supersymmetry and composite dynamics are nowadays pushed in quite tuned regions of parameter space by the null LHC searches.

This has motivated the scientific community to consider alternative solutions to the problem of the instability of the EW scale. A compelling possibility is the one where the Higgs mass is driven to a value much smaller than the SM cutoff by a dynamical evolution in the early Universe. This mechanism has been firstly proposed in [72] and goes under the name of *cosmological relaxation*. The basic idea is as follows: the Higgs squared mass parameter $H^\dagger H$ is made dynamical by its coupling with a new scalar degrees of freedom, the relaxion

ϕ, generally assumed to be a pseudo Nambu Goldstone boson (pNGB). The evolution of the relaxion field during the early Universe evolution, governed by an opportune potential $V(\phi)$, scans the Higgs mass parameter, makes it evolving from large positive values up to the critical value in which electroweak symmetry breaking (EWSB) is triggered. Once the Higgs develops a vacuum expectation value (VEV), a back-reaction potential turns on and stops the relaxion evolution, dynamically selecting the measured value for the EW scale.

For the mechanism to work, two ingredients are essentials: *i*) a friction mechanism that slows down the relaxion evolution and avoids the overshooting of the back-reaction barrier and consequently of the correct EW scale, and *ii*) a mechanism to generate the back-reaction itself. In much of the explicit realizations of the relaxion mechanisms, the friction is provided by the Hubble expansion during inflation [72; 119; 120; 121; 122; 123; 124; 125; 126; 127; 128; 129; 130; 131; 132; 133; 134; 135; 136; 137] [1], so that the relaxion fields slow rolls during the cosmological relaxation phase. Alternatives are however possible: the friction can be generated by particle production [139; 142; 143; 144; 145], the relaxion can fast-roll during inflation [146] or it can fragment [147; 148]. Cosmological relaxation after inflation is also possible [149]. As for the back-reaction, we can essentially distinguish between familon models [123] and models in which the potential barrier is generated by the confinement of a new strongly interacting dynamics with new vector fermions, as already discussed in the original paper [72].

In the present Chapter we focus on this second scenario. This opens up an interesting possibility: after a relaxation phase during inflation in which the EW scale is dynamically selected, the Universe may be reheated to temperatures above the critical temperature of the new confining interactions. If this happens, the back-reaction barrier disappears and the Universe undergoes a second relaxation phase. When the temperature of the Universe drops again below the confinement scale of the new strong dynamics, the barrier is once again generated and the relaxion stops again its evolution. Crucially, depending on the gauge group of the new confining dynamics, the number of new fermions and their representations under

[1] Notice that usually the details of the inflation sector are left largely unspecified. See however [138; 139] for attempts to take into account inflaton effects, or [140; 141] for an example of how to identify the relaxion with the inflaton.

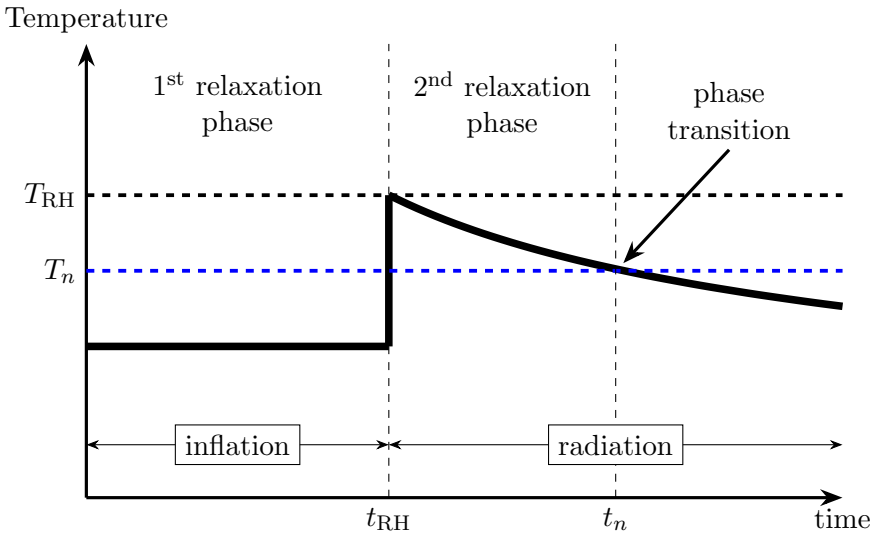

Figure 5.1: Sketch of the framework we are considering. The thick black line represents an approximate sketch of the temperature evolution. During inflation a first relaxation phase selects the correct EW vacuum. When reheating happens at $t_{\rm RH}$, the temperature increases and the radiation domination phase begins. For simplicity we will consider reheating to be an instantaneous process. If the reheating temperature $T_{\rm RH}$ is larger than the nucleation temperature T_n, the back-reaction potential disappears and a second relaxation phase occurs. After a while, the temperature falls below the nucleation temperature of the new strongly interacting group, and a phase transition occurs which may generate a GW signal.

the gauge group, this phase transition can be of first order [150] and can thus give rise to a stochastic GW background [151]. The signal might be then detected at present and future interferometer experiments [152; 153; 154; 155; 156; 157; 158; 159; 160], thus connecting in this way the two milestones discovery of the 2010s. A sketch of the situation we are considering is shown in Fig. 5.1.

The Chapter is organized as follows: in Section 5.2 we briefly review the hierarchy problem. Later in Section 5.3 we introduce introduced the relaxion mechanism. Sections 5.4 and 5.5 are devoted to an introduction to phase transitions and gravitational waves. In Section 5.6 we review the cosmological relaxation mechanism, where the back-reaction potential is generated by a new strongly interacting dynamics. In Section 5.7 we analyze the relaxion evolution after reheating. We show how the equation of motion of the relaxion during this second relaxation phase can be analytically solved for certain range of temperatures, and

what are the bounds on the parameter space that we obtain by requiring the additional relaxation phase not to spoil the dynamical selection of the EW scale achieved during the first relaxation phase. In Section 5.8 we discuss the GW spectrum generated in the first order phase transition associated with the generation of the back-reaction potential after reheating and its detectability at future experiments. We also add two Appendices where we collect more technical material. In Appendix E.1 we discuss in detail various models of strongly interacting vector-like fermions and review how to describe their low energy dynamics and in particular their vacuum energy, which is relevant for the relaxion mechanism. In Appendix F.1 we instead explicitly show how the constraints on the relaxion parameter space used throughout the paper are derived.

5.2 The Hierarchy Problem

The discovery in 2012 of a new resonance, with mass around 125 GeV, has been a milestone for Particle Physics [115; 161]. In Fig.5.2 we observe the invariant mass distribution data together with the fit to $H \to ZZ^* \to 4\,l$ (left) and to $H \to \gamma\gamma$ (right). The red line represents the fit to the data points, including the shape of the Higgs Boson and the backgrounds. These backgrounds come from the quark-antiquark annihilation $qq \to ZZ^*$ (left) and diphoton $\gamma\gamma$ final states (right).

The hierarchy problem drove most of the theoretical activities over the last forty years. It can be summarized as follows: any running scalar mass in the theory receives threshold corrections proportional to the squared mass of any particle interacting with the scalar. In particular, very large threshold corrections are expected to appear at least at the Planck mass, where gravity should become important. The problem stems from the fact that small variations in the masses appearing in the thresholds produce huge variations of the scalar mass at low energies, and must thus be tuned to keep the variations under control. As a consequence, the properties of any new physics model that extends the SM at high energies must be known with a high degree of precision to reliably compute the low energy physics, clearly undermining our concept of Effective Field Theory, see Chapter 2. This is true in

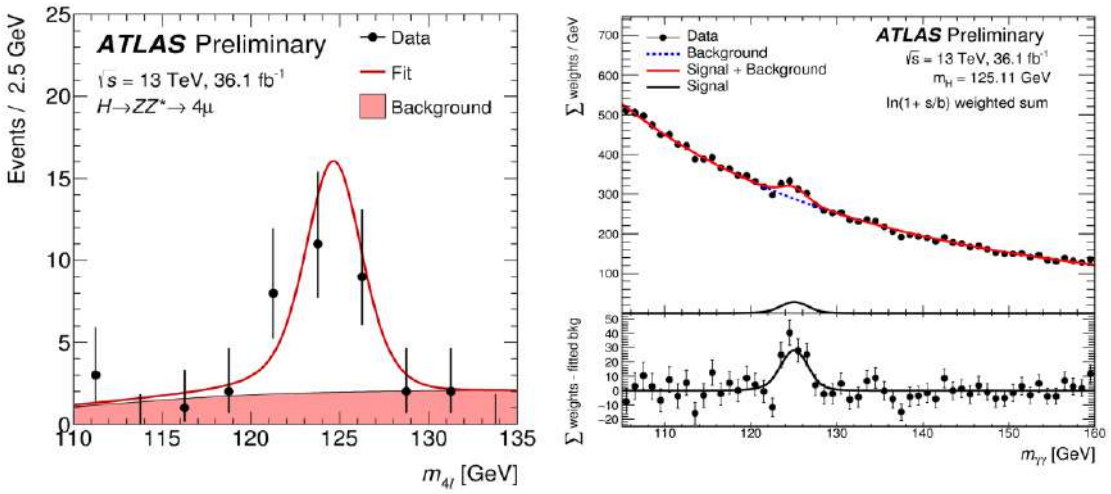

Figure 5.2: The invariant mass distribution data together with the fit (solid red lines) to $H \to ZZ^* \to 4l$ (left) and to $H \to \gamma\gamma$ (right). The backgrounds come from the quark-antiquark annihilation $qq \to ZZ^*$ (left) and diphoton $\gamma\gamma$ final states (right)[162].

particular for the Higgs Boson mass parameter m_H. For instance, consider the existence of a new particle at the scale of 10^{10} GeV (scale of New Physics M_{NP}). The contribution to the running of the Higgs mass is given by

$$M\frac{\partial m_H^2}{\partial M} = \frac{\alpha}{16\pi^2}M_H^2, \tag{5.1}$$

where $M_H = 10^{10}$ GeV is the mass of some new particle which interacts with the Higgs and α is some combination of couplings. In this example, the running of the Higgs squared mass with respect to the scale M in the SM presents a jump at 10^{10} GeV, see Fig.5.3. We could also estimate the order of the tuning as $(m_H/M_{NP})^2 \sim 10^{-16}$ [163]. Considering this problematic sensibility of the Higgs boson to NP, many interesting solutions were addressed in the last decades, even before the Higgs were discovered: Supersymmetry [164], extra-dimensions [165], composite Higgs [166], etc.

In general, the new degrees of freedom in BSM theories contribute to the Higgs mass either at tree or at loop level. From the Wilsonian's EFT point of view, if the scale at which the new degrees of freedom appear is Λ, the quadratic Higgs term (the only term in the SM

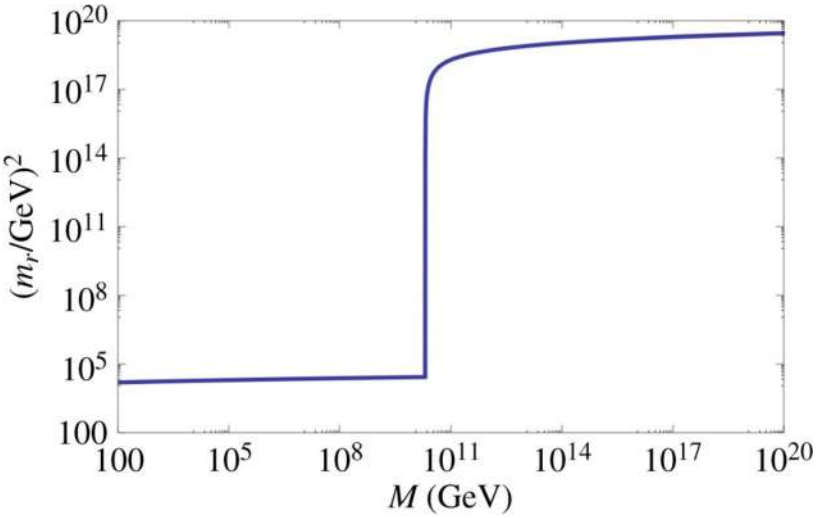

Figure 5.3: Running of the renormalized Higgs squared mass with respect to the scale M, the plot presents a jump at $10^{10}GeV$ due to the insertion of a new particle of mass $M_H = 10^{10}GeV$. As a consequence the Higgs mass requires a tunning of the order $(m_H/M_{NP})^2 \sim 10^{-16}$ [163].

with a dimensionful coefficient) would be $\mathcal{L} \supset -\Lambda^2 H^\dagger H$.

In Ref.[72], P. Graham, D. Kaplan and S. Rajendran proposed an alternative solution to the hierarchy problem. In contrast to the conventional models, their framework, called Cosmological Relaxation, generates the stability of the Higgs vacuum dynamically. This is achieved trough the interaction between the Higgs and a new scalar field, the *relaxion*. The following section is devoted to introduce the Relaxion mechanism *a la* Graham-Kaplan-Rajendran.

5.3 Higgs-Relaxion mechanism

In 2015, P. Graham, D. Kaplan and S. Rajendran in Ref. [72] proposed a new mechanism to solve the hierarchy problem. The generic form of the relaxion lagrangian is given by

$$\mathcal{L} \supset -(\Lambda^2 - \epsilon\,\Lambda\,\phi)H^\dagger H - \lambda\,(H^\dagger\,H)^2 - V(\epsilon\,\phi) - \frac{1}{32\pi^2}\frac{\phi}{F}G^{\mu\nu}\widetilde{G}_{\mu\nu} + \mathcal{L}_{\text{fermions}} + \mathcal{L}_{\text{gauge}}, \quad (5.2)$$

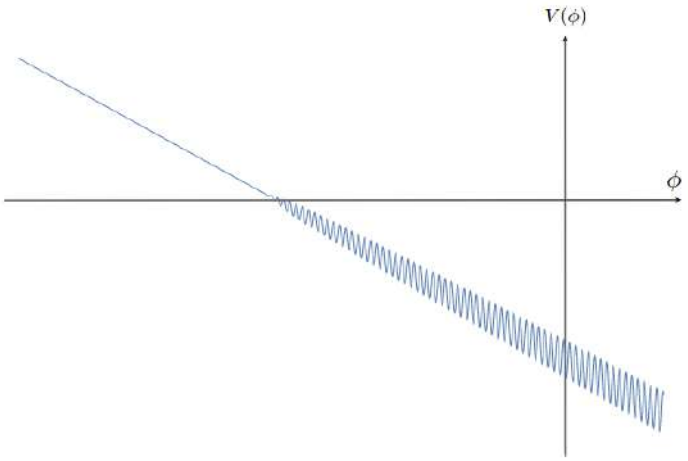

Figure 5.4: Relaxion Potential used in Ref. [72].

where H is the Higgs doublet, $G^{\mu\,\nu}$ is the field strength tensor of a non-Abelian gauge theory and $\widetilde{G}_{\mu\nu}$ its dual, Λ is the cutoff of the theory, λ, ϵ and r are positive dimensionless parameters and ϕ is the relaxion field. The fermion content inside $\mathcal{L}_{\text{fermions}}$ could have a QCD origin or not, and it plays an important role for the relaxion mechanism to work. After chiral symmetry breaking (ChSB) takes place, the topological term in Eq. (5.2) in conspiracy with the fermion sector develops a back-reaction potential. After that the form of the Higgs-Relaxion potential at tree-level [72] is

$$V(H,\phi) = \left(\Lambda^2 - \epsilon\Lambda\phi\right) H^\dagger H + \lambda (H^\dagger H)^2 - r\epsilon\Lambda^3\phi + V_{\text{BR}}(H,\phi)\ , \tag{5.3}$$

where the back-reaction potential takes the form

$$V_{\text{BR}}(H,\phi) = \Lambda^4_{\text{BR}}(\langle H\rangle)\cos\left(\frac{\phi}{F}\right)\ . \tag{5.4}$$

In this equation $\langle H\rangle = v/\sqrt{2}$. It is worthwhile to stress the explicit dependence in the amplitude of Eq.(5.4) on the Higgs VEV. The amplitude is a (model dependent) monotonically increasing function of the Higgs VEV and F is the scale at which the NGB ϕ appears.

We show in Fig.(5.4) a plot of a typical relaxion potential. The potential in Eq.(5.2) that depends on the relaxion field, $V(\epsilon\,\phi)$, has been expanded as $-r\epsilon\Lambda^3\phi - r\epsilon^2\Lambda^2\phi^2 + \ldots$. Because

at the EWSB scale the first and second contribution in the latter expansion are of the same order, we consider just the linear term as in Eq.(5.3). We see that if $\epsilon \to 0$, the lagrangian Eq.(5.3) respects a discrete shift symmetry $\phi \to \phi + 2\pi F$. This symmetry is explicitly broken by the spurion ϵ, which can thus be taken small in a technically natural way.

We assume that the cosmological relaxation mechanism takes place during inflation, with ϕ evolving in a slow-roll regime. We furthermore take the initial value of the field ϕ to be sufficiently small to guarantee the condition $\Lambda^2 - \epsilon\Lambda\phi_{in} > 0$ to be satisfied at the beginning of the relaxation phase, thus implying an unbroken EW symmetry. As ϕ evolves, increasing its value due to the $-r\epsilon\Lambda^3\phi$ term in the potential, the Higgs squared mass parameter becomes smaller and smaller, until it crosses zero and causes the breaking of the EW symmetry. Once $\langle H \rangle \neq 0$, the back-reaction potential $V_{\rm BR}$ is switched on, this implies:

$$\Lambda_{\rm BR}(\langle H \rangle) = \begin{cases} 0 & \text{if } \langle H \rangle = 0, \\ \neq 0 & \text{if } \langle H \rangle \neq 0. \end{cases} \tag{5.5}$$

The amplitude of the oscillating term grows with the Higgs VEV, until it is large enough to stop the evolution of ϕ, dynamically selecting the right value of $\langle H \rangle$. This is the essence of the relaxion mechanism (see Fig 5.5).

In addition there are some conditions that are needed to guarantee the successful realization of the relaxion mechanism, see Appendix F.1 for more details.

Validity of the EFT: We are assuming the field ϕ to be an angular degree of freedom, with a decoupled radial mode. Since the mass of the radial mode is $\mathcal{O}(F)$ we obtain the condition $F \gtrsim \Lambda$. We will also require $F \lesssim M_{\rm Pl}$, where $M_{\rm Pl} \simeq 10^{18}$ GeV is the Planck mass.

Conditions on inflation: We ask the dynamics of inflation to be decoupled from the one of the relaxion. Otherwise, we open the possibility that the relaxion could spoil inflation. Hence, to achieve this we require the relaxion energy density $\rho_\phi \sim \Lambda^4$ to be smaller than the inflaton energy density, $\rho_{\rm infl} \sim H_I^2 M_{\rm Pl}^2$, where H_I is the Hubble scale during

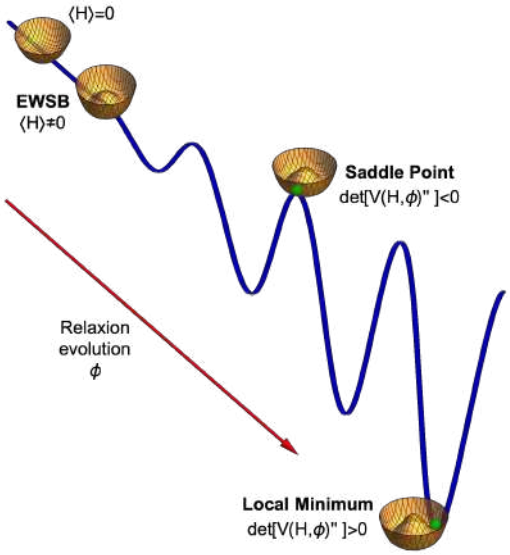

Figure 5.5: Sketch of the electroweak relaxation mechanism. At the beginning of the relaxion evolution the Higgs squared mass parameter is positive and $\langle H \rangle = 0$. As ϕ evolves it drives $\langle H \rangle \neq 0$. Once the Higgs VEV is turned on, a back-reaction is generated, stopping the evolution. We also show the sign of the determinant of the matrix of second derivatives of the potential, important in deriving Eq. (F.8).

inflation. This implies the lower bound

$$H_I \gtrsim \frac{\Lambda^2}{M_{\rm Pl}} \ . \tag{5.6}$$

Since we are assuming that the back-reaction is generated by some strong force, we need to guarantee that the barriers can form during inflation. This requires

$$H_I \lesssim \Lambda_d \ , \tag{5.7}$$

where Λ_d denotes the scale of confinement of the strong interactions.

We also demand the classical relaxion evolution not to be spoiled by quantum fluctuations. To achieve this condition we require the classical spread of the relaxion field in one Hubble time, $\Delta\phi_{\rm cl} \sim \dot{\phi}/H_I \sim V'/H_I^2$, to be larger than the quantum spread $\Delta\phi_{\rm quantum} \sim H_I$, where V indicates the relaxion potential and the derivative is with

respect to the field ϕ. This implies a second upper bound on the scale of inflation that reads

$$H_I \lesssim \epsilon^{1/3}\Lambda \ . \tag{5.8}$$

The slow-rolling of the relaxion will stop when the slope of the potential matches the slope of the barrier [72]. From Eq.5.3, this implies

$$r\epsilon\Lambda^3 F \sim \Lambda_{\rm BR}^4. \tag{5.9}$$

A well motivated possibility is for the back-reaction potential to be generated by QCD becoming strongly interacting. This possibility is however ruled out by noticing that Eq.(5.9) defines the approximate value of ϕ at which the rolling stops

$$r\epsilon\Lambda^3\,\phi_{\rm stop} \sim r\epsilon\Lambda^3 F \Rightarrow \phi_{\rm stop} \sim \mathcal{O}(F) \text{ or } \theta = \frac{\phi}{F} \sim 1. \tag{5.10}$$

This result is in tension with the experimental constraint on the QCD θ-parameter, $\theta \lesssim 10^{-13}$ [167; 168].

An alternative possibility, already proposed in Ref.[72], is to introduce the so-called $L+N$ model, in which a new strongly interacting group is introduced. The lagrangian is

$$\mathcal{L} \supset m_L L L^c + m_N N N^c + y H L N^c + \widetilde{y} H^\dagger L^c N + \mathcal{L}_{\rm gauge}. \tag{5.11}$$

In Eq.(5.11), L and N are vector-like fermions with the same EW charges as lepton doublets and RH neutrinos, respectively. In addition, L is a heavy field, i.e. heavier than the EW scale. In contrast, N is a light fermionic field. The amplitude of the barrier can be estimated as (see Appendix E)

$$\Lambda_{\rm BR}^4 \simeq 4\pi\, f_{\pi'}^3\, m_N, \tag{5.12}$$

where $f_{\pi'}$ is the chiral symetry breaking scale. We thus have the hierarchy $m_L \gg f_{\pi'} \gg$

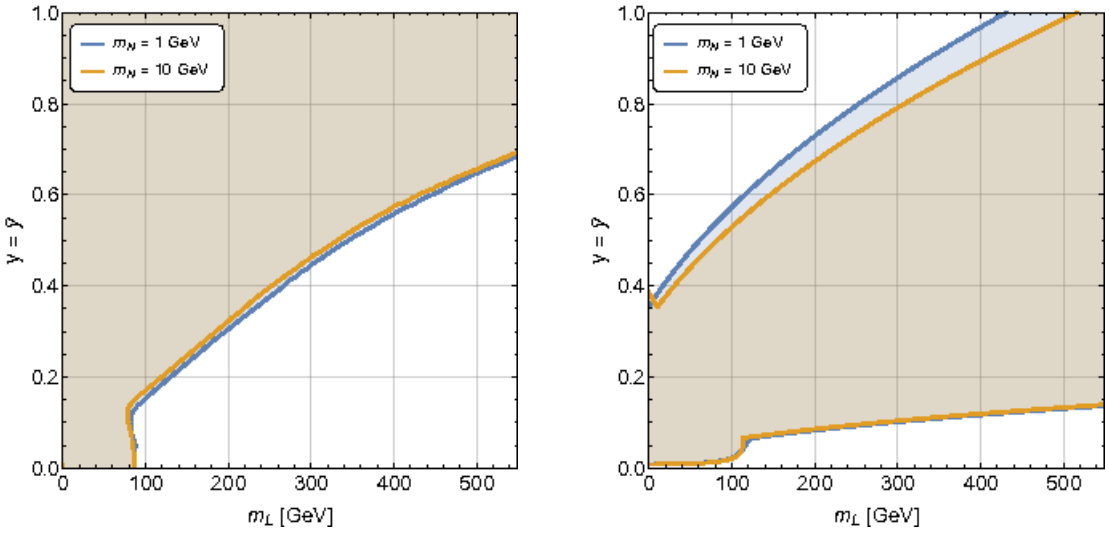

Figure 5.6: (Left) This plot shows the excluded (colored) region at 95% C.L. using electroweak precision measurements. (Right) In this other case, the excluded region at 95% C.L. was obtained from BR($h \to n_i \overline{n_j}$) < 20%. In both analysis the new strong group used is $SU(3)$ [169]. The same plane, m_L Vs. $y = \widetilde{y}$, was used in both plots.

m_N [72].

After integrating out the heavy field L, the Higgs contribution to the mass of N is $y\widetilde{y}\langle H\rangle^2/m_L$. One-loop contributions to the mass of N give $\sim \left(y\widetilde{y}/16\pi^2\right) m_L \log\left(M/m_L\right)$. In order for the Higgs contribution to be the leading one, we shall have

$$m_L < \frac{4\pi\langle H\rangle}{\sqrt{\log M/m_L}}. \tag{5.13}$$

From the latter bound we can see that the model would not work if m_L (or $f_{\pi'}$ [72]) is above a few hundreds of GeVs. Finally, Ref. [169] put bounds on the masses of the light fermions. We show the excluded (colored) regions in Fig. 5.6 in the plane m_L Vs. $y = \widetilde{y}$ for the choice of masses $m_N = 1, 10$ GeV. Note that the condition $y = \widetilde{y}$ is imposed. On the left-side of the figure electroweak precision measurements were used to obtain the excluded region. The excluded region on the right-side of the figure is obtained from the branching fraction of the Higgs decaying mode $h \to n_i \overline{n_j}$, i.e. BR($h \to n_i \overline{n_j}$) < 20%, where n_j ($j = 1, 2$) are the result of the mixing of the

neutral components of L, N, L^c and N^c at low energies.

5.4 Phase Transitions and Bubble Nucleation

5.4.1 Phase Transitions

A phase transition (PT) is a change on the state of a given system. The typical example is water. When it boils its state change from liquid to vapor, or if the temperature drops enough, from liquid to solid.

Any state can be characterized by using thermodynamic quantities, such as temperature, pressure, etc. A change in the values of those quantities could give us information about the existence of a PT, and provides also a way to classify PT as

- First Order (FOPT),
- Second Order (SOPT),
- Cross-Over.

In contrast to SOPT or cross-over, which are *smooth* processes, FOPTs are abrupt phenomena. In QFT a PT is described as a transition between one vacuum state to another [170]. If the evolution between vacua is continuous, we have a SOPT (or cross-over). In contrast, a discontinuous change in the ground state reveals a FOPT. In a FOPT there is also a discontinuity in the entropy [170]. Consequently, FOPT are phase transitions that can release a great amount of latent heat. For this reason, in what follows we are interested in FOPT.

5.4.2 Bubble Nucleation

At zero temperature these type of processes are modeled by the euclidean scalar action with potential $V(\phi)$:

$$S_E = \int d^4 x_E \left[\frac{1}{2} \partial_\mu \partial^\mu \phi + V(\phi) \right]. \tag{5.14}$$

However, zero temperature field theory is not enough to describe processes where the temperature is comparable with the energy scale of the theory. In those cases, thermodynamic effects become important. Therefore, ultimately, we are interested in processes at finite temperature, $T \neq 0$. We also look for stationary topological solutions of the equation of motions at finite T. These considerations lead to Eq.(5.14) to take the form $S_E \equiv S_3(T)/T$, where $S_3(T)$ is the finite temperature Euclidean three-dimensional action [171]

$$S_3 = 4\pi \int d\,r\, r^2 \left[\frac{1}{2} \left(\frac{d\,\Phi}{d\,r} \right)^2 + V(\Phi, T) \right], \tag{5.15}$$

where $V(\Phi, T)$ is called the thermal effective potential (the free-energy, F, in thermodynamic language). One important consequence is that now the field fluctuates around the minimum of the free-energy. From thermodynamics we have

$$F = E - TS, \tag{5.16}$$

where E and S stand for energy, and entropy, respectively. The equation of state also tells us that entropy can be computed by

$$S \equiv -\left(\frac{\partial\, F}{\partial\, T} \right). \tag{5.17}$$

These relations, when translated into the finite temperature field theory language, become:

$$V(\Phi, T) \;\; = \;\; \rho(\Phi, T) - T\, s(\Phi, T), \tag{5.18}$$

In Eq. (5.18), $\rho(\phi, T)$ is the *energy density*. The analogous expression of Eq.(5.17) for the *entropy density* is

$$s(\phi, T) \equiv -\left(\frac{\partial\, V(\phi, T)}{\partial\, T} \right). \tag{5.19}$$

Now that we have defined these important quantities, we shall pass to talk about the creation of bubbles, also called *bubble nucleation*. Let us suppose that the system defined by Eq. (5.14), at zero temperature, after spontaneous symmetry breaking has two degenerate minima, say $\Phi = \pm v$. As stated above, as the temperature becomes comparable to the energy scale of the theory, thermal effects become important. Consider the effective potential thermal $V(\Phi, T)$. The analogous situation with two degenerate minima defines the *critical temperature*, T_c. This means that at T_c the effective potential gets the same value for both minima

$$V(0, T_c) \equiv V(\langle\Phi\rangle, T_c) \tag{5.20}$$

where $\langle\Phi\rangle \neq 0$, see Fig.5.7. When the temperature is higher than the temperature associated with the symmetry breaking i.e. $T \gg T_c$, the minimum of the effective potential is located at the symmetric phase, i.e. $\langle\Phi\rangle = 0$. If the symmetric phase is realized as T increases the phenomenon is called symmetry restoration. By the inverse reasoning, as the temperature drops and reaches the critical temperature T_c a phase transition to the broken phase takes place. Those two local minima are sometimes classified as *true* and *false* vacuum, Φ_{true} and Φ_{false}, respectively. In general we have

$$V(\Phi_{\text{true}}, T) < V(\Phi_{\text{false}}, T). \tag{5.21}$$

After the temperature drops below T_c, the field still remains a time in the false vacuum before tunneling to the true one. This happens throughout the barrier separating the symmetric and broken phases, see Figs.5.7 and 5.8. For this reason, the false vacuum is called *metastable*. When the process described above happens in a region of space, the coexistence of two vacua produce a *bubble*. It is also said that a bubble has been *nucleated*. This nucleated bubble separates the true and the false vacuum: while the former remains inside the bubble, the metastable vacuum lives out of it and forms the background where the bubble grows. The phase boundary is called the *bubble wall*. In Fig.5.9 we show an example of this process.

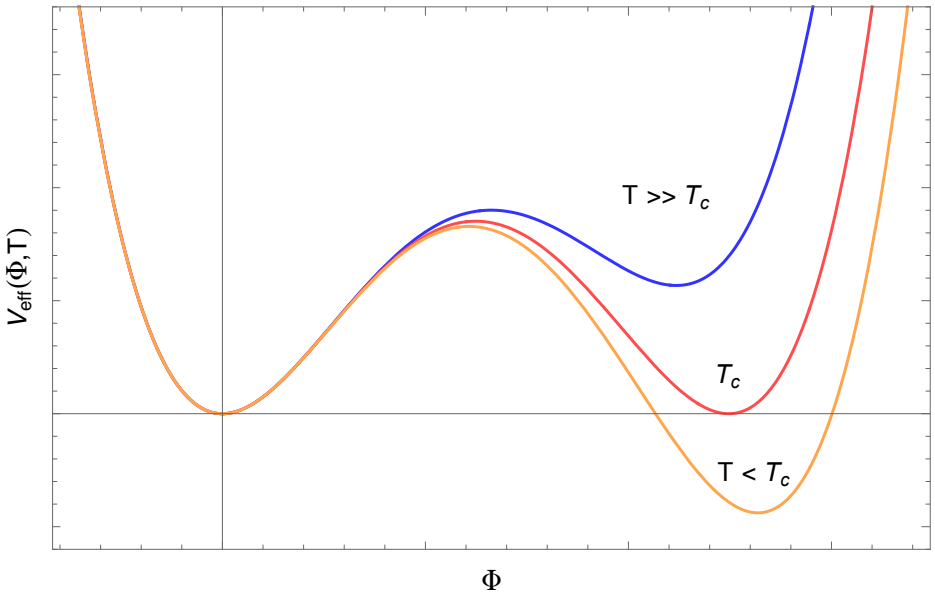

Figure 5.7: As the system cools down, the temperature drops and a FOPT takes place.

For the three dimensional Euclidean action the EoM is

$$\frac{d^2\Phi}{dr^2} + \frac{2}{r}\frac{d\Phi}{dr} = V'_{\text{eff}}(\Phi, T). \tag{5.22}$$

The bounce $\Phi_{\text{bnc}}(r)$ is a solution of the EoM given in Eq.(5.22) that smoothly connects the true and false vacuum. Hence, the boundary conditions for this solution are [171; 172]

$$\Phi(r) = 0, \text{ as } r \to \infty, \tag{5.23}$$

$$\frac{d\Phi(r)}{dr} = 0, \text{ as } r = 0. \tag{5.24}$$

Up to our present knowledge there is no general analytical solution for the bounce.

However, it is undeniable that an analytical analysis would be interesting. For this reason, in Appendix D we discuss the thin-wall approximation, with which it is possible to find analytical expressions for the radius of the bubble and the three-dimensional action S_3 [171]. In addition, we find an expression for the bounce.

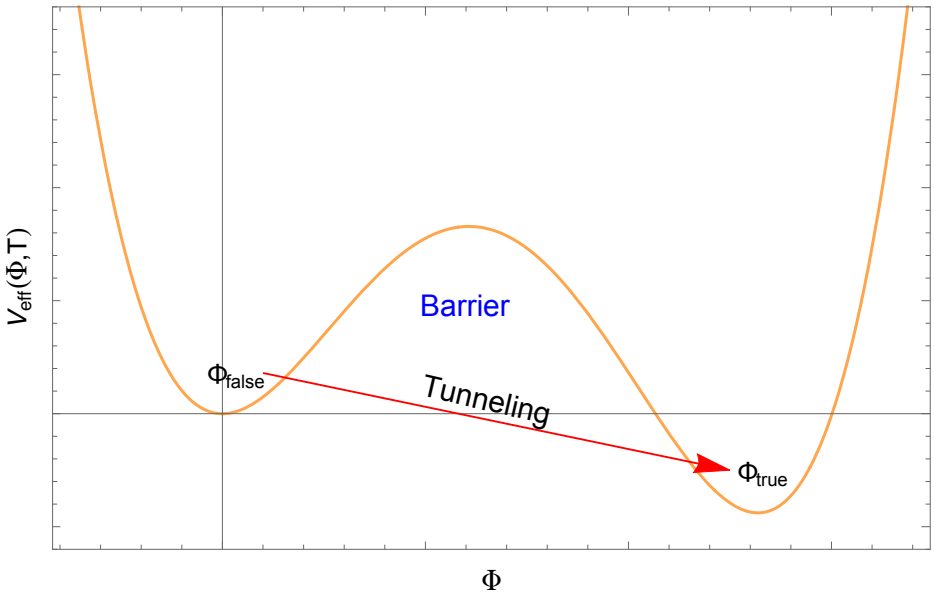

Figure 5.8: The tunneling between the false and true vacuum is described by the bounce.

5.5 Gravitational Waves

5.5.1 Gravitational Waves: Important parameters

Let us now discuss the parameters directly related to the phase transition under consideration: the nucleation temperature T_n, the inverse time duration β/H and the strength of the transition α. The first two parameters are defined in terms of the nucleation rate [171; 172]

$$\Gamma(T) = \mathcal{A}_{(T)}\, e^{-S_3/T} \ , \tag{5.25}$$

where S_3 is the Euclidian action computed at its bounce and $\mathcal{A}_{(T)}$ is a factor with units of $(\text{Mass})^4$. The nucleation temperature is defined as the temperature at which one of the nucleated bubbles reaches a size comparable to the Hubble radius at that time, $\Gamma(T_n) \simeq H^4(T_n)$. The latter condition guarantees that we have bubbles that do not collapse until they reach the size to have cosmological implications. Considering the process to take

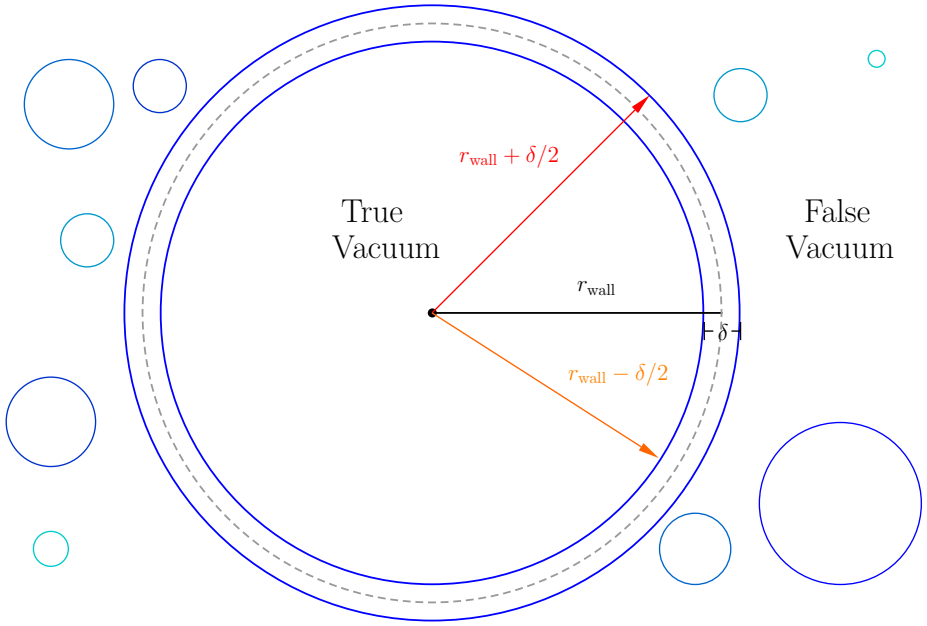

Figure 5.9: Nucleated bubble of δ thickness and radius $r_{\rm wall}$ containing the true vacuum in a false vacuum background. This figures is used in Appendix D in the thin-wall approximation.

place in the radiation domination epoch, the above statement implies [170; 173]

$$\frac{S_3}{T_n} \simeq 164.56 - 2\log\left(\frac{g_*}{100}\right) - 4\log\left(\frac{T_n}{1\,\text{GeV}}\right) . \tag{5.26}$$

The exact numerical value of the first term on the right-hand side depends on the precise form of $\mathcal{A}_{(T)}$, for simplicity we assume $\mathcal{A}_{(T)} \simeq T^4$. The inverse time duration β/H is instead defined as the rate of change of Γ at the nucleation time $t_{\rm nucl}$ via [174]

$$\beta \equiv \frac{1}{\Gamma}\frac{d\,\Gamma}{d\,t}\bigg|_{t_n} \Rightarrow \frac{\beta}{H} = T\,\frac{d}{dT}\left(\frac{S_3}{T}\right)\bigg|_{T=T_n} . \tag{5.27}$$

The strength of the transition, α, is instead not univocally defined. In the literature many definitions can be found [28; 175; 176; 177]. The most common are based on the latent heat and on the trance anomaly. In the first one α is identified as the ratio between the latent heat of the transition and the energy density of the radiation in the plasma $\rho_{\rm rad}$. In the second one it is defined through the trace of the the stress-energy tensor and $\rho_{\rm rad}$. From the practical point of view, both definitions can be summarized

as

$$\alpha = \frac{1}{\rho_{\rm rad}} \left(\Delta V - n\, T\, \frac{\partial \Delta V}{\partial T} \right) \Big|_{T=T_n} , \tag{5.28}$$

where $\Delta V = V_{\rm eff}(\Phi_{\rm false}, T) - V_{\rm eff}(\Phi_{\rm true}, T)$[1] is the difference of the free energy density between the two phases and $n = 1$ (1/4) when α is defined via the latent heat (trace of the stress-energy tensor).

5.5.2 Computation of the gravitational wave spectrum

After bubble collisions part of the latent heat is transferred to the plasma and converted into bulk flow, while the rest goes to the scalar field in the form of kinetic energy. The ratio of the energy converted into gravitational waves in the direction $\widehat{k}$ into the solid angle $d\,\Omega$ at frequency ω defines the spectrum [170]

$$\Omega_{\rm GW} \equiv \omega \frac{dE_{\rm GW}}{d\omega} \frac{1}{E_{\rm Tot}}, \tag{5.29}$$

where

$$\frac{dE_{\rm GW}}{d\Omega\, d\omega} = 2G\omega^2\, \Lambda_{ij,lm}(\widehat{k}) \widetilde{T}^*_{ij}(\widehat{k},\omega)\, \widetilde{T}_{lm}(\widehat{k},\omega). \tag{5.30}$$

In this equation $\widetilde{T}_{ij}(\widehat{k},\omega)$ is the space-space components of the Fourier transform of the stress energy tensor

$$\widetilde{T}_{ij}(\widehat{k},\omega) = \frac{1}{2\pi} \int dt\, e^{i\omega t} \int d^3x\, T_{ij}(x,t)\, e^{-ik\cdot x}, \tag{5.31}$$

and $\Lambda_{ij,lm}$ is the projection tensor for gravitational radiation [170; 178]:

$$\Lambda_{ij,lm} = \delta_{il}\delta_{jm} - 2\widehat{k}_j\widehat{k}_m\delta_{ij} + \frac{1}{2}\widehat{k}_i\widehat{k}_j\widehat{k}_l\widehat{k}_m - \frac{1}{2}\delta_{ij}\delta_{lm} + \frac{1}{2}\delta_{ij}\widehat{k}_l\widehat{k}_m + \frac{1}{2}\delta_{lm}\widehat{k}_i\widehat{k}_j. \tag{5.32}$$

Hence, different sources that contribute to the stress energy tensor shall affect the gravitational wave spectrum.

[1] From now on we consider $\Phi_{\rm false} = 0$.

We now quickly remind the reader how the computation of the spectrum of the stochastic GW background produced in a first order phase transition proceeds. Three contributions must be considered [179]: the one from true vacuum bubble collisions, $\Omega_{\rm col}\, h^2$, the one from the propagation of sound waves in the plasma, $\Omega_{\rm sw}\, h^2$, and the one from magnetohydrodynamic turbulence effects, $\Omega_{\rm turb}\, h^2$:

$$\boxed{\Omega_{\rm total}\, h^2 \simeq \Omega_{\rm col}\, h^2 + \Omega_{\rm sw}\, h^2 + \Omega_{\rm turb}\, h^2}. \tag{5.33}$$

A fourth contribution may be generated by quantum fluctuations [170], but since its impact is not well understood we will not consider it in the following.

In a strongly interacting theory, after confinement takes place, the radial degree of freedom (associated with the chiral symmetry breaking) interacts with the light particles in the plasma. We thus expect the interactions between the scalar shell and the plasma to be important, causing the behavior of the bubble to be a *non-runaway* one [152], that is the bubble walls do not keep accelerating until the bubbles collide. Since in this case most of the latent heat of the phase transition is transferred to the plasma in the form of sound waves and turbulence, in the following we will focus on the $\Omega_{\rm sw}\, h^2$ and $\Omega_{\rm turb}\, h^2$ contributions only. Their expressions can be written in a compact way as [152; 153; 176; 180; 181; 182]

$$\Omega_i h^2 = a_i \left(\frac{\beta}{H}\right)^{-1} \left(\frac{\kappa_i\, \alpha}{1+\alpha}\right)^{b_i} \left(\frac{100}{g_\star}\right)^{1/3} v_{\rm wall}\, S_i(f)\ , \tag{5.34}$$

where $i =$ sw or turb for the sound waves and turbulence contributions, respectively. The details of the phase transition enter in the parameters α, β/H and T_n, which we will discuss in detail below. As for the other parameters, the numerical coefficients a_i in the two cases are given by [152; 153; 176; 180]

$$a_{\rm sw} = 2.65 \times 10^{-6}\ , \qquad a_{\rm turb} = 3.35 \times 10^{-4} \tag{5.35}$$

and the exponents b_i are

$$b_{\rm sw} = 2 \ , \qquad b_{\rm turb} = 3/2 \ . \tag{5.36}$$

Again, $g_\star$ denotes the number of relativistic degrees of freedom and H is the Hubble parameter, where both quantities are computed at the nucleation temperature. The quantity $v_{\rm wall}$ is the wall velocity. It is known that scenarios with large $v_{\rm wall}$ lead to stronger GW signals [28; 152; 175; 177]. While in the non-runway behavior the bubble walls stop their acceleration and reach a terminal velocity, this velocity might still be relativistic. Calculating the specific value of $v_{\rm wall}$ is beyond the scope of the present thesis. We will then concentrate on the case of highly relativistic bubbles, $v_{\rm wall} \sim 1$, since it is the most interesting regime from an observational point of view. Decreasing $v_{\rm wall}$ down to $v_{\rm wall} \sim 0.75$ doesn't drastically modify the overall picture, see *e.g.* [177]. Finally, the coefficients κ_i are the efficiencies of each process. The former is the efficiency to convert the latent heat into bulk motion, while the latter is the part that is converted into vorticity in the plasma. Numerical fits of $\kappa_{\rm sw}$ suggests the form [152; 175]

$$\kappa_{\rm sw} \simeq \frac{\alpha}{0.73 + 0.083\sqrt{\alpha} + \alpha} \ , \tag{5.37}$$

for $v_{\rm wall} \sim 1$, where α was defined in Eq.(5.28). $\kappa_{\rm turb}$ is determined trough $\kappa_{\rm turb} = \epsilon\, \kappa_{\rm sw}$. Previous studies suggest the conservative value of $\epsilon = 5 \times 10^{-2}$ [152; 183; 184]. As for the spectral shapes $S_i(f)$, they read

$$S_{\rm sw}(f) = \frac{f^3}{f_{\rm sw}^3} \left(\frac{7}{4 + 3\frac{f^2}{f_{\rm sw}^2}} \right) , \qquad S_{\rm turb}(f) = \frac{f^3}{f_{\rm turb}^3} \frac{\left(1 + \frac{f}{f_{\rm turb}}\right)^{-\frac{11}{3}}}{1 + 8\,\pi\, f/\tilde{h}} . \tag{5.38}$$

In the previous expression $\tilde{h}$ is the Hubble rate at t_n redshifted to today,

$$\tilde{h} = 1.65 \times 10^{-5}\,{\rm Hz} \left(\frac{T_n}{100\,{\rm GeV}} \right) \left(\frac{g_\star}{100} \right)^{1/6} \ , \tag{5.39}$$

while the peak frequencies in the two cases are given by similar expressions,

$$f_i = f_i^0 \, \frac{1}{v_{\rm wall}} \, \frac{\beta}{H} \, \frac{T_n}{100\,{\rm GeV}} \, \left(\frac{g_\star}{100}\right)^{1/6} \, , \tag{5.40}$$

with $f_{\rm sw}^0 = 1.9 \times 10^{-5}$ Hz and $f_{\rm turb}^0 = 2.7 \times 10^{-5}$ Hz. It has been suggested in [176; 184] that when $\beta/H \gg 1$, the sound wave and the turbulence contributions shown above *overestimate* and *underestimate* the signal, respectively. Following the suggestion in the same works, we modify $\Omega_{\rm sw}\, h^2$ and $\Omega_{\rm turb}\, h^2$ to

$$\Omega_{\rm sw}^{\rm fast}\, h^2 = (\tau_{\rm sw}\, H)\; \Omega_{\rm sw}\, h^2 \, , \quad \Omega_{\rm turb}^{\rm fast}\, h^2 = (1 - \tau_{\rm sw}\, H)\; \Omega_{\rm turb}\, h^2 \big|_{\kappa_{\rm turb} = \kappa_{\rm sw}} \, , \tag{5.41}$$

where

$$\tau_{\rm sw}\, H = (8\pi)^{1/3} \, \frac{v_{\rm wall}}{\overline{U}_f \; (\beta/H)}$$

is related to the duration of sound waves and $\overline{U}_f$ is the root-mean-square four velocity of the plasma.

Gravitational tests of electroweak relaxation

5.6 Relaxation with strongly interacting fermions

A possible origin for the back-reaction potential, already considered in the original work [72], involves fermions charged under new strong interactions $\mathcal{G}_{\rm dark}$ as well as under EW interactions. Provided that the scale of inflation is smaller that the confinement scale of $\mathcal{G}_{\rm dark}$, which we will denote as $g_\rho f$, and that the Higgs boson interacts with the new fermions, the back-reaction potential forms and, as described in App. E.1, $\Lambda_{\rm BR}$ takes the form

$$\Lambda_{\rm BR}^4 \simeq \left| \mu_B^2 H^\dagger H - \Lambda_0^4 \right| \, , \tag{5.42}$$

where the constants μ_B^2 and Λ_0^4 depend on the specific model considered. The form of Eq. (5.42) is however generic.

In addition to the conditions for a successful relaxation given before, the present model has some extra conditions.

Conditions on the back-reaction: The term Λ_0^4 is present in the back-reaction potential even before EWSB. To guarantee that it does not stop the relaxion evolution we require

$$\Lambda^3 > \frac{\Lambda_0^4}{r\epsilon F} \ . \tag{5.43}$$

In addition, to ensure that after EWSB there will be a period of evolution in which the height of the barrier grows, we need

$$v_{\rm EW}^2 \mu_B^2 > \Lambda_0^4 \qquad \text{and} \qquad \Lambda < \frac{\mu_B^2}{\epsilon F} \ . \tag{5.44}$$

The EW scale is an output of the relaxation: An approximate expression for the EW VEV in terms of the parameters of the model is

$$v_{\rm EW}^2 \simeq \frac{\epsilon \Lambda^3 F + \Lambda_0^4}{\mu_B^2 - \epsilon \Lambda F} \ . \tag{5.45}$$

As shown in Appendix F.1, the cutoff satisfy

$$\Lambda \lesssim 6.7 \times 10^6 \, \text{GeV} \ \left[\frac{\mu_B}{10 \, \text{GeV}}\right]^{2/3} \left[\frac{10^{-30}}{\epsilon}\right]^{1/3} \left[\frac{10^{16} \, \text{GeV}}{F}\right]^{1/3} \left[1 - \frac{\Lambda_0^4}{\mu_B^2 v^2}\right]^{1/3} \ , \tag{5.46}$$

favoring thus very small values of ϵ. This result can be problematic in two aspects: *i*) to completely solve the hierarchy problem an additional protection mechanism must be present for scales between Λ and $M_{\rm Pl}$, and *ii)* a successful relaxation requires the relaxion excursion to be at least $\Delta\phi \sim \Lambda/\epsilon$ in order for the Higgs mass parameter to change sign. Given the very small ϵ needed for the mechanism to work, the resulting excursion is transplanckian. The first issue can be solved assuming supersymmetry [185; 186; 187], a composite dynamics [188] or a warped dimension [189] to be present above Λ. The second problem requires more model building effort, but can be solved in the context of clockwork models [190; 191; 192; 193]. In the following we assume that one of these mechanisms is present to stabilize the EW scale

all the way up to the Planck scale, and focus only on the effective field theory defined by Eq. (5.3).

5.7 Evolution after reheating

As already mentioned, we are considering a situation in which the relaxation of the EW scale happens during inflation, *i.e.* the correct EW VEV is selected at the end of this phase. This leaves open the question of *what happens after reheating?* One possibility is for reheating to leave the Universe in a bath with temperature $T_{\rm RH} \lesssim \Lambda_d$. In this case there is no further dynamical evolution in the relaxion field direction, since ϕ remains stuck in its minimum. If $T_{\rm RH} > T_{\rm EW}$, with $T_{\rm EW}$ the scale of EW phase transition, we expect thermal corrections in the Higgs field direction to recover the EW symmetry. As the Universe expands and cools down, EWSB is again triggered as usual [1].

A second possibility, on which we focus in the following, is for reheating to happen at $T_{\rm RH} > T_n$, where T_n is the nucleation temperature of the additional strong interaction $\mathcal{G}_{\rm dark}$. If this is the case, after reheating the back-reaction disappears and the Universe undergoes then a second period of relaxation. This possibility has received less attention from the literature, see *e.g.* [121; 138; 194; 195]. As the Universe expands and cools down, it will again reach a temperature $T \sim T_n$ at which the new strong sector again confines, thus producing again the back-reaction barrier and ultimately stopping the relaxion evolution [2]. As we are going to see at the end of this Section, the relaxion evolution stops soon after the barrier is again formed. If the transition producing the back-reaction barrier is strongly first order, it will produce a GW signal that might be observable at interferometer experiments, as we will study in Sec. 5.8. This allows to open a new window on this type of solutions of the hierarchy problem.

Let us now discuss more in detail the relaxion evolution when $T_{\rm RH} > T_n$. We want to understand whether this additional relaxation phase can spoil the solution of the hierarchy

[1] Since the portal coupling between the Higgs and the relaxion sectors is small, we do not expect significant modifications to the EW phase transition with respect to what happens in the SM.

[2] Note that the oscillations of the relaxion around the minimum can make it a viable candidate for dark matter [195].

problem. We achieve this by imposing additional conditions on the parameters in order to achieve the correct EW minimum today. We need to consider three situations, depending on the relative hierarchy between $T_{\rm RH}$, T_n and $T_{\rm EW}$:

- If $T_n < T_{\rm RH} < T_{\rm EW}$ the Universe is reheated to a phase in which the scalar potential has already a non-trivial minimum in the Higgs direction, while there are no barriers in the relaxion direction. Using the potential in Eq. (5.3) in the equation of motion $\ddot{\theta} + 3H(t)\dot{\phi} + \partial V/\partial\phi = 0$ we obtain

$$\ddot{\theta} + \frac{3}{2t}\dot{\theta} = \frac{1}{F^2}\left(r\epsilon F\Lambda^3 + \epsilon F\Lambda v^2(\theta)\right) , \tag{5.47}$$

  where

$$v^2(\theta) = \frac{-\Lambda^2 + \epsilon F\Lambda\,\theta}{2\lambda} \tag{5.48}$$

  is the Higgs VEV in the absence of the back-reaction barrier. We have used $H = 1/(2t)$, as appropriate for a radiation dominated Universe. The solution for temperatures $T_n < T < T_{\rm RH}$ can be written analytically in terms of modified Bessel functions I_n and K_n of first and second kind, respectively [1]. To write a compact expression we define a new time variable $\tau = \epsilon\Lambda t/\sqrt{2\lambda}$, the functions

$$f(\tau) = \frac{I_{1/4}(\tau)}{\tau^{1/4}} , \qquad g(\tau) = \frac{K_{1/4}(\tau)}{\tau^{1/4}} , \tag{5.49}$$

  and the constant term

$$\xi = \frac{(2r\lambda - 1)\Lambda^2}{\sqrt{2\lambda}F^2} . \tag{5.50}$$

  The solution can be written as

$$\theta(\tau) = -\xi + \frac{g_0\theta_0' - g_0'(\theta_0 + \xi)}{f_0'g_0 - f_0g_0'}f(\tau) + \frac{-f_0\theta_0' + f_0'(\theta_0 + \xi)}{f_0'g_0 - f_0g_0'}g(\tau) , \tag{5.51}$$

  where the primes denote the derivative with respect to τ, and the subscript 0 indicates that the quantity must be computed at the initial time, *i.e.* at reheating. Assuming

[1] In Wolfram Mathematica these functions are called BesselI and BesselK, respectively.

reheating to be an instantaneous process, we can identify θ_0 with the value of the relaxion field at the end of the inflationary period and we can assume that the relaxion field does not acquire a relevant dynamics during reheating, leading to $\dot{\theta}_0 \simeq 0$. We also notice that for large values of τ we have the asymptotic behavior $I_n(\tau) \sim e^{\tau}/\sqrt{\tau}$ and $K_n(\tau) \sim e^{-\tau}/\sqrt{\tau}$. For large τ we thus obtain

$$\theta(\tau) \simeq -\xi + \left(\frac{\tau_0}{\tau}\right)^{3/4} \cosh(\tau - \tau_0)\,(\theta_0 + \xi) + \left(\frac{\tau_0}{\tau}\right)^{3/4} \sinh(\tau - \tau_0)\,\theta_0' \ . \tag{5.52}$$

The dependence on hyperbolic trigonometric functions implies that the relaxion field will evolve very quickly, if enough time is allowed to pass. We will comment later on the dynamics taking place for $T < T_n$;

- If $T_n < T_{\rm EW} < T_{\rm RH}$ there are two phases in the evolution. The first one applies for $T_{\rm EW} < T < T_{\rm RH}$ while the second one for $T_n < T < T_{\rm EW}$. In the first phase the equation of motion to be solved is Eq (5.47) with $v^2(\theta) = 0$. The solution can again be written analytically:

$$\theta(t) = \theta(T_{\rm RH}) + \frac{r\epsilon\Lambda^3}{5F}(t^2 - 5T_{\rm RH}^2) + \frac{4r\epsilon\Lambda^3 T_{\rm RH}^{5/2}}{5F\sqrt{t}} \ . \tag{5.53}$$

Notice that the evolution is a power law in this regime, and the relaxion field evolves much less than what happens when $v^2(\theta) \neq 0$. Using the relation between time and temperature in a radiation domination Universe

$$H^2 = \frac{1}{4\,t^2} = \frac{1}{3M_{\rm Pl}^2}\frac{\pi^2}{30} g_\star T^4 \ , \tag{5.54}$$

where $g_\star$ denotes the number of relativistic degrees of freedom we can rewrite the solution as

$$\theta(T) = \theta(T_{\rm RH}) + \frac{9}{2\pi^2 g_\star}\frac{r\epsilon\Lambda^3 M_{PL}^2}{F}\frac{4T^5 - 5T^4 T_{\rm RH} + T_{\rm RH}^5}{T^4 T_{\rm RH}^5} \ . \tag{5.55}$$

Once EWSB is triggered the equation of motion to be solved is again Eq. (5.47) with

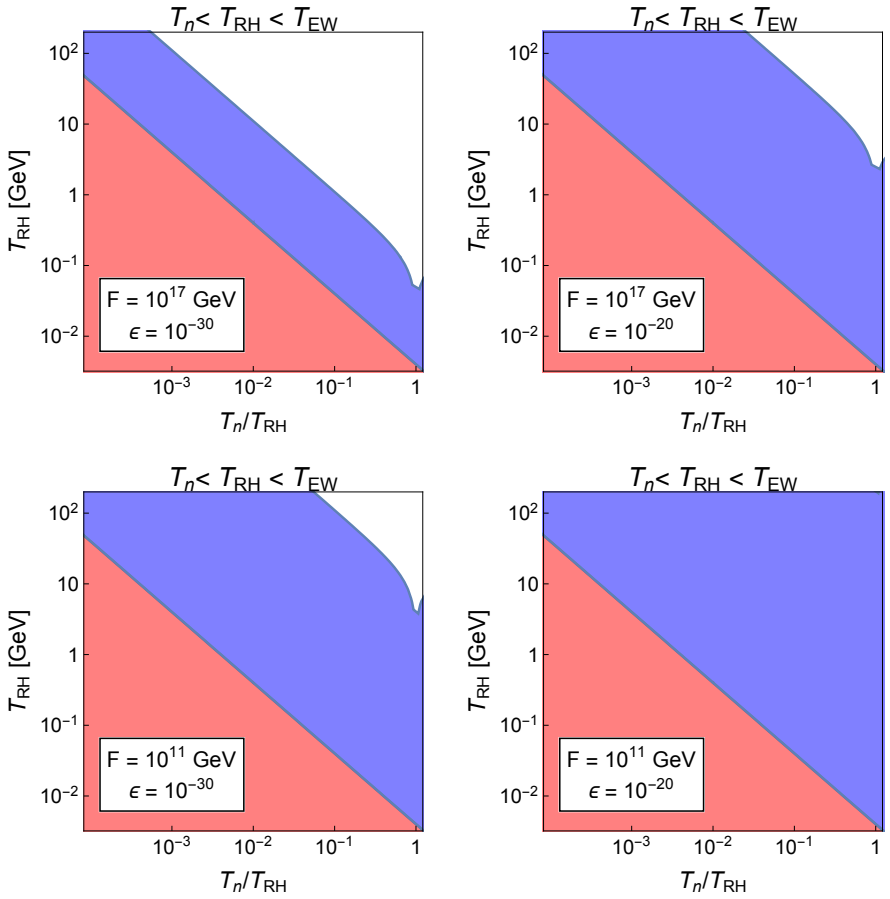

Figure 5.10: Regions in which the relative variation of the Higgs VEV of Eq. (5.56) is larger than unity (blue) and therefore the solution of the hierarchy problem is spoiled and in which the nucleation or the reheating temperatures are smaller than 4 MeV (red). We suppose the initial VEV to be $v_{\rm EW}$. All the plots show the $T_n < T_{\rm RH} < T_{\rm EW}$ case. See the text for more details.

$v^2(\theta) \neq 0$, whose solution is given in Eq. (5.51) with $\tau_0 \equiv \tau_{EW}$;

- The last case is the one in which $T_{\rm EW} < T_n < T_{\rm RH}$. For $T_n < T < T_{\rm RH}$ the solution is given by Eq. (5.53), while we will discuss in the next paragraph what happens for $T < T_n$.

To compute the solution for $T < T_n$ we need to turn on not only the Higgs VEV, for $T < T_{\rm EW}$, but the back-reaction barrier as well. To the best of our knowledge, no analytical solution can be found in this case. We can however qualitatively expect that, once the barriers form,

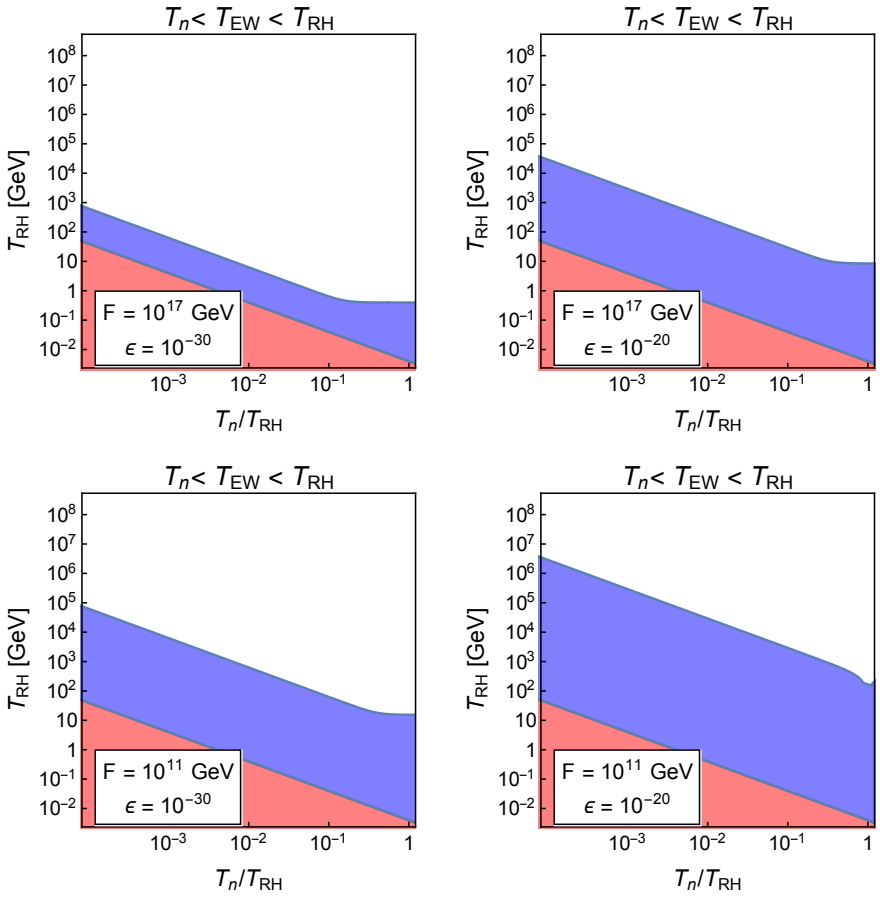

Figure 5.11: Regions in which the relative variation of the Higgs VEV of Eq. (5.56) is larger than unity (blue) and therefore the solution of the hierarchy problem is spoiled and in which the nucleation or the reheating temperatures are smaller than 4 MeV (red). We suppose the initial VEV to be $v_{\rm EW}$. All the plots show the $T_n < T_{\rm EW} < T_{\rm RH}$ case. See the text for more details.

the relaxion will find itself trapped in a position which is displaced from the minimum in the relaxion direction. It will then oscillate around this minimum losing energy. It is in this phase that it can behave like dark matter, as studied in [195]. Whether or not the relaxion stops its evolution when encountering the first barrier will depend on the velocity it has acquired during the second relaxation phase, and cannot be inferred analytically. As shown at the end of App. F.1 however, the change in the Higgs VEV between two subsequent minima is relatively small, so that it is likely that the second stopping phase will not modify dramatically the value of the Higgs VEV at the end of the relaxion evolution. What can

modify dramatically this value is however the relaxion evolution before the barrier is again formed. To understand whether this is the case, we show in Fig. 5.10 and Fig. 5.11 in blue the regions in which

$$\frac{\delta v}{v} \equiv \frac{v[\theta(T_n)] - v_{EW}}{v_{EW}} > 1 \ . \tag{5.56}$$

In this regions the Higgs VEV at the end of the second relaxation phase differs by more than a factor of 2 with respect to the observed VEV, and the solution of the hierarchy problem is spoiled. In Fig. 5.10 we consider the case in which $T_n < T_{\rm RH} < T_{\rm EW}$, while in Fig. 5.11 we show the case in which $T_n < T_{\rm EW} < T_{\rm RH}$. We take $T_{\rm EW} \simeq 160$ GeV. We have fixed the parameters of the model to the same representative values chose in Eq. (5.46), with the exceptions of ϵ and F, whose values are reported in the plots. For simplicity we have taken a fixed value of $g_\star = 100$, although by varying it the overall picture does not change. Furthermore, we have supposed that the initial relaxion value at reheating gives $v_{\rm EW}$ and has vanishing velocity. The quantity $v[\theta(T_n)]$ is computed using Eqs. (5.51) and (5.55). We also impose a lower bound $T_n, T_{\rm RH} \gtrsim 4$ MeV, represented by the red regions, where the limit on $T_{\rm RH}$ is taken from [196] while the limit on T_n is imposed to be safely far from the Big Bang nucleosynthesis epoch $T \sim 1$ MeV. By inspecting Fig. 5.10 we see that for reheating temperatures below the EW phase transition one, there are regions in parameter space in which the solution of the hierarchy problem is completely spoiled, depending on the choice of parameters. This is due to the exponential evolution of the relaxion field in this regime. On the contrary, when $T_n < T_{\rm EW} < T_{\rm RH}$ most of the relaxion evolution happens when Eq. (5.55) is valid. Since the relaxion field does not evolve much in this regime, there are large regions of parameter space in which the modifications of the VEV are small. Finally, when $T_{\rm EW} < T_n < T_{RH}$ the evolution follows again Eq. (5.55) and is not enough to drastically modify the value of the VEV. For this reason we do not show any plot for this case.

Let us finish this Section noticing that we can imagine a situation in which the VEV at the end of the first relaxation phase is smaller than observed Higgs VEV. If this is the case, the second relaxation phase could provide the additional evolution needed to be compatible with experiments. In this paper we will focus on a situation in which the correct Higgs VEV is selected at the end of the first relaxation phase, leaving for future work the analysis of

what happens in the opposite situation.

5.8 Gravitational waves signal

In relaxion models with strongly interacting fermions there are two main sources of GW: *i)* the confinement of $\mathcal{G}_{\text{dark}}$ if it proceeds through a first order phase transition [28; 177] and *ii)* the possible penetration of the barrier by the relaxion field before stopping at the minimum [197; 198; 199]. Since the last process is much more difficult to analyze, we will focus here on the first signal, leaving the second one for future work. Since the confinement dynamics of $\mathcal{G}_{\text{dark}}$ is a non-perturbative process, it is difficult to make quantitative predictions on the GW spectra that can be produced. The phase transition ultimately depends on the phase diagram of the theory, whose determination requires computationally expensive lattice computations. We can however have an order of magnitude estimate of the expected signal using effective models to parametrize the confining dynamics. As shown in [177], in QCD-like theories different effective models give GW spectra whose peak amplitude might differ even by two order of magnitudes between each other. Nevertheless they can give a useful indication of what kind of theories can produce a GW spectra which is close enough to current and future experimental sensitivities, and that thus deserve further dedicated theoretical studies to allow for a more precise study of the phase transition and of the associated GW signals. In this work we decide to focus on the linear sigma model description of a confining strong dynamics, which is introduced in Chapter 2 and also is defined in Eq. (E.7) of Appendix E.1.1. We nevertheless stress that our results should be taken as a preliminary indication for what the real GW spectrum could be, as recently also emphasized in [28; 177].

As already mentioned in the Introduction, a well-known argument by Pisarski and Wilczek [150] implies that $SU(N_d)$ gauge theories with $N_d \geq 3$ feature a first order phase transition if $N_F \geq 3$ light [1] flavors are present, see Appendix G. Motivated by this result, we study here $SU(N_d)$ gauge theories with $N_F = 3$ and $N_F = 4$ flavors, considering both the situations in which the new confining phase transition happens at a scale below and above the EW critical

[1] That is with a mass smaller than the new gauge theory confinement scale.

temperature $T_{\rm EW}$. A general discussion of these models in the relaxion framework can be found in App. E.1.2. We keep our discussion general, but to make it more concrete it is useful to take as an example the variations of the $L+N$ model shown in Fig. E.1, where L and N are new vector-like fermions in the fundamental of $SU(N_d)$ with the quantum number of the SM lepton doublet and of a total singlet, respectively. We see that the physics of the $N_F = 3$ case is captured by the minimal $L+N$ model with dark confinement scale above the EW one (model A), as well as the physics of models in which we add 3 singlets to the spectrum independently on the confinement scale (models B and D). Notice that the EW charged fermion L cannot be too light in order to evade current experimental direct searches bounds, and we then assume it to have a mass larger than $\Lambda_{\rm EW}$. The physics of the $N_F = 4$ dark flavors, on the contrary, is captured by the minimal model with two copies of L fermions and a decoupled singlet (model C), and of models in which L is decoupled and 4 light dark N flavors are added to the spectrum (models B and D with $n_N = 4$). Experimental bounds on the minimal $L+N$ model have been considered in [169; 200; 201] (see also Fig.5.6). Although important, these bounds allow for rather different spectra at the level of sigma model without spoiling the successful relaxation of the EW scale.

5.8.1 Gravitational wave spectrum: QCD-like case

We now compute the GW spectrum using the linear sigma model defined in App. E.1.1 with the formalism of Sec. 5.5.2. We refer the reader to the Appendix for a definition of the notation we use for the linear sigma model. We focus here on the situation in which the masses of the σ and η' mesons satisfy $m_{\sigma,\eta'} \gtrsim f_\pi$, where f_π is the pion decay constant. Since this is the well-known spectrum of QCD, we use the term "QCD-like" to refer to this case. We will study in Sec. 5.8.2 a different physical spectrum. In our computation we consider the chiral limit, in which the mass of the lightest fermions is much smaller than the confinement scale Λ_d and we focus on the $N_F = 3$ and $N_F = 4$ cases. We present our results for two specific values of T_n: one where $T_n < T_{\rm EW}$ and one where $T_n > T_{\rm EW}$, thus capturing the different possibilities discussed in Sec. 5.7. In particular we fix the values of the linear sigma model parameters for the two cases as reported in Tab. 5.1, where we also indicate the values of

QCD-like case $N_F = 3$

	$T_n < T_{\rm EW}$	$T_n > T_{\rm EW}$
m_Σ^2 [GeV^2]	64	64
λ	1.5	1.5
κ	4	4
μ_Σ [GeV]	10^2	10^4
f_π [GeV]	24.7	2.4×10^3
m_σ [GeV]	36.9	3.4×10^3
$m_{\eta'}$ [GeV]	60.9	5.9×10^3
m_S [GeV]	60.8	5.9×10^3
T_n [GeV]	25.2	2.3×10^3
α	0.00317	0.0312
β/H	11921.4	7904.9

QCD-like case $N_F = 4$

	$T_n < T_{\rm EW}$	$T_n > T_{\rm EW}$
m_Σ^2 [GeV^2]	676	6.4×10^5
λ	2	2
κ	4	3
μ_Σ	9	9
f_π [GeV]	30	1.1×10^3
m_σ [GeV]	36.8	1.1×10^3
$m_{\eta'}$ [GeV]	90.1	3.4×10^3
m_S [GeV]	76.5	2.8×10^3
T_n [GeV]	28.6	0.9×10^3
α	0.00283	0.0054
β/H	66894.1	15694.5

Table 5.1: Values of the linear sigma model parameters, physical meson masses and relevant quantities entering the GW spectrum calculation of the $N_F = 3$ and $N_F = 4$ for the QCD-like cases.

the chiral symmetry breaking VEV, the relevant mesons masses, the nucleation temperature T_n and of the main parameters entering the GW spectrum computation. In choosing these benchmark point we have scanned the linear sigma models parameters trying to maximize the GW spectrum for both nucleation temperatures. In the lack of analytical expressions for α and β/H this represents a challenging numerical process. As already stressed in [177] it is interesting to notice that large values of β/H are found. This is to be contrasted with the naive estimate

$$\frac{\beta}{H} \simeq 4 \log \frac{M_{\rm Pl}}{T_n} \simeq \mathcal{O}(100) \ . \tag{5.57}$$

Since for the sound waves and turbulence contribution the GW amplitude decreases linearly with β/H, see Eq. (5.34), while the peak frequency increases linearly with it, see Eq. (5.40), the direct computation of β/H through an explicit, although effective, model has a strong consequence for the observability of the GW spectra. All together our results for the QCD-like case are shown in Fig. 5.12 for the $N_F = 3$ and $N_F = 4$ models in the upper and lower panels respectively. There, the left and right panels correspond to the $T_n < T_{\rm EW}$ and $T_n > T_{\rm EW}$ cases. In all plots the blue line shows the spectrum computed using Eq. (5.34), while the red line is computed using the modification presented in Eq. (5.41), which explicitly show

the suppression factor due to the decrease of the sound wave contribution. The situation depicted in the left panels can be realized, in the relaxation framework we are considering, when $T_n < T_{\rm RH} < T_{\rm EW}$ or when $T_n < T_{\rm EW} < T_{\rm RH}$. As shown in Sec. 5.7 in the first case large regions of parameter space end up with large variations on $v_{\rm EW}$ from the second relaxation phase, leaving thus $T_{\rm EW} < T_{\rm RH}$ as the preferred case [1]. The situation of the right panels refers instead to the case $T_{\rm EW} < T_n < T_{\rm RH}$, for which we showed that large regions of parameter space are compatible with a small variation of the EW VEV during the second relaxation phase. In all the figures the colored regions represent the sensitivities of future interferometer experiments. In particular we show the projected reach from AstroD-GW [154; 155], eLISA [154; 202], BBO [154; 156], DECIGO [154; 156], B-DECIGO [154; 156], AION [157], MAGIS [158], ET [159] and CE [160]. As we see from Fig. 5.12, both for $N_F = 3$ and $N_F = 4$ cases the GW signal from the dark phase transition is a few orders of magnitude below the region that can be probed in future experiments, in agreement with previous results obtained in similar frameworks [28; 177]. We stress again, however, that these results must be interpreted as an order-of-magnitude estimate since, as shown in [177], different effective models for the strong sector confining dynamics can give results that might differ even by two orders of magnitude for the amplitude of the signal and that might then fall on the edge of detectability. Notice also that changing N_F does not dramatically change the region in which the signal falls, making thus difficult the identification of the underlying model in case a signal is detected. We conclude emphasizing once more that, according to the discussion in Appendix E.1.2, the strongly interacting models generating the back-reaction potential in the relaxion mechanism do not suffer from very strong experimental limits. In particular, it is not difficult to obtain in such models the spectrum used in this section.

5.8.2 Gravitational wave spectrum: non QCD-like case

We now turn to the discussion of more exotic strongly interacting models, *i.e.* models in which, unlike the case of QCD, the theory spectrum features $m_\sigma \lesssim f_\pi$. The behavior of gauge

[1] We remind the reader that there are however choices of parameters for which the variation $\delta v/v$ is smaller than one even when $T_{\rm RH} < T_{\rm EW}$, see Fig. 5.10.

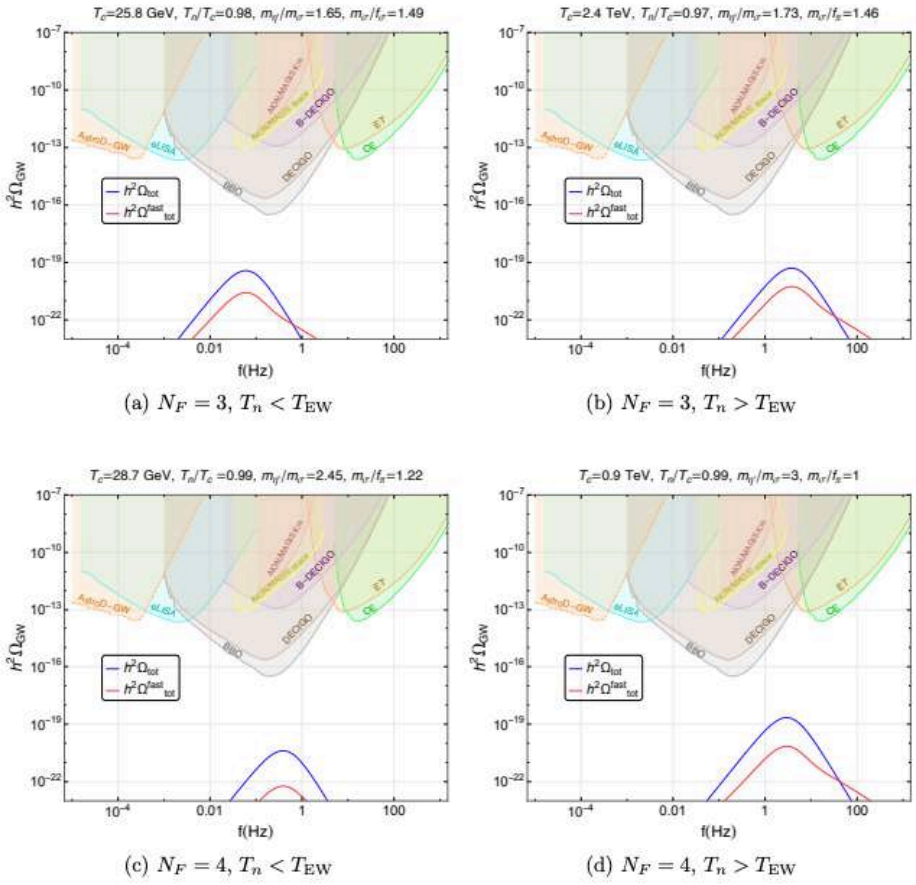

(a) $N_F = 3$, $T_n < T_{\rm EW}$ (b) $N_F = 3$, $T_n > T_{\rm EW}$

(c) $N_F = 4$, $T_n < T_{\rm EW}$ (d) $N_F = 4$, $T_n > T_{\rm EW}$

Figure 5.12: Gravitational wave spectrum for a strongly interacting sector with a QCD-like spectrum, see the definition in Sec. 5.8.1. The parameters of the benchmark points shown are collected in Tab. 5.1. We show the signal computed according to Eq. (5.34) (blue line) and to Eq. (5.41) (red line).

theories with different number of flavors has been studied on the lattice in a certain number of situations, with the surprising result that a non-QCD behavior in which the σ meson is lighter than expected might emerge. In particular, light composite σ scalars have been found in an SU(3) gauge theory with 8 flavors in the fundamental [203; 204; 205; 206], with 2 flavors in the symmetric representation [207; 208; 209] and with 4 light and 8 heavy flavors [210]. They also appear in SU(2) theories with one adjoint flavor [211]. The behavior seems to be quite generic, and is typically associated with gauge theories near to their conformal limit. In the case of $N_F = 3$ and $N_F = 4$, this is expected to happen when the number of colors is

Non QCD-like case $N_F = 3$

	$T_n < T_{\rm EW}$	$T_n > T_{\rm EW}$
m_Σ^2 [GeV^2]	1	1
λ	0.01	0.01
κ	0.1	0.1
μ_Σ [GeV]	3.5	150
f_π [GeV]	54.4	2.3×10^3
m_σ [GeV]	9.86	0.4×10^3
$m_{\eta'}$ [GeV]	16.90	0.7×10^3
m_S [GeV]	18.4	0.8×10^3
T_n [GeV]	19.9	0.8×10^3
α	0.00336	0.00348
β/H	1166.25	907.5

Non QCD-like case $N_F = 4$

	$T_n < T_{\rm EW}$	$T_n > T_{\rm EW}$
m_Σ^2 [GeV^2]	25	4.9×10^5
λ	0.3	2
κ	0.4	3
μ_Σ	1.56	10.58
f_π [GeV]	50	2.1×10^3
m_σ [GeV]	7	0.9×10^3
$m_{\eta'}$ [GeV]	62.4	7×10^3
m_S [GeV]	49.5	5.6×10^3
T_n [GeV]	9	0.9×10^3
α	0.09378	0.02136
β/H	1483.2	1828.3

Table 5.2: Values of the linear sigma model parameters, physical meson masses and relevant quantities entering the GW spectrum calculation of the $N_F = 3$ and $N_F = 4$ for the non QCD-like cases.

larger than 4 and the fermions transform in the antisymmetric representation [212].

In all the cases mentioned above, the σ meson is found to be roughly degenerate with the pions, at least in the limit of large chiral symmetry breaking. Such behavior can be captured by a sigma model, as shown in [213]. The limit of small chiral symmetry breaking is however more difficult to describe on the lattice. In the absence of conclusive data, we will suppose that the physics is correctly captured by a sigma model, at least in a first approximation. In [214] such sigma model has been extend to include the effects of the η' mass. An interesting result emerging from the analysis is that the degeneracy between m_σ and m_π can be explained by an approximate cancellation between the VEV and $m_{\eta'}$. If this happens in the chiral limit, an immediate consequence is that typically $m_\sigma \lesssim$ VEV, and thus $m_\sigma \lesssim f_\pi$. This is the situation studied in this section. Our results are shown in Fig. 5.13, where the color codes are the same as in Fig. 5.12. As we see, allowing for $m_\sigma \lesssim f_\pi$ allows to boost the GW signal amplitude, in agreement with the results of [28], where detectable GW spectra where found for large values of $m_{\eta'}/m_\sigma$. All together we find that, while in the $N_F = 3$ case also in case of non QCD-like theory the predicted GW signal lies well below the reach of future experiments, in the $N_F = 4$ case, the signal could be potentially detected both for the $T_c < T_{\rm EW}$ and $T_c > T_{\rm EW}$ cases, in the frequency range 10^{-3} Hz $-$ 1 Hz. Numerically, we have

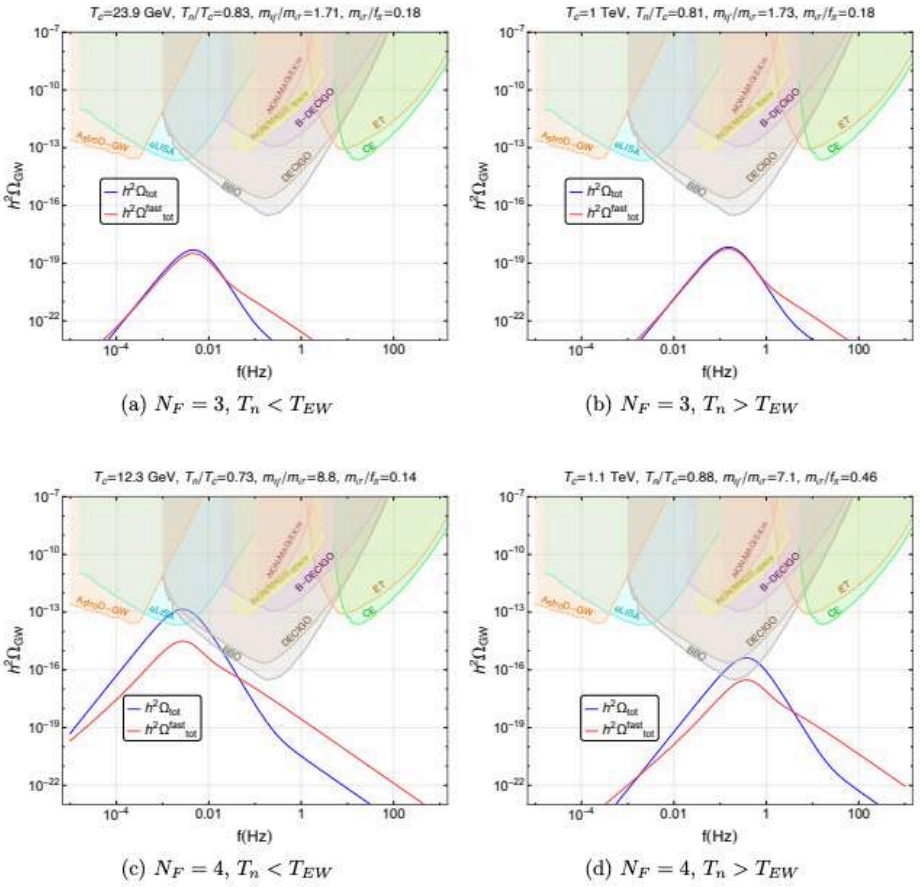

(a) $N_F = 3$, $T_n < T_{EW}$ (b) $N_F = 3$, $T_n > T_{EW}$

(c) $N_F = 4$, $T_n < T_{EW}$ (d) $N_F = 4$, $T_n > T_{EW}$

Figure 5.13: Same as in Fig. 5.12 but for the non QCD-like case defined in Sec. 5.8.2. The parameters of the benchmarks shown are collected in Tab. 5.2.

also explicitly checked that other than a large $m_{\eta'}/m_\sigma$, also the condition of a small m_σ/f_π should be satisfied in order to enhance the signal towards the reach of future experiments. If any one of these two conditions fails to be satisfied, the signal typically lies well below the region of future detectability.

Chapter 6

Conclusions

In the present dissertation we have focused on some application of EFT's in the search for BSM physics. In this context, we dealt with three main subjects. First, how BSM physics can modify the detection of relic neutrinos in a PTOLEMY-like experiment. Second, we studied the running and mixing of operators of a dark sector EFT, under the hypothesis that the operators are generated by a heavy *flavorful* mediator. Finally, the search for gravitational imprints of a candidate to solve the hierarchy problem, the relaxion.

Because the covered topics are different, we will first give the conclusions of each topic separately, and finalize with a global discussion.

First, the detection of the CνB would be a milestone for both particle physics and cosmology. Experiments using the neutrino capture by tritium are in development, so that the detection of the CνB may become a reality in the near future. In this part of the research we have studied how the capture rate is modified if new interactions involving neutrinos are present. For definitiveness, we have focused on the interactions arising from generic BSM physics, including all the dimension-six operators that can modify the process $\nu + n \to e + p$. Once the experimental limits coming from low energy processes are considered, we have seen that for Majorana neutrinos the modifications to the capture rate are modest (of $\mathcal{O}(2\%)$), while for Dirac neutrinos we can have much larger modifications, which can either increase or diminish the capture rate up to roughly a factor of two. Since in the SM case we expect the capture rate for Majorana neutrinos to be twice the one for Dirac neutrinos, we see that

the measurement of the capture rate at future experiments will not be conclusive about the Majorana or Dirac nature of neutrinos.

Another situation in which the observed neutrino capture rate can be different from the standard one is the existence of a non negligible cosmic population of right handed neutrinos. In this case the capture rate can either be left unaltered or increase (depending on the physical origin of the right handed population). This allows us to conclude that if a PTOLEMY-like experiment detects a capture rate *smaller* than the standard capture rate for Dirac neutrinos, it would unavoidably point to the presence of New Physics in the neutrino sector (since, as shown in section 3.7.4, the capture rate can be decreased in this case). If instead the measured capture rate is between the standard Dirac and Majorana case, or even above the standard Majorana case, the situation will not be clear, since the effect can be caused by Dirac neutrinos with either BSM interactions or an additional cosmological abundance of right-handed neutrinos. On the other hand, we have seen how important the right-chiral couplings are for the relic neutrino capture rate. Since the rate depends on ϵ_{Rq} when m_j/E_j is not negligible, a possible detection of the CνB can put stronger limits on the ϵ_{Rq} couplings that other low energy processes can not.

We also briefly discuss in appendix A the problem of distinguishing the electron peaks generated by neutrino capture and β-decay. With an expected resolution of $\Delta = 0.15$ eV, the PTOLEMY experiment will be able to detect only a single peak, corresponding to the capture of the three neutrino mass eigenstates. Assuming however two possible resolutions, $\Delta = 0.01$ eV (very aggressive) and $\Delta = 0.001$ eV (ultimate), we established a novel criteria to distinguish the electron peaks as a function of the separation between the experimental Gaussian distributions. The main result is that, given the range of neutrino parameters allowed by current oscillation experiments, the ability to distinguishing the peaks depends crucially on the neutrino mass ordering, and even for the ultimate value $\Delta = 0.001$ eV the three peaks could be only disentangled for normal ordering. This result agrees with previous studies in the literature [36; 215; 216].

In the second part of the thesis we considered a generic dark sector EFT, we also computed the running above and below the EW scale and the matching due to the heavy SM particles.

Our main results are shown in Fig. 4.7 and in the approximate analytic solutions of Eqs. (4.15) and (4.16). The most important effects in the running are generated by the top Yukawa coupling, and as such are present only above the top quark threshold. Once turned on at the scale Λ, the contribution of the running on the flavor-off-diagonal Wilson coefficients is irreducible, in the sense that, unlike what happens for flavor-diagonal coefficients, it does not depend on possible correlations between the Wilson coefficients at the scale Λ. From a phenomenological perspective, our results imply that the most important effect of the running and mixing is found at low energy in the currents constructed out of the left-handed down-type quarks $\bar{b}_L\gamma^\mu d_L$ and $\bar{b}_L\gamma^\mu s_L$. If the dark sector is heavier than the B mesons mass scale, then the main effects will be due to loops of dark particles. If instead the dark sector is sufficiently light, the decays $b \to s +$ invisible and $b \to d +$ invisible may be kinematically allowed and can be used to put bounds on the Wilson coefficients. Since all these processes depend on the specific nature of the dark sector particles, we defer their study to a forthcoming research.

In the third part of this thesis we have considered the framework in which the EW scale is stabilized through the *relaxation* mechanism. We have assumed that this happens during inflation and that the back-reaction potential needed to stop the relaxion evolution is generated by new vector-like fermions charged under a new strongly interacting $SU(N_d)$ gauge group. We have focused on a configuration where the reheating temperature is above the confinement scale of the new strong dynamics. This causes the restoration of a deconfined phase after inflation, the disappearance of the back-reaction potential and the presence of a second relaxation phase during the early Universe thermal evolution. This second relaxation phase can in principle completely spoil the solution of the hierarchy problem. Once the temperature of the plasma drops again below the confinement scale of the new strong dynamics, the barrier again forms and the relaxation finally stops its evolution. Crucially, the phase transition between the confined and unconfined dynamics might be strongly first order and can then produce a stochastic GW background, that can be detected at present and future interferometer experiments.

We have studied the relaxation evolution during the second relaxation phase, finding analytical solutions for its equation of motions for various ranges of temperatures. In particular

we have shown that, depending on the model parameters and on the hierarchy between the nucleation, reheating and EW phase transition temperatures, there are ample regions in parameter space where the second relaxation phase does not spoil the solution to the hierarchy problem. Such regions are large when $T_n < T_{\rm EW} < T_{\rm RH}$ and $T_{\rm EW} < T_n < T_{\rm RH}$, but are typically small or inexistent when $T_n < T_{\rm RH} < T_{\rm EW}$.

We have then studied the GW signal that can be generated during the confining phase transition that ends the second relaxation stage, considering $SU(N_d)$ gauge theories with 3 and 4 light flavors present in the spectrum. To quantitatively describe the strong dynamics we have employed a linear sigma model, considering both QCD-like spectra, in which the σ meson is heavier than the symmetry breaking scale, and non QCD-like spectra, in which the σ meson can ben lighter than it. The latter behavior may emerge in theories close to their conformal window, although additional lattice studies are needed to establish whether this is the case or not. While in the first case we find that the predicted signals lie below the present and future experimental sensitivities, in the case of non-QCD like spectra signals close and within the experimental reach can be obtained for the $N_F = 4$ case. We however observe that, even if a GW signal will be detected in the future, the reconstruction of the underlying model will in general be challenging. On the one hand, as we have shown, there is little difference in the signal shapes expected for $N_F = 3$ and $N_F = 4$ cases we have analyzed. On the other hand, many different models of strongly interacting vector-like fermions can give rise to the same relaxion back-reaction potential and can be described through the same linear sigma model studied here. We finally stress that all results obtained in this work by describing the dynamics of a strongly interacting theory through effective models suffer by large uncertainties, that can affect the peaks positions and heights of the predicted GW spectra [177]. Nevertheless we believe that is of paramount interest that BSM physics that can offer a solution to the hierarchy problem through the relaxion mechanism might generate a GW signal in the range of detectability of future experiments, and this makes even more important a thorough study of such theories through first principle calculations.

To conclude, the results obtained in this thesis show some of the possible applications of EFT techniques in the quest of BSM physics. Those techniques were implemented in various

different context, and to calculate a variety of quantities such as: the capture rate, the RG evolution of the Wilson's coefficients and the GW spectrum. Furthermore, the different models we faced were different not only on their symmetries, but also on their particle content and even in the type of experiments associated to their detection. This proves how such techniques are "universal", in the sense that they provide a unique framework able to tackle with vastly different problems that could be tested in near future experiments.

Appendix A

A.1 Standard Model: conventions

We show in this Appendix a few more details on the SM Lagrangian, as well as some useful definitions used throughout the thesis. According to the conventions shown in Table 4.1, the SM Lagrangian in the unbroken phase is given by

$$\begin{aligned}\mathcal{L} = &-\frac{1}{4}(G_{\mu\nu})^2 - \frac{1}{4}(W^a_{\mu\nu})^2 - \frac{1}{4}(B_{\mu\nu})^2 \\ &+ i\overline{\psi}\not{D}\psi + |D_\mu H|^2 - V(H) \\ &+ \overline{q}_L Y_d H d_R + \overline{q}_L Y_u \tilde{H} u_R + \overline{\ell}_L Y_e H e_R + h.c.\,,\end{aligned} \tag{A.1}$$

where as usual $\tilde{H} = i\sigma_2 H^*$. We stress that we do not commit to a fermion basis in which some of the Yukawa matrices Y_u, Y_d and Y_e are diagonal. The equation of motion of the hypercharge vector field is particularly important, since it allows to define away a redundant current. It reads

$$\begin{aligned}\partial^\nu B_{\mu\nu} = g' J^Y_\mu = g' \big(&y_{q_L}\overline{q}_L\gamma_\mu q_L + y_{u_R}\overline{u}_R\gamma_\mu u_R + \overline{d}_R\gamma_\mu d_R + y_{\ell_L}\overline{\ell}_L\gamma_\mu\ell_L \\ &y_{e_R}\overline{e}_R\gamma_\mu e_R + y_H i H^\dagger \overleftrightarrow{D}_\mu H\big)\,.\end{aligned} \tag{A.2}$$

Once the EW symmetry is broken by the Higgs vacuum expectation value (vev)

$$\langle H\rangle^T = (0, v) \qquad v \simeq 174\ \text{GeV}\,, \tag{A.3}$$

and all the states get non-vanishing masses.

Appendix B

B.1 Brief comment on the neutrino mass ordering

As we have already stressed, each neutrino mass eigenstate will produce an electron of energy given by eq. (3.52) in a PTOLEMY-like experiment. A natural question is then whether each neutrino peak can be distinguished from the β-decay background and, if so, when each peak in the distribution can be distinguished from the peaks generated by the capture of the other neutrinos [215; 216]. The answer depends crucially not only on the experimental resolution Δ, but also on the absolute value of the neutrino masses as well. In order to answer the above questions, we slightly modify eq. (3.55) to consider the number of events due to the ν_j capture as

$$\mathcal{N}^j_{\mathrm{C}\nu\mathrm{B}}(\Delta) = \int_{E_e^{\mathrm{C}\nu\mathrm{B},j}-\Delta/2}^{E_e^{\mathrm{C}\nu\mathrm{B},j}+\Delta/2} dE_e \frac{d\Gamma^{\mathrm{BSM}}_{\mathrm{C}\nu\mathrm{B}}(j)}{dE_e} \,,$$

with $E_e^{\mathrm{C}\nu\mathrm{B},j}$ given in eq. (3.52). The criteria we use to distinguish the peaks from the background and between each other are the following:

1. we say that an electron peak due to neutrino capture can be distinguished from the β-decay background if

$$r^j_{\mathrm{C}\nu\mathrm{B}} \equiv \frac{\mathcal{N}^j_{\mathrm{C}\nu\mathrm{B}}(\Delta)}{\sqrt{\mathcal{N}_\beta(\Delta)}} \geq 5; \tag{B.1}$$

2. we count the number of distinguishable peaks according to the number of different

values taken by the function

$$\Xi^{j}_{\mathrm{C}\nu\mathrm{B}} = \sum_{i=1}^{3} \left\{ 1 - \Theta \left(D_B \left(\frac{d\Gamma^{i}_{\mathrm{C}\nu\mathrm{B}}}{dE_e}, \frac{d\Gamma^{j}_{\mathrm{C}\nu\mathrm{B}}}{dE_e} \right) - 4.5 \right) \right\} \Gamma^{i}_{\mathrm{C}\nu\mathrm{B}}, \tag{B.2}$$

where $D_B(p,q)$ is the Bhattacharya distance [217], defined for two Gaussians distributions, p and q, as

$$D_B(p,q) = \frac{1}{4} \ln \left\{ \frac{1}{4} \left(\frac{\sigma_p^2}{\sigma_q^2} + \frac{\sigma_q^2}{\sigma_p^2} + 2 \right) \right\} + \frac{1}{4} \frac{(\mu_p - \mu_q)^2}{\sigma_p^2 + \sigma_q^2}. \tag{B.3}$$

The value 4.5, which measures the separation between the peaks in the Θ function of eq. (B.2), has been chosen because it corresponds to a distance of 6σ between the mean values of two Gaussians with $\sigma_p = \sigma_q$.

The function $\Xi^{j}_{\mathrm{C}\nu\mathrm{B}}$ of eq. (B.2) has been constructed as follows: when the mass eigenstates are degenerate, the Bhattacharya distance vanishes and $\Xi^{j}_{\mathrm{C}\nu\mathrm{B}}$ gives the total neutrino capture rate. Since $\Xi^{j}_{\mathrm{C}\nu\mathrm{B}}$ takes a unique value for the three neutrino states, we have that only one peak will be seen experimentally. Meanwhile, if any eigenstate is separated enough to give a distance equal or larger than 6σ, the $\Xi^{j}_{\mathrm{C}\nu\mathrm{B}}$ will correspond to the value of the capture rate for such mass eigenstate. Whether a PTOLEMY-like experiment will be able to distinguish between two or more neutrino capture peaks depends instead on the mass ordering and on the experimental resolution Δ. With the expected PTOLEMY resolution of $\Delta = 0.15$ eV, the Gaussian peaks for each electron will be too large to allow a distinction between the different contribution, so that a unique peak is expected. Nevertheless, we will try to understand how the electron peaks would look like for better experimental resolutions, which we take to be $\Delta = 0.01$ eV and $\Delta = 0.001$ eV.

We show in figure B.1 how the $\Xi^{j}_{\mathrm{C}\nu\mathrm{B}}$ function depend on the lightest neutrino mass m_0, for the mass eigenstates ν_1 (green), ν_2 (red) and ν_3 (blue). We consider both types of mass orderings and the two resolution already mentioned, $\Delta = 0.01$ eV and $\Delta = 0.001$ eV. We also scan over all the neutrino parameters at 3σ [218]. The gray points are those that can not be distinguished from the β-decay background. The upper left panel ($\Delta = 0.01$ eV, normal

ordering) should be interpreted as follows: for $m_0 \gtrsim 3 \times 10^{-2}$ eV, the $\Xi^j_{\mathrm{C}\nu\mathrm{B}}$ function takes only one value, so that only one peak would be measured, which corresponds to the capture of the three neutrinos. Since the peak is not gray, it can be distinguished from the β-decay background. For 8×10^{-3} eV $\lesssim m_0 \lesssim 3 \times 10^{-2}$ eV, two peaks could be measured, one due to the ν_3 capture (blue) and the other due to ν_1 and ν_2 (red/green). Finally, for $m_0 \lesssim 8 \times 10^{-3}$ eV, only the ν_3 peak can be resolved, while the $\nu_1 + \nu_2$ peak cannot be discriminated from the β-decay background. The other panels can be interpreted along the same reasoning. It is interesting to notice that there is only one situation in which the three peaks can be resolved, corresponding to the normal ordering for the extreme case $\Delta = 0.001$ eV. With the same resolution but inverted ordering, at most two peaks can be discriminated, since ν_1 and ν_2 tend to become degenerate as $m_3 \to 0$.

To better illustrate the interplay between the experimental resolution Δ and the importance of the neutrino mass ordering, we show in figure B.2 the expected spectra in a PTOLEMY-like experiment. In each plot we show normal (continuous line) and inverted (dashed line) ordering, for the two experimental resolutions we are discussing (a very agreessive $\Delta = 0.01$ eV, upper panels, and an ultimate $\Delta = 0.001$ eV, lower panels) and for some choices for the lightest neutrino mass. The gray line represents the β-decay background. This shows another potential problem in the peak detection; since

$$\Gamma^j_{\mathrm{C}\nu\mathrm{B}} \propto |U_{ej}|^2 \,,$$

and

$$|U_{ej}|^2 \simeq \{0.68, 0.3, 0.02\} \,,$$

the peak due to ν_3, although in principle distinguishable from the other peak(s), is much smaller, and will most probably be unresolved or unobservable in a real experiment.

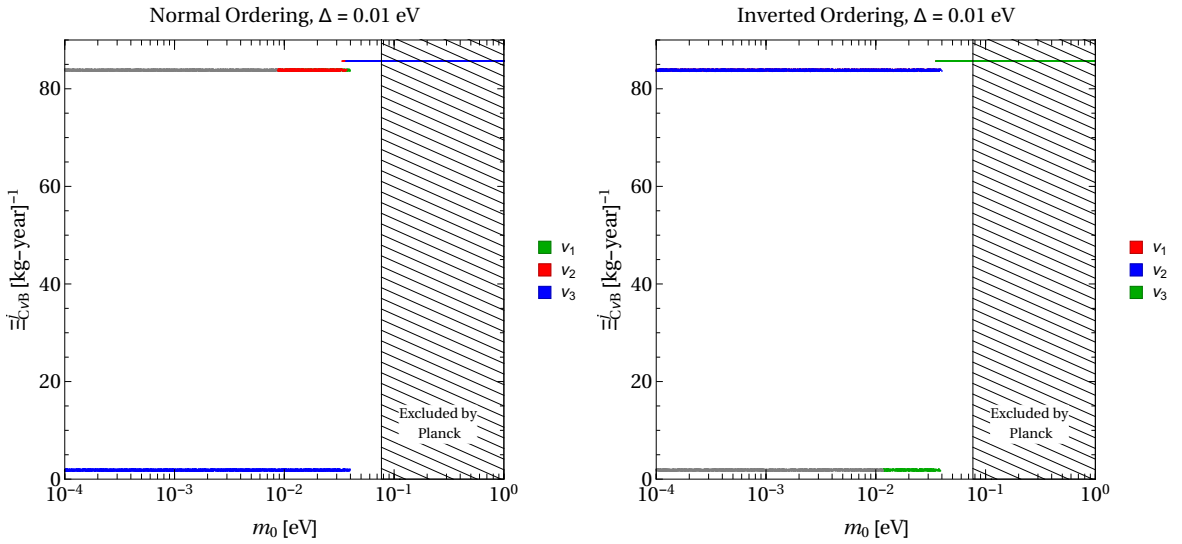

(a) $\Delta = 10^{-2}$ eV

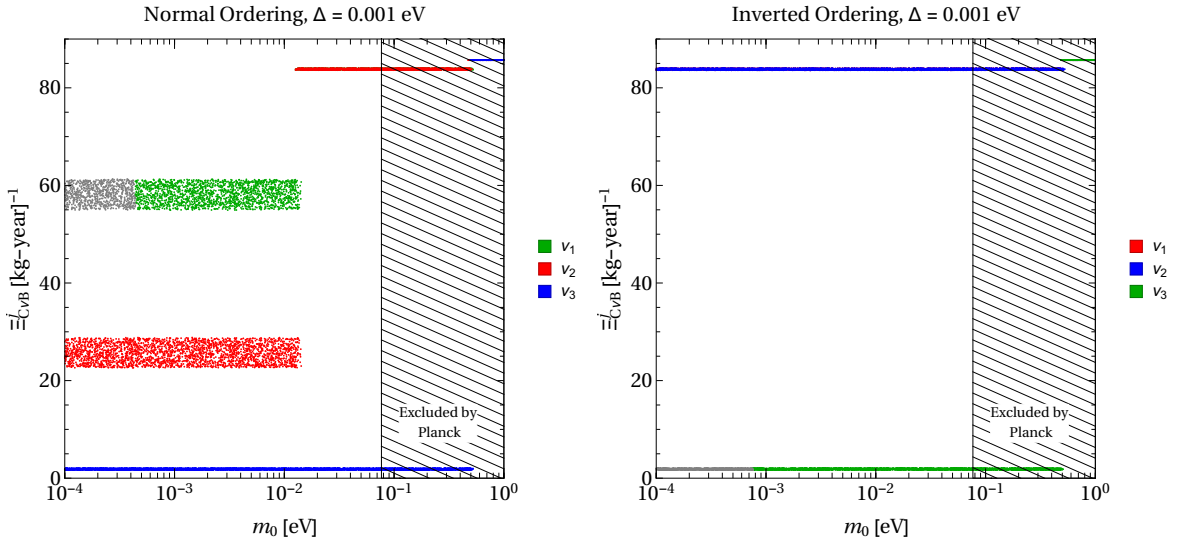

(b) $\Delta = 10^{-3}$ eV

Figure B.1: Dependence of the $\Xi^j_{\mathrm{C}\nu\mathrm{B}}$ function of eq. (B.2) on the value of the lightest neutrino mass m_0. The experimental resolution is chosen to be $\Delta = 0.01$ eV (upper panels) and $\Delta = 0.001$ eV (lower panels), and we show both normal ordering (left panels) and inverted ordering (right panels). The three neutrino mass eigenstate contributions are shown in green (ν_1), red (ν_2) and blue (ν_3). The gray points correspond to the regions that cannot be distinguished from the β-decay background. The shaded region is excluded by the Planck limit on the sum of neutrino masses [63].

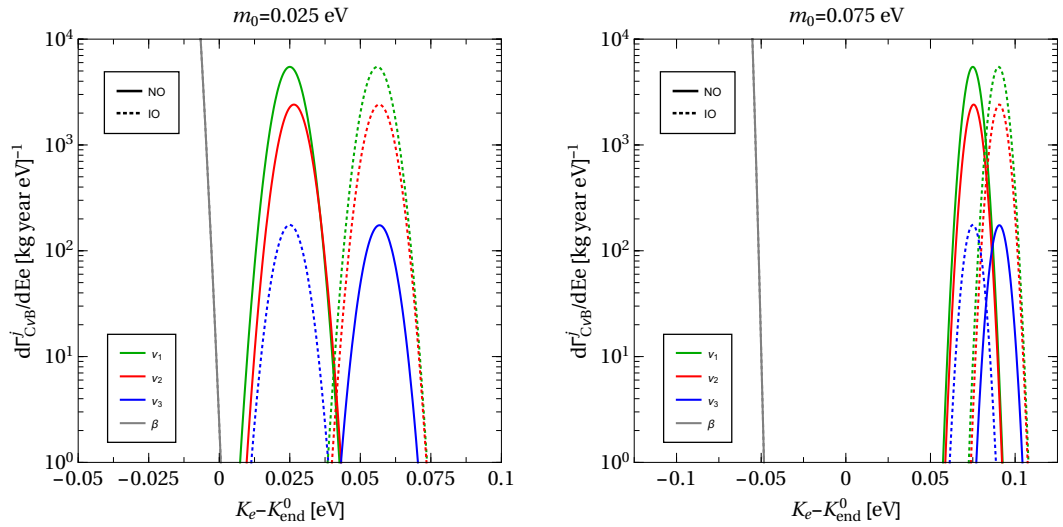

(a) $\Delta = 10^{-2}$ eV

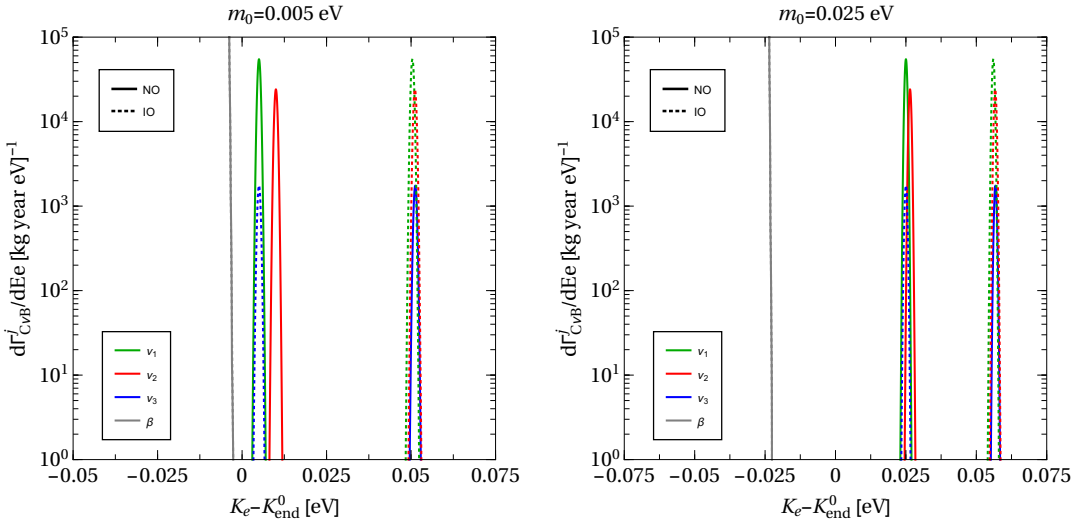

(b) $\Delta = 10^{-3}$ eV

Figure B.2: Simulated spectra of the electrons created by the relic neutrino capture for $\Delta = 0.01$ eV (upper panels) and $\Delta = 0.001$ eV (lower panels) for each mass eigenstate contribution: ν_1 (green), ν_2 (red), ν_3 (blue). A few values of the lowest neutrino mass m_0 are considered to illustrate the behavior for the normal ordering (NO) and inverted ordering (IO). The gray line corresponds to the endpoint of the β-decay background.

Appendix C

C.1 The SM lagrangian below the EW scale

After we integrate out the heavy fields in the SM Lagrangian, Eq. (A.1), results

$$\mathcal{L} = -\frac{1}{4}(G_{\mu\nu})^2 - \frac{1}{4}(F_{\mu\nu})^2 + \overline{\psi}(\not{D} - m_\psi)\psi + \mathcal{L}_{\text{Fermi}}\,, \tag{C.1}$$

where $F_{\mu\nu}$ is the photon field strength, while ψ represents any of the light Dirac fermions still present in the theory. We do not assume the existence of right handed neutrinos in the low energy spectrum, and we leave unspecified the mechanism behind their mass generation. Once the Z and W bosons are integrated out, we obtain two contributions for the four-fermion Fermi Lagrangian. The neutral current one reads

$$\mathcal{L}_{\text{F}} \supset -\frac{G_{Fff'}}{\sqrt{2}} g_{\Gamma f} g_{\Gamma' f'} (\overline{f}\Gamma^\mu f)(\overline{f'}\Gamma'_\mu f')\,, \tag{C.2}$$

where $\Gamma = \gamma^\mu$ or $\gamma^\mu\gamma_5$ as defined below Eq. (4.10). Although the notation $G_{Fff'}$ seems redundant, we keep explicit track of the 'fermion indices' because, as we will show in Appendix C.4, different f and f' correspond to different running for the coupling.

Turning to the charged current, the relevant contributions read

$$\mathcal{L}_{\text{F}} \supset -\frac{G_{Fud}}{4\sqrt{2}} \sum_{i,j,k,l} V^{ij} V^{\dagger kl} \bar{u}^i \left(\gamma^\mu - \gamma^\mu\gamma_5\right) u^l \bar{d}^k \left(\gamma_\mu - \gamma_\mu\gamma_5\right) d^j\,, \tag{C.3}$$

where V denotes the CKM matrix.

The EoM of the photon field, used to eliminate the redundant operator $\partial_\mu F^{\nu\mu}$ is

$$\partial_\mu F^{\nu\mu} = eJ^\nu_{em}\,, \tag{C.4}$$

with J_{em} the usual electromagnetic current.

C.2 EFT generated in specific models

Let us now show how some of the flavor models involving dark sectors present in the literature can be mapped to our formalism. We start with the situation considered in References [100; 219; 220], which can be summarized via the interactions

$$\mathcal{L}^A_{int} = \lambda_{ij}\overline{d}^i_R\chi^j_L\phi\,, \quad \mathcal{L}^B_{int} = \lambda_{ij}\overline{u}^i_R\chi^j_L\phi\,, \quad \mathcal{L}^C_{int} = \lambda_{ij}\overline{q}^i_L\chi^j_R\phi\,. \tag{C.5}$$

The triplet of dark fermions χ_i is chosen to be a gauge singlet, while the scalar mediator ϕ transforms under the SM gauge group as the quark to which it couples to. The same kind of interactions have been considered in Ref. [68] in the context of collider searches of Hidden Valley models. Taking the mediator to be heavy, we obtain at low energy

$$\begin{aligned}
\mathcal{L}^A_{EFT} &= \frac{\lambda_{ij}\lambda^*_{km}}{2m^2_\phi}\left(\overline{\chi}^k_L\gamma^\mu\chi^j_L\right)\left(\overline{d}^i_R\gamma_\mu d^m_R\right),\\
\mathcal{L}^B_{EFT} &= \frac{\lambda_{ij}\lambda^*_{km}}{2m^2_\phi}\left(\overline{\chi}^k_L\gamma^\mu\chi^j_L\right)\left(\overline{u}^i_R\gamma_\mu u^m_R\right),\\
\mathcal{L}^C_{EFT} &= \frac{\lambda_{ij}\lambda^*_{km}}{2m^2_\phi}\left(\overline{\chi}^k_R\gamma^\mu\chi^j_R\right)\left(\overline{q}^i_L\gamma_\mu q^m_L\right).
\end{aligned} \tag{C.6}$$

This shows that the combination of operators studied in this part of the research can be easily obtained in specific models.

C.3 Computation of the Renormalization Group Equation

In this appendix we will present more details on the computation of the RGE's for the Wilson coefficients of the $d = 3$ currents appearing in Tables 4.2 and 4.3. The final results have been

shown in Sec. 4.3, with numerical solutions given in Sec. 4.4.1. We will always use dimensional regularization in $d = 4 - 2\varepsilon$ dimensions, and use the $\overline{\text{MS}}$ scheme.

Let us start by considering loop corrections *above the EW scale*. The counterterm Lagrangian $\mathcal{L}_{c.t.}$ generated by the wave function renormalization (see Fig. 4.2) is given by

$$\begin{aligned}
\mathcal{L}_{c.t.} = & \left[\frac{g^2\,\mathcal{C}(\mathbf{2}) + g'^2\,y_H^2}{8\pi^2\varepsilon} - \frac{3\,\mathrm{tr}(Y_q^2) + \mathrm{tr}(Y_e^\dagger Y_e)}{16\pi^2\varepsilon}\right]\partial_\mu H^\dagger \partial^\mu H \\
& - \overline{q}_L\left[\frac{g_s^2\,\mathcal{C}(\mathbf{3}) + g^2\,\mathcal{C}(\mathbf{2}) + g'^2\,y_{q_L}^2}{16\pi^2\varepsilon}\mathbb{1} + \frac{Y_q^2}{32\pi^2\varepsilon}\right] i\partial\!\!\!/\, q_L \\
& - \overline{u}_R\left[\frac{g_s^2\,\mathcal{C}(\mathbf{3}) + g'^2\,y_{u_R}^2}{16\pi^2\varepsilon}\mathbb{1} + \frac{Y_u^\dagger Y_u}{16\pi^2\varepsilon}\right] i\partial\!\!\!/\, u_R - \overline{d}_R\left[\frac{g_s^2\,\mathcal{C}(\mathbf{3}) + g'^2\,y_{d_R}^2}{16\pi^2\varepsilon}\mathbb{1} + \frac{Y_d^\dagger Y_d}{16\pi^2\varepsilon}\right] i\partial\!\!\!/\, d_R \\
& - \overline{\ell}_L\left[\frac{g^2\,\mathcal{C}(\mathbf{2}) + g'^2\,y_{\ell_L}^2}{16\pi^2\varepsilon}\mathbb{1} + \frac{Y_e Y_e^\dagger}{32\pi^2\varepsilon}\right] i\partial\!\!\!/\, \ell_L - \overline{e}_R\left[\frac{g'^2\,y_{e_R}^2}{16\pi^2\varepsilon}\mathbb{1} + \frac{Y_e^\dagger Y_e}{16\pi^2\varepsilon}\right] i\partial\!\!\!/\, e_R\,,
\end{aligned} \tag{C.7}$$

where $\mathcal{C}(\mathbf{2})$ and $\mathcal{C}(\mathbf{3})$ are, respectively, the $SU(2)_L$ and $SU(3)_c$ Casimirs for the fundamental representations, y_i denotes the field hypercharge and we have used Eq. (4.5) for the definition of Y_q^2. The connection between renormalized and bare fields is now straightforwardly found:

$$\begin{aligned}
H &\simeq \left[\mathbb{1} - \frac{1}{2}\left(\frac{g^2\,\mathcal{C}(\mathbf{2}) + g'^2\,y_H^2}{8\pi^2\varepsilon} - \frac{3\,\mathrm{tr}(Y_q^2) + \mathrm{tr}(Y_e^\dagger Y_e)}{16\pi^2\varepsilon}\right)\right] H_{bare}\,, \\
q_L &\simeq \left[\mathbb{1} + \frac{1}{2}\left(\frac{g_s^2\,\mathcal{C}(\mathbf{3}) + g^2\,\mathcal{C}(\mathbf{2}) + g'^2\,y_{q_L}^2}{16\pi^2\varepsilon}\mathbb{1} + \frac{Y_q^2}{32\pi^2\varepsilon}\right)\right] q_{L,bare}\,, \\
u_R &\simeq \left[\mathbb{1} + \frac{1}{2}\left(\frac{g_s^2\,\mathcal{C}(\mathbf{3}) + g'^2\,y_{u_R}^2}{16\pi^2\varepsilon}\mathbb{1} + \frac{Y_u^\dagger Y_u}{16\pi^2\varepsilon}\right)\right] u_{R,bare}\,, \\
d_R &\simeq \left[\mathbb{1} + \frac{1}{2}\left(\frac{g_s^2\,\mathcal{C}(\mathbf{3}) + g'^2\,y_{d_R}^2}{16\pi^2\varepsilon}\mathbb{1} + \frac{Y_d^\dagger Y_d}{16\pi^2\varepsilon}\right)\right] d_{R,bare}\,, \\
\ell_L &\simeq \left[\mathbb{1} + \frac{1}{2}\left(\frac{g^2\,\mathcal{C}(\mathbf{2}) + g'^2\,y_{\ell_L}^2}{16\pi^2\varepsilon}\mathbb{1} + \frac{Y_e Y_e^\dagger}{32\pi^2\varepsilon}\right)\right] \ell_{L,bare}\,, \\
e_R &\simeq \left[\mathbb{1} + \frac{1}{2}\left(\frac{g'^2\,y_{e_R}^2}{16\pi^2\varepsilon}\mathbb{1} + \frac{Y_e^\dagger Y_e}{16\pi^2\varepsilon}\right)\right] e_{R,bare}\,.
\end{aligned} \tag{C.8}$$

Our results confirm the computation of Ref. [79]. Let us now turn to the computation of the

counterterms due to currents corrections (see Fig. 4.3). For each Wilson coefficient C_a, direct computation gives the counterterms

$$\begin{aligned}
\delta C_{q_L} =& -\frac{g_s^2\,\mathcal{C}(\mathbf{3})+g^2\,\mathcal{C}(\mathbf{3})+g'^2\,y_{q_L}^2}{16\pi^2\varepsilon}C_{q_L}-\frac{Y_uC_{u_R}Y_u^\dagger+Y_dC_{d_R}Y_d^\dagger}{32\pi^2\varepsilon}+\frac{Y_q^2}{32\pi^2\varepsilon}C_H\,,\\
\delta C_{u_R} =& -\frac{g_s^2\,\mathcal{C}(\mathbf{3})+g'^2\,y_{u_R}^2}{16\pi^2\varepsilon}C_{u_R}-\frac{Y_u^\dagger C_{q_L}Y_u}{16\pi^2\varepsilon}+\frac{Y_u^\dagger Y_u}{16\pi^2\varepsilon}C_H\,,\\
\delta C_{d_R} =& -\frac{g_s^2\,\mathcal{C}(\mathbf{3})+g'^2\,y_{d_R}^2}{16\pi^2\varepsilon}C_{d_R}-\frac{Y_d^\dagger C_{q_L}Y_d}{16\pi^2\varepsilon}+\frac{Y_d^\dagger Y_d}{16\pi^2\varepsilon}C_H\,,\\
\delta C_{\ell_L} =& -\frac{g^2\,\mathcal{C}(\mathbf{2})+g'^2\,y_{\ell_L}^2}{16\pi^2\varepsilon}C_{\ell_L}-\frac{Y_e^\dagger C_{e_R}Y_e}{32\pi^2\varepsilon}+\frac{Y_e^\dagger Y_e}{32\pi^2\varepsilon}C_H\,,\\
\delta C_{e_R} =& -\frac{g'^2\,y_{e_R}^2}{16\pi^2\varepsilon}C_{e_R}-\frac{Y_e^\dagger C_{\ell_L}Y_e}{16\pi^2\varepsilon}+\frac{Y_e^\dagger Y_e}{16\pi^2\varepsilon}C_H\,,\\
\delta C_H =& +\frac{g^2\,\mathcal{C}(\mathbf{2})+g'^2\,y_H^2}{8\pi^2\varepsilon}+\frac{3\mathrm{tr}(C_{q_L}\hat{Y}_q^2)}{16\pi^2\varepsilon}\\
&-\frac{3\left(\mathrm{tr}(Y_uC_{u_R}Y_u^\dagger)-\mathrm{tr}(Y_dC_{d_R}Y_d^\dagger)\right)}{16\pi^2\varepsilon}-\frac{\mathrm{tr}(Y_e^\dagger C_{\ell_L}Y_e)-\mathrm{tr}(Y_eC_{e_R}Y_e^\dagger)}{16\pi^2\varepsilon}\,.
\end{aligned}\tag{C.9}$$

Notice that, in addition to the counterterms of Eq. (C.9), also the redundant operator $\partial_\nu B^{\nu\mu}$ is generated via the loops of Fig. 4.4, and a further counterterm δC_B is needed. We get

$$\delta C_B=-\frac{2}{3}\frac{g'}{16\pi^2\varepsilon}T\,,\tag{C.10}$$

with T defined in Eq. (4.6). Once δC_B is added to the Lagrangian, we apply Eq. (A.2) to define away the $\partial^\nu B_{\nu\mu}$ current, obtaining that each of the counterterms in Eq. (C.9) gets a correction

$$\delta C_a\to\delta C_a-y_a\frac{2}{3}\frac{g'^2}{16\pi^2\varepsilon}T\,.\tag{C.11}$$

We are now in the position of finally compute the RGE's of the Wilson coefficients C_φ. Let us sketch the procedure. Writing $\varphi\simeq(\mathbb{1}+W_\varphi)\varphi_{bare}$ for each field (with explicit expressions given in Eq. (C.8)), the bare Wilson coefficient is given in terms of the renormalized one by

$$C_\varphi^{bare}=\mu^{\alpha\varepsilon}(\mathbb{1}+W_\varphi)(C_\varphi+\delta C_\varphi)(\mathbb{1}+W_\varphi)\simeq\mu^{\alpha\varepsilon}\left(C_\varphi+\delta C_\varphi+\frac{C_\varphi W_\varphi+W_\varphi C_\varphi}{2}\right)\,.\tag{C.12}$$

The factor $\mu^{\alpha\varepsilon}$ is inserted to ensure that all the renormalized Wilson coefficients C_φ are dimensionless in $d = 4 - 2\varepsilon$ dimensions. The coefficient α depends on the field content of the dark current $J_{\mathcal{D}}$, but we will not need to specify it as long as all the SM currents couple either to the same dark current, or to many dark currents of the same dimensions. Imposing $dC_\varphi^{bare}/d\log\mu = 0$ and using that, to leading order in the couplings, the RGE's have the form

$$\frac{dC_\varphi}{d\log\mu} = -\alpha\,\varepsilon\,C_\varphi + \dots\,, \tag{C.13}$$

we obtain the RGE's of Eq. (4.4). For the running of the Yukawa and gauge couplings we use the results in References [111; 112].

Let us now move to the EFT *below* the EW scale. The only contributions to the wave function renormalization of fermions come from QED and QCD. The counterterms are

$$\mathcal{L}_{c.t.} = -\frac{1}{16\pi^2\varepsilon}\sum_f \left(\mathcal{C}_f(\mathbf{3})g_s^2 + Q_f^2 e^2\right)\overline{f}i\partial\!\!\!/ f\,, \tag{C.14}$$

where $\mathcal{C}_f(\mathbf{3})$ is the $SU(3)_c$ quadratic Casimir, if the fermion has color, and Q_f is the fermion electric charge. Notice that there is no flavor off-diagonal contribution. Turning to vertex corrections, we now have contribution from gauge bosons and from four fermion interactions

(see Fig. 4.5). The vertex counterterms are

$$
\begin{aligned}
\delta C_{V_u} &= \frac{1}{16\pi^2\epsilon}\left[\left(\mathcal{C}_2(3)g_s^2+Q_u^2e^2\right)C_{V_u}-\frac{g_{V_u}\mathcal{F}_u}{2}-\frac{G_{Fud}}{2}V\left(\mathcal{M}_{V_d}^2-\mathcal{M}_{A_d}^2\right)V^\dagger\right],\\
\delta C_{V_d} &= \frac{1}{16\pi^2\epsilon}\left[\left(\mathcal{C}_2(3)g_s^2+Q_d^2e^2\right)C_{V_d}-\frac{g_{V_d}\mathcal{F}_d}{2}-\frac{G_{Fdu}}{2}V^\dagger\left(\mathcal{M}_{V_u}^2-\mathcal{M}_{A_u}^2\right)V\right],\\
\delta C_{V_\nu} &= \frac{1}{16\pi^2\epsilon}\left[-\frac{g_{V_\nu}\mathcal{F}_\nu}{2}-\frac{G_{F\nu e}}{2}(\mathcal{M}_{V_e}^2-\mathcal{M}_{A_e}^2)\right],\\
\delta C_{V_e} &= \frac{1}{16\pi^2\epsilon}\left[Q_e^2e^2C_{V_e}-\frac{g_{V_e}\mathcal{F}_e}{2}\right],\\
\delta C_{A_u} &= \frac{1}{16\pi^2\epsilon}\left[\left(\mathcal{C}_2(3)g_s^2+Q_u^2e^2\right)C_{A_u}-\frac{g_{A_u}\mathcal{F}_u}{2}+\frac{G_{Fud}}{2}V\left(\mathcal{M}_{V_d}^2-\mathcal{M}_{A_d}^2\right)V^\dagger\right],\\
\delta C_{A_d} &= \frac{1}{16\pi^2\epsilon}\left[\left(\mathcal{C}_2(3)g_s^2+Q_d^2e^2\right)C_{A_d}-\frac{g_{A_d}\mathcal{F}_d}{2}+\frac{G_{Fdu}}{2}V^\dagger\left(\mathcal{M}_{V_u}^2-\mathcal{M}_{A_u}^2\right)V\right],\\
\delta C_{A_\nu} &= \frac{1}{16\pi^2\epsilon}\left[-\frac{g_{A_\nu}\mathcal{F}_\nu}{2}+\frac{G_{F\nu e}}{2}(\mathcal{M}_{V_e}^2-\mathcal{M}_{A_e}^2)\right],\\
\delta C_{A_e} &= \frac{1}{16\pi^2\epsilon}\left[Q_e^2e^2C_{A_e}-\frac{g_{A_e}\mathcal{F}_e}{2}\right],
\end{aligned}
\tag{C.15}
$$

where we have used the definition of Eq. (4.10). As before, the redundant current $\partial_\nu F^{\nu\mu}$ is radiatively generated, and the corresponding counterterm results

$$
\delta C_\gamma = \frac{e}{12\pi^2\varepsilon}\left(3Q_u\mathrm{tr}[C_{V_u}]+3Q_d\mathrm{tr}[C_{V_d}]+Q_e\mathrm{tr}[C_{V_e}]\right). \tag{C.16}
$$

This effect can be incorporated in the other Wilson coefficients via the shift

$$
C_{V_a}\to C_{V_a}+Q_a\mathcal{Q}\,. \tag{C.17}
$$

Repeating now the procedure sketched in Eqs. (C.12) and (C.13) we obtain the RGE's presented in Eq. (4.8).

C.4 Running of G_F due to QCD and QED

Let us now discuss the running of the Fermi coupling below the EW scale. In addition to the wave function renormalization, we need to consider the diagrams shown in Fig. C.1. The

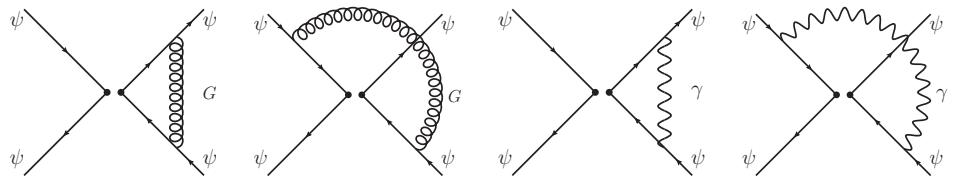

Figure C.1: Feynman diagrams contributing to the running of the Fermi coupling below the EW scale.

results are independent on the flavor of the external fermions. Some of the vertex corrections will cancel against the wave function contributions (more specifically, those vertex corrections in which the gluon or photon connect particles in the same fermion line). The gluon 'crossed' contributions [1] generate the operators

$$\overline{q}\Gamma^{\mu}T^{a}q\overline{q'}\Gamma'_{\mu}T^{a}q' \tag{C.18}$$

with a double insertion of Gell Mann matrices. These operators do not enter in the running of our currents, and we will therefore not consider them in the following. Notice however that their effect is important when the nature of the dark current is specified and dark fermions loops can be considered, as in Refs. [82; 103]. We are thus left with the photon 'crossed' loops, which are the only radiative effects that we need to take into account. Their effect is to produce the RGE

$$\frac{dG_{Fff'}}{d\log\mu} = -2G_{Fff'}\frac{Q_f Q_{f'}\alpha}{\pi}, \tag{C.19}$$

which has been used in the numerical computations of Sec. 4.4.1. Notice that the resulting RGE is independent on Γ^{μ} and Γ'^{μ}. Quantitatively, the relative variation in the value of $G_{Fff'}$ is of order of a few percent.

[1] With 'crossed' contributions we mean those loops in which the photon or gluon connect particles in two different fermion lines.

Appendix D

D.1 Bubble Nucleation: The Thin-Wall approximation

This approximation was first proposed by S. Coleman in Ref.[172] and then extended to finite temperature field theory by Linde in Ref.[171]. It is valid when the barrier height present in the FOPT, see Fig.5.8, is higher than ΔV. In order to gain a physical idea of the situation let us explore the implications. During the formation of bubbles the energy deposited in the volume $\sim (\Delta V) r^3$ becomes larger than the one deposited in the surface $\sim r^2$ [171]. This implies that $(\Delta V) r \gg 1$, and because ΔV is small, the bubble radius must be large. It also means that the bubble radius is larger than the wall thickness[1]. Therefore, in this limit the EoM Eq.(5.22) is simplified to

$$\frac{d^2\Phi}{dr^2} = V'_{\rm eff}(\Phi, T) \implies \frac{d\Phi}{dr} = \sqrt{2\, V_{\rm eff}(\Phi, T)}. \tag{D.1}$$

Now, the action defined in Eq.(5.15) can be separated in the following manner

$$S_3 = 4\pi \int_0^{r_{\rm wall}-\delta/2} dr\, r^2 \left\{ \frac{1}{2} \left(\frac{d\Phi}{dr} \right)^2 + V(\Phi, T) \right\} + 4\pi \int_{r_{\rm wall}-\delta/2}^{r_{\rm wall}+\delta/2} dr\, r^2 \left\{ \frac{1}{2} \left(\frac{d\Phi}{dr} \right)^2 + V(\Phi, T) \right\}.$$

where we already neglected the term $4\pi \int_{r_{\rm wall}+\delta}^{\infty} dr\, r^2 \left\{ \frac{1}{2} \left(\frac{d\Phi}{dr} \right)^2 + V(\Phi, T) \right\} = 0$, and δ is the bubble thickness, see Fig.5.9.

After integrating by parts and considering that the bubble thickness is small ($\delta \approx 0$), we

[1] The wall thickness is the region where $d\Phi/dr$ is large.

get

$$S_3 = -\frac{4}{3}\pi r_{\rm wall}^3\,\Delta V + 4\pi r_{\rm wall}^2 S_1, \tag{D.2}$$

where $S_1 = \int_0^\infty dr\,\left\{\frac{1}{2}\left(\frac{d\Phi}{dr}\right)^2 + V(\Phi,T)\right\}$ is identified as the one dimensional Euclidean action. S_3 is now a function of $r_{\rm wall}$ which can determined from

$$\frac{d\,S_3}{d\,r_{\rm wall}} = 0 \Longrightarrow r_{\rm wall} = \frac{2\,S_1}{\Delta V}. \tag{D.3}$$

Replacing Eq.(D.3) into Eq.(D.2), the three dimensional Euclidean action becomes

$$S_3 = \frac{16\,\pi\,S_1^3}{3\,\Delta V}. \tag{D.4}$$

As commented above S_1 is the one dimensional Euclidean action, and under the condition given in Eq.(D.1), S_1 is now given by

$$S_1 = \int_0^{\Phi_{\rm true}} d\Phi\,\sqrt{2\,V(\Phi,T)}. \tag{D.5}$$

Eqs.(D.3), (D.4) and (D.5) are the main results of this section. Nevertheless, the thin-wall approximation says nothing about an explicit form of the bounce, at most it gives Eq.(D.1). In order to obtain a concrete and useful result for a straightforward application, we study the following arbitrary potential that has the important terms for a FOPT:

$$V(\Phi,T) = \frac{1}{2}\,M^2(T)\,\Phi^2 - \frac{1}{3}\,\xi(T)\,\Phi^3 + \frac{1}{4}\,\lambda\,\Phi^4 \tag{D.6}$$

It is worthwhile to mention that the quadratic and quartic terms are present in the effective potential of the models we consider in Section 5.6. The cubic term is different: while it is already present at tree-level for $N_f = 3$, it is generated by the thermal corrections of the effective potential for $N_f = 4$. Therefore, the generic potential given in Eq.(D.6) has all the terms important for us.

Because within this approximation $\Delta V \approx 0$, we conclude that $V(0,T) \approx V(\Phi_{\rm true},T)$.

From the minimization condition $dV/d\Phi|_{\Phi_{\rm true}} = 0$ we have an extra constraint on $\Phi_{\rm true}$. Combining these two results we obtain

$$\Phi_{\rm true} = \frac{2}{3}\frac{\xi}{\lambda}, \tag{D.7}$$

$$2\,\xi^2 = 9\,M^2\,\lambda, \tag{D.8}$$

where Eq.(D.8) is obtained after evaluating $\Phi_{\rm true}$ in any of the two previous constraints on $V(\Phi, T)$. By combining Eqs.(D.7) and (D.8), with Eq.(D.6) the potential can be rewritten as

$$V(\Phi, T) = \frac{1}{4}\,\lambda\,\Phi^2\,(\Phi_{\rm true} - \Phi)^2. \tag{D.9}$$

Now we are able to compute explicitly Eq.(D.5)

$$S_1 = \sqrt{\frac{\lambda}{2}}\int_0^{\Phi_{\rm true}} d\Phi\;\Phi\;(\Phi_{\rm true} - \Phi)\,, \tag{D.10}$$

obtaining a closed expression for S_1:

$$S_1 = \sqrt{\frac{\lambda}{2}}\frac{\Phi_{\rm true}^3}{6} = \frac{4\,\xi^3}{3^4\,\sqrt{2}\,\lambda^{5/2}}. \tag{D.11}$$

Applying this result to Eqs.(D.3) and (D.4), S_3/T and $r_{\rm wall}$ are easily computed:

$$\frac{S_3}{T} = \frac{2^{17/2}\,\pi\,\xi^9}{3^{13}\,\lambda^{15/2}\,(\Delta V)\,T} \tag{D.12}$$

$$r_{\rm wall} = \frac{2^{5/2}\,\xi^3}{3^4\,\lambda^{5/2}\,(\Delta V)}. \tag{D.13}$$

Finally, we explicitly compute an analytical form for the bounce. This is done by solving

Eq.(D.1)

$$\begin{aligned} \int_r^R d\,r &= \sqrt{\frac{\lambda}{2}} \int_{\Phi(r)}^{\Phi(R)} \frac{d\,\Phi}{\Phi\ (\Phi_{\rm true} - \Phi)} \\ \Longrightarrow \frac{\left(\frac{\Phi_{\rm true}-\Phi(R)}{\Phi(R)}\right)}{\left(\frac{\Phi_{\rm true}-\Phi(r)}{\Phi(r)}\right)} &= \frac{\exp\left(-R\frac{\sqrt{\lambda}\,\Phi_{\rm true}}{\sqrt{2}}\right)}{\exp\left(-r\frac{\sqrt{\lambda}\,\Phi_{\rm true}}{\sqrt{2}}\right)}. \end{aligned}$$

The latter expression implies that $\frac{\Phi_{\rm true}-\Phi(r)}{\Phi(r)} = c_0\ \exp\left(-r\frac{\sqrt{\lambda}\,\Phi_{\rm true}}{\sqrt{2}}\right)$, where c_0 is a constant. Hence, we get for $\Phi(r)$

$$\Phi(r) = \frac{\Phi_{\rm true}}{1 + c_0\ \exp\left(-r\frac{\sqrt{\lambda}\,\Phi_{\rm true}}{\sqrt{2}}\right)}. \tag{D.14}$$

Finally, the unknown constant c_0 is determined by the condition that a typical bounce profile changes its concavity at $r_{\rm wall}$. This means

$$\left.\frac{d^2\Phi(r)}{d\,r^2}\right|_{r_{\rm wall}} = 0. \tag{D.15}$$

The latter condition fixes $c_0 = \exp\left(r_{\rm wall}\frac{\sqrt{\lambda}\,\Phi_{\rm true}}{\sqrt{2}}\right)$. In this way, we have been able to determine an analytical form for the bounce, which is

$$\begin{aligned} \Phi_{\rm bounce}(r) &= \frac{\Phi_{\rm true}}{1 + \exp\left((r_{\rm wall} - r)\frac{\sqrt{\lambda}\,\Phi_{\rm true}}{\sqrt{2}}\right)} \\ &= \frac{\Phi_{\rm true}}{1 + \exp\left((r_{\rm wall} - r)\frac{\sqrt{2}\,\xi}{3\sqrt{\lambda}}\right)} \end{aligned} \tag{D.16}$$

In summary, given an effective potential of the form of Eq.(D.6), analytical expressions for S_3/T, $r_{\rm wall}$ and $\Phi_{\rm bounce}$ are determined in the thin-wall approximation. These expressions are Eqs.(D.12), (D.13) and (D.16), respectively.

Appendix E

E.1 Strongly interacting models for the relaxation of the EW scale

We collect in this Appendix some useful formulas regarding strongly interacting vector-fermion models and their vacuum energy. We start with some general results, and then specialize them to the models used in the relaxion framework.

E.1.1 General setup

Consider N_F vector-like fermions Ψ charged under a new confining group, which for simplicity we take to be $SU(N_d)$. We will assume a situation similar to what happens in QCD, namely that there is a small explicit breaking of the chiral symmetry $SU(N_F)_L \times SU(N_F)_R$ due to non vanishing fermion masses. Moreover, we take the axial part of the global flavor group to be anomalous. The Lagrangian we consider is

$$\mathcal{L} = i\bar{\Psi}\partial\!\!\!/\Psi - \overline{\Psi}_L \mathcal{M} \Psi_R + \frac{\theta_0}{32\pi^2} D_{\mu\nu} D^{\tilde{\mu\nu}} + h.c. \,, \tag{E.1}$$

where $\mathcal{M}$ is the $n \times n$ mass matrix of the vector-like fermions Ψ and $D_{\mu\nu}$ is the field strength tensor of the $SU(N_d)$ gauge group, with $\tilde{D}_{\mu\nu}$ its dual. Using a $SU(N_F)_L \times SU(N_F)_R$ trans-

formation [1] the mass matrix can always be put in the form

$$\mathcal{M} \to e^{i\varphi_M/N_F}\mathrm{diag}(M_1,\ldots,M_{N_F}) \equiv e^{i\varphi_M/N_F}\mathcal{M}_D \ , \tag{E.2}$$

where $\varphi_M = \arg\det\mathcal{M}$ and $M_i \geq 0$. We use this basis in the following. We can write the low energy theory by using the following transformations and spurions under an axial transformation

$$\Psi_{L,R} \to e^{\mp i\alpha}\Psi_{L,R} \ , \quad M \to e^{-2i\alpha}M \ , \quad \theta_0 \to \theta_0 - 2\,N_F\,\alpha \ . \tag{E.3}$$

We collect the low energy degrees of freedom in a matrix

$$\Sigma = \text{“}\overline{\Psi}_L\Psi''_R = \left(\frac{v+\sigma}{\sqrt{2N_F}} + S^aT^a\right)\mathcal{U} \ , \tag{E.4}$$

where σ is the radial degree of freedom, T^a are the $SU(N)$ generator, S^a are CP-even scalars and $\mathcal{U}$ is the matrix of the NBGs, including the dark η'. Notice that we denote the VEV with v, as opposed to the EW VEV, which has been called $v_{\rm EW}$. We write $\mathcal{U}$ explicitly as

$$\mathcal{U} = \exp\left[i\left(\frac{\eta'}{v} + \frac{\pi^aT^a}{v/\sqrt{2N_F}}\right)\right] \ . \tag{E.5}$$

Following [214] we define the pion decay constant in a theory with N_F flavors as

$$f_\pi = \sqrt{\frac{2}{N_F}}v \ . \tag{E.6}$$

The most general potential invariant under $SU(N_F)_L \times SU(N_F)_R \times U(1)_V \times U(1)_A$ is given by

$$V = -m_\Sigma^2\langle\Sigma^\dagger\Sigma\rangle + \frac{\lambda}{2}\langle\Sigma^\dagger\Sigma\rangle^2 + \frac{\kappa}{2}\langle(\Sigma^\dagger\Sigma)^2\rangle - B\,\langle\mathcal{M}\Sigma\rangle + \mu_\Sigma\,e^{-i\theta}\det\Sigma + h.c. \tag{E.7}$$

[1] Note that the phases can be factorized using a transformation generated by the diagonal elements of the two groups.

where $\langle\cdot\rangle$ denotes the trace and we have used an axial transformation to put the phase dependence in the anomaly term, $\theta = \theta_0 + \varphi_M$.

Let us start with the computation of the vacuum energy, since it is essential to write the relaxion potential in Eq. (5.3). In doing this we ignore the heavy degrees of freedom σ and S^a in Eq. (E.7). Using the results of [221], working in the basis in which the fermion mass matrix is diagonal forces the Σ matrix in the vacuum to be diagonal. We write it as

$$\Sigma_0 \equiv \langle\Sigma\rangle = \frac{v}{\sqrt{2N_F}}\text{diag}(e^{i\theta_1}, \ldots, e^{i\theta_{N_F}}) \ , \tag{E.8}$$

which gives a vacuum energy

$$E(\theta) = -\tilde{B}\sum_{i=1}^{N_F} M_i \cos\theta_i + \tilde{\mu}_\Sigma \cos\left(\sum_{k=1}^{N_F}\theta_k - \theta\right) \ . \tag{E.9}$$

In the previous equation we have used $\tilde{B} = Bv\sqrt{2/N_F}$ and $\tilde{\mu}_\Sigma = 2\mu_\Sigma(v/\sqrt{2N_F})^{N_F}$. The Dashen equations give the minimum conditions

$$\tilde{B}\, M_i \sin\theta_i = -\tilde{\mu}_\Sigma \sin\left(\sum_k \theta_k - \theta\right) \ , \quad i = 1, \ldots, N_F \ . \tag{E.10}$$

We can find approximate solutions to the Dashen equations when the anomaly term dominates over the mass term, which is equivalent to assume that the mass of the η' is larger than the masses of the mesons. In this limit we have

$$\sin\left(\sum_k \theta_k - \theta\right) \simeq 0 \ , \quad \Rightarrow \quad \theta \simeq \sum_k \theta_k \ . \tag{E.11}$$

The remaining Dashen equations can now be written as

$$M_i \sin\theta_i = M_k \sin\theta_k \ , \quad i \neq k \ . \tag{E.12}$$

In the case in which all the fermion masses are approximately of the same order the previous equation is solved by $\theta_i \simeq \theta_k \simeq \theta/N_F$. This means that in the limit considered,

i.e. dominance of the anomaly term over the mass term and approximate degeneracy of the fermion masses, the vacuum matrix is given by

$$\Sigma_0 \simeq \frac{v\, e^{i\theta/N_F}}{\sqrt{2N_F}} 1 \ . \tag{E.13}$$

If instead a hierarchy is present among the fermion masses the situation drastically changes. For definitiveness, let us consider the hierarchy $M_1 \ll M_i$, $i = 2, \ldots, N_F$ when the anomaly term dominates. Eq. (E.12) is now approximately solved by $\theta_1 \simeq \theta$ and $\theta_i \simeq 0$ for $i = 2, \ldots, N_F$. The conclusion is that, when a clear hierarchy is present among the fermion masses, only the lightest fermions contribute significantly to the vacuum energy. As last step, we remind that the inclusion of the relaxion field can be achieved simply promoting θ to a dynamical parameter,

$$\theta \to \phi(x)/F \ . \tag{E.14}$$

We now move on with the discussion of the potential of the σ particle, since it drives the phase transition discussed in Sec. 5.8. Having discussed the effect of the VEV of the light modes in the computation of the vacuum energy, see Eq. (E.9), we now simply focus on the potential driven by σ. To write the full potential we implement thermal effects using the Truncated Full Dressing (TFD) procedure [222]

$$V_{\text{eff}}(\sigma, T) = V(\sigma) + \sum_i \frac{T^4}{2\pi^2}\, n_i\, J_B\left(\frac{M_i^2(\sigma, T)}{T^2}\right) \ . \tag{E.15}$$

The first term, $V(\sigma)$, is the tree level potential as a function of the homogenous background field σ, and can be obtained from Eq. (E.7). Following refs. [28; 223] we consider the Coleman-Weinberg contribution already included in the tree level term, since its inclusion just renormalizes the tree-level couplings. Each thermal contribution depends on the multiplicity n_i, on the bosonic thermal integral

$$J_B(x) = \int_0^\infty dy\, y^2 \log\left(1 - e^{-\sqrt{x+y^2}}\right) \ , \tag{E.16}$$

and on the thermal masses $M_i(\sigma, T)$. In a sigma model with N_F flavors they read

$$\begin{aligned}
M_\sigma^2(\sigma,T) &= -m_\Sigma^2 + \frac{3}{2}\left(\lambda + \frac{\kappa}{N_F}\right)\sigma^2 - \mu_\Sigma(N_F-1)\left(\frac{\sigma}{\sqrt{2N_F}}\right)^{N_F-2} + \Pi(N_F) \\
M_{\eta'}^2(\sigma,T) &= -m_\Sigma^2 + \frac{1}{2}\left(\lambda + \frac{\kappa}{N_F}\right)\sigma^2 + \mu_\Sigma(N_F-1)\left(\frac{\sigma}{\sqrt{2N_F}}\right)^{N_F-2} + \Pi(N_F) \\
M_{S^a}^2(\sigma,T) &= -m_\Sigma^2 + \frac{1}{2}\left(\lambda + \frac{3\,\kappa}{N_F}\right)\sigma^2 + \mu_\Sigma\left(\frac{\sigma}{\sqrt{2N_F}}\right)^{N_F-2} + \Pi(N_F) \\
M_{\pi^a}^2(\sigma,T) &= -m_\Sigma^2 + \frac{1}{2}\left(\lambda + \frac{\kappa}{N_F}\right)\sigma^2 - \mu_\Sigma\left(\frac{\sigma}{\sqrt{2N_F}}\right)^{N_F-2} + \Pi(N_F)\ ,
\end{aligned} \tag{E.17}$$

The terms proportional to μ_Σ are present only for $N_F \geq 3$. We have already included the "Debye" masses $\Pi(N_F)$ computed at one loop, the so called "hard thermal loop" [222]. In a theory with N_F flavor we obtain

$$\Pi(N_F) = \frac{T^2}{12}\left((N_F^2+1)\lambda + 2N_F\,\kappa\right)\ . \tag{E.18}$$

E.1.2 Explicit models

In the original paper [72] the back-reaction barrier is generated by the so-called $L+N$ model. This is a theory in which vector-like fermions charged under a new confining group are introduced. These fermions have EW quantum numbers to allow for Yukawa interactions with the Higgs boson. More specifically, the model consists in a vector-like pair L, L^c (where L has the same quantum numbers as the SM lepton doublet and L^c has conjugated charges) and by a second vector-like pair N, N^c of SM singlets. This is only one of the possibilities since, as we are now going to show, all models that allow for a Yukawa interaction with the Higgs doublet and in which there is a clear mass hierarchy can generate the required back-reaction. Before starting, let us remind the reader that in light of the Pisarski-Wilczek argument [150] already mentioned in Sec. 5.8, we require the presence of at least 3 light flavors below the confinement scale to produce a strong first order phase transition.

The most general Lagrangian we consider is

$$\mathcal{L} = -\psi^c \mathcal{M}_\psi \psi - \chi^c \mathcal{M}_\chi \chi - H\psi^c \mathcal{Y} N\chi^c - H^\dagger \chi^c \mathcal{Y}'\psi + h.c. \tag{E.19}$$

where the quantum numbers of the vector-like fermions are such that it is possible to write the Yukawa interactions. Moreover, $\mathcal{M}_L$, $\mathcal{M}_N$, $\mathcal{Y}$ and $\mathcal{Y}'$ are matrices whose dimensions depend on the number of fermions. Suppose now there is a hierarchy $\mathcal{M}_\chi \ll \mathcal{M}_\psi$. Integrating out the heavy fermions we obtain the effective Lagrangian

$$\mathcal{L}_{eff} = \chi^c \left(\mathcal{M}_\chi - \mathcal{Y}' \frac{1}{\mathcal{M}_\psi} \mathcal{Y} H^\dagger H \right) \chi + h.c. \tag{E.20}$$

As explained in Sec. E.1.1, the computation of the vacuum energy can be done analytically when all the fermions are approximately degenerate or when there is a clear mass hierarchy, in which case only the lightest fermions contribute. This allows us to conclude that the heavy ψ states do not substantially contribute to the vacuum energy even if their masses happen to be below the confinement scale. The problem thus is to compute the eigenvalues of the χ mass matrix. To write approximate analytical formulas we take all mass matrices to be proportional to the identity, $\mathcal{M}_\chi = m_\chi 1$ and $\mathcal{M}_\psi = m_\psi 1$ and all Yukawa matrices to be real with equal entries, $\mathcal{Y}^{(\prime)}_{ij} = y^{(\prime)}$. In this limit the vacuum energy is equal to

$$E(\phi) \simeq -\tilde{B} \left| m_\chi - \frac{n_\psi n_\chi y y'}{m_\psi} H^\dagger H \right| \cos\left(\frac{\phi}{F}\right) \ , \tag{E.21}$$

where n_χ and n_ψ are the number of χ and ψ fermions. This equation justifies the form of the back-reaction used in Eq. (5.42). Experimental limits on the $L+N$ model have been studied in [169] for the situation in which only the N flavor confines, and in [200; 201] for the situation in which both L and N confine. Although relevant, none of these bounds put significant restrictions on the parameters of the linear sigma model used in the computation of the GW spectra.

Let us comment on two further points before concluding this section. There is a caveat to the above argument: when the fermions that form bound states carry EW quantum numbers, loop contributions to the effective Lagrangians can be important, see *e.g.* [200]. We have assumed so far that such loops are negligible, but this is not necessarily the case. When loops are important the argument leading to Eq. (E.8) fails, and the computation of the vacuum energy can in general be done only numerically. Finally, let us give some

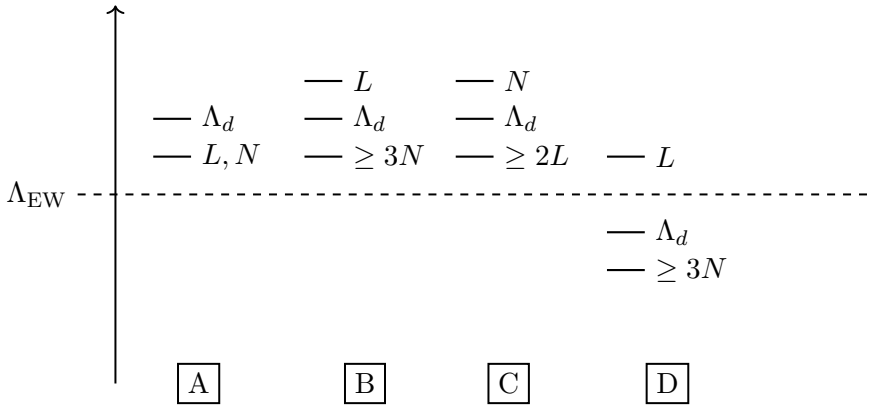

Figure E.1: Summary of the models that can generate the back-reaction for the relaxion mechanism to work and, at the same time, satisfy the Pisarski-Wilczek condition. We show only variations of the $L + N$ model defined in Sec. E.1.2, although more general possibilities are possible.

concrete example of models that can lead to strong first order phase transition. Focussing for simplicity only on variations of the original $L + N$ model used in Ref. [72], we summarize the different possibilities in Fig. 5.1.

Appendix F

F.1 Successful relaxation of the EW scale with strongly interacting fermions

We now describe in more detail how the conditions listed in Sec. 5.6 are obtained. To keep the discussion generic, we will use the form of the back-reaction potential shown in Eq. (5.42). Minimizing the potential in Eq. (5.3) we obtain

$$\frac{\partial V}{\partial H} = 0 \Rightarrow \qquad v^2(\theta) = -\frac{\Lambda^2 - \epsilon\Lambda F\,\theta - \mathcal{S}\,\mu_B^2\cos\theta}{2\lambda}\,, \tag{F.1}$$

$$\frac{\partial V}{\partial \phi} = 0 \Rightarrow \qquad r\epsilon\Lambda^3 F = \left(\mathcal{S}\mu_B^2\sin\theta - \epsilon\Lambda F\right) v^2(\theta) - \mathcal{S}\Lambda_0^4\,\sin\theta \tag{F.2}$$

where we have defined the dimensionless field $\theta = \phi/F$, $v^2(\theta)$ is the θ-dependent Higgs minimum, and $\mathcal{S} = \text{sign}[\mu_B^2 v^2(\theta) - \Lambda_0^4]$. As usual, the first equation applies when $v^2(\theta)$ is a positive quantity, otherwise the Higgs VEV vanishes. From the minimum equations we see that for small θ we have $v^2(\theta) = 0$, and $\mathcal{S} = -1$. From the equations of motion it follows that $\partial V/\partial\phi = 0$ corresponds to the stopping of the relaxion evolution. To avoid this, we need to make sure that the minimum equation has no solution while $v^2(\theta) = 0$. This amounts to require

$$r\epsilon\Lambda^3 F > \Lambda_0^4\,, \tag{F.3}$$

which corresponds to Eq. (5.43). As time passes and θ increases, the system reaches a critical value for the relaxion field in which $\epsilon\Lambda F\theta_c - \mu_B^2\cos\theta_c = 2\lambda\Lambda^2$ and EWSB is triggered.

From Eq. (F.1) we see that $v^2(\theta)$ starts growing essentially linearly with θ. Looking at Eq. (F.2), and keeping into account Eq. (F.3), we conclude that the right hand side must grow to guarantee the existence of a solution after EWSB. This can happen only if the factor multiplying $v^2(\theta)$ is positive. This requirement amounts to $\mathcal{S} = +1$ (at least around the EW scale), *i.e.* $\mu_B^2 v_{EW}^2 > \Lambda_0^4$, and to $\mu_B^2 > \epsilon\Lambda F$, which are Eq. (5.44).

We now discuss the computation of the EW scale in terms of the parameters of the model. Once the EW minimum is reached for a value θ_0 of the relaxion field we must have

$$\begin{aligned} 2\lambda v_{EW}^2 &= -\Lambda^2 + \epsilon\Lambda F\,\theta_0 + \mu_B^2 \cos\theta_0 \ , \\ r\epsilon\Lambda^3 F &= \left(\mu_B^2 \sin\theta_0 - \epsilon\Lambda F\right) v_{EW}^2 - \Lambda_0^4 \sin\theta_0 \ . \end{aligned} \tag{F.4}$$

Solving these equations for $\sin\theta_0$ and $\cos\theta_0$, and using $\sin^2\theta_0 + \cos\theta_0^2 = 1$ we can determine the value of θ_0. The two solutions are

$$\theta_0 = \frac{\Lambda^2 + 2\lambda v_{EW}^2}{\epsilon F \Lambda} \pm \frac{\mu_B^2}{\epsilon F \Lambda (\mu_B^2 v_{EW}^2 - \Lambda_0^4)} \sqrt{\left(\mu_B^2 v_{EW}^2 - \Lambda_0^4\right)^2 - (\epsilon F \Lambda^3)^2 \left(1 + \frac{v_{EW}^2}{\Lambda^2}\right)} \ . \tag{F.5}$$

The positive sign gives $\cos\theta_0 < 0$, while the negative sign gives $\cos\theta_0 > 0$. We now analyze the minimum conditions. Requiring $\det V'' > 0$, where V'' is the matrix of second derivative of the potential, see the sketch in Fig. 5.5, we obtain

$$\cos\theta_0 > \frac{\epsilon^2 \Lambda^6 F^2 \left(\mu_B^2 + \frac{\Lambda_0^4}{\Lambda^2}\right)^2}{2\lambda_H \left(\mu_B^2 v^2 - \Lambda_0^4\right)^3} \ . \tag{F.6}$$

Since the right hand side is a positive quantity, we immediately conclude that the solution with $\cos\theta_0 < 0$ corresponds to a saddle point, while the solution with $\cos\theta_0 >$ may be a local minimum in some region of parameter space. To determine this region we first translate Eq. (F.6) in a maximum equation for $\sin\theta_0$. We then combine this maximum equation with

Eq. (F.9), obtaining

$$\epsilon F \Lambda^3 < \left[\mu_B^2 v_{EW}^2 - \Lambda_0^4\right] \left[\left(1 + \frac{v_{EW}^2}{\Lambda^2}\right)^2 + \frac{\mu_B^2 + \Lambda_0^4/\Lambda^2}{2\lambda_H(\mu_B^2 v_{EW}^2 - \Lambda_0^4)}\right]^{-1/2} . \tag{F.7}$$

Noticing that the term inside the square brackets is very close to one we end up with $\epsilon F \Lambda^3 \lesssim \mu_B^2 v_{EW}^2 - \Lambda_0^4$ as condition to guarantee the existence of a minimum. As for the saddle point solution, we notice that it corresponds to a minimum in the Higgs direction and to a local maximum in the relaxion direction, see Fig. 5.5. By focussing in the ϕ direction, the difference between the potential in the maximum and in the minimum reads

$$V_{max} - V_{min} = \frac{2(r\mu_B^2\Lambda^2 + \Lambda_0^4)}{\mu_B^2 v_{EW}^2 - \Lambda_0^4} \sqrt{\left(\mu_B^2 v_{EW}^2 - \Lambda_0^4\right)^2 - \epsilon^2 F^2 \Lambda^6 \left(r + \frac{v_{EW}^2}{\Lambda^2}\right)^2} . \tag{F.8}$$

Let us now go back to Eq. (F.4). The second equation can be used to compute

$$\sin\theta_0 = \left(r + \frac{v_{EW}^2}{\Lambda^2}\right) \frac{\epsilon F \Lambda^3}{\mu_B^2 v_{EW}^2 - \Lambda_0^4} . \tag{F.9}$$

Requiring $|\sin\theta_0| \leq 1$ we obtain

$$\Lambda^3 \left(r + \frac{v_{EW}^2}{\Lambda^2}\right) \leq \frac{\mu_B^2 v_{EW}^2 - \Lambda_0^4}{\epsilon F} , \tag{F.10}$$

which is the inequality of Eq. (5.46). *In order to maximize the allowed value of* Λ *we must be close to* $\theta_0 = \pi/2 + 2\pi\kappa$*, with* κ *an integer.* This agrees with the results of Ref. [224]. Using this in Eq. (F.1) allows us to compute how much the Higgs VEV changes as a function of κ. We obtain

$$v^2(\kappa') - v^2(\kappa) = \frac{\pi \epsilon F \Lambda (\kappa' - \kappa)}{\lambda} . \tag{F.11}$$

In the case $\kappa' - \kappa = 1$, i.e. for two subsequent minima, we obtain

$$\Delta v^2 \lesssim \frac{\pi}{\lambda} \frac{\mu_B^2 v_{EW}^2 - \Lambda_0^4}{\Lambda^2} , \tag{F.12}$$

where we have used the condition on the parameter space required by the existence of a

minimum. We then see that the change of the Higgs VEV between subsequent minima is very small.

Appendix G

G.1 Pisarski-Wilczek-Wirstam condition

We start by giving a chronological evolution of the ideas that lead to the Pisarski-Wilczek-Wirstam condition [150; 225].

E. Brézin, Le Guillou and Zinn-Justin in 1973 [226] using Wilson's ϵ-expansion method, see Refs. [227; 228; 229; 230], studying systems described by n-component order parameter. They conclude in their work that there is only one *stable* fixed point under $O(n)$-symmetric interactions, as $n < 4$.

Later in 1975, P. Bak, S. Krinsky and Mukamel [231], besides the three Landau symmetry conditions [231] they propose a fourth one:

> "If there is no stable fixed point within the ϵ-expansion then the transition is first-order."

In the same work, the authors by using the results of Ref.[226] showed that thermodynamic processes that produce *no* change in the unit cell are well described by $O(n)$-symmetric interactions as $n \leq 3$. In contrast, processes that affect the form of the unit cell are described by order parameters of $n \geq 4$ components, see Fig. G.1.

P. Bak et al. in Ref.[231] also noted that the result of E. Brézin et al. in Ref.[226] can be summarized as:

> The isotropic fixed points is *always* stable in $O(n)$-symmetric interactions, as $n \leq 3$.

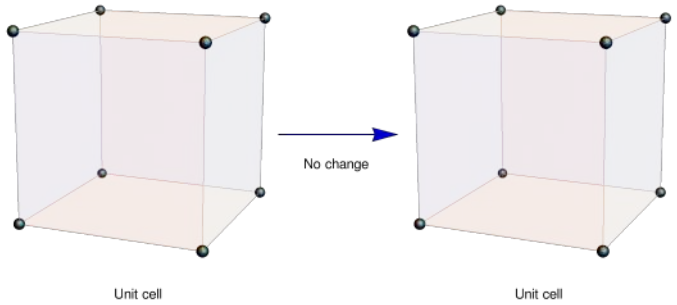

(a)

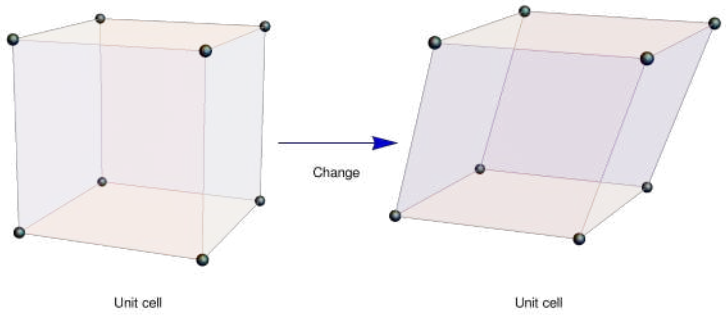

(b)

Figure G.1: (a) Thermodynamic processes that produce *no* change in the unit cell are well described by $O(n)$-symmetric interactions as $n \leq 3$. (b) Processes that affect the form of the unit cell are described by order parameters of $n \geq 4$ components.

This implies that the unstable fixed points could appear in $O(n)$-symmetric interactions, as $n \geq 4$. They did not prove their conjecture; however, they gave five different Hamiltonians with $n \geq 4$ components as examples. The running coupling constants associated with those Hamiltonians posses no stable fixed points [231] and have FOPT. In Table G.1, we show those five types of physical systems.

The connection between RG fixed points and FOPT may be is not evident. We can under-

Anti-ferromagnetic order	Number of components of order parameter	Systems know to be first-order
Type I ($\vec{m} \perp \vec{k}$)	$n = 6$	UO_2
Type II ($\vec{m} \perp \vec{k}$)	$n = 8$	MnO
Type III ($\vec{m} \,\|\| \, [100], \vec{k} = [\frac{1}{2}\, 0\, 1]$)	$n = 12$	
Sinusoidal ($\vec{m} \perp \vec{k} = [k\, 0\, 0]$)	$n = 12$	Cr
Screw spiral ($\vec{m} \perp \vec{k} = [k\, 0\, 0]$)	$n = 12$	Eu

Table G.1: Physical systems corresponding to Hamiltonians with no stable fixed points[231]

stand that relation in the following way. Let us consider the system defined by the action

$$S = S^{\star} + g \int d^D x \, \mathcal{O}[\phi(x)] \tag{G.1}$$

where $S^{\star}$ is the action of a theory defined by fixed points. Because $S^{\star}$ cannot depend on microscopic details, it is a scale invariant theory.

Under the change of scale $x \to \lambda x$, as $\lambda > 0$

$$S' = S^{\star} + \lambda^y \, g \int d^D x \, \mathcal{O}[\widehat{\phi}(x)]. \tag{G.2}$$

For $y > 0$, the IR RG flow for one relevant operator is schematically showed in Fig.G.2.

Fig.G.2 shows an unstable fixed point with its RG flow. This defines a phase transition between two phases, one to the left and the other to the right [232].

In 1980, H. H. Iacobson and D. J. Amit in Ref.[233] generalize the previous work of E. Brézin et al. [226], they focused in the study of n-component order parameter theories with couplings of the type $g_{ijkl}\, \phi_i \, \phi_j \, \phi_k \, \phi_l$. They show that if the interaction has more than one

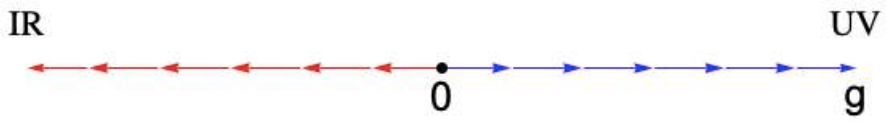

Figure G.2: IR RG flow for one relevant operator. This is an unstable fixed point.

invariant there are systems with stable fixed points; however, the allowed domain of the renormalized couplings includes regions where the running of couplings are not attracted to the stable fixed points.

In their work H. Iacobson and J. Amit [233] focused on lagragians of the type

$$\mathcal{L} = \frac{1}{2}\partial_\mu \phi_i \, \partial^\mu \phi^i - \frac{r^2}{2}\phi_i \phi_i - g_{ijk}\phi_i \phi_j \phi_k \phi_l, \tag{G.3}$$

with two invariants: the $O(n)$ one and the cubic anisotropy $\sum_i \phi_i^4$. Hence, the *trace condition* [226] is imposed

$$g_{ijkk} = g\,\delta_{ij}. \tag{G.4}$$

The domain of variation of the scale μ is $0 < \mu < \infty$. While the IR region is getting by taking the limit $\mu \to 0$, the UV behavior is obtained as $\mu \to \infty$ [233]. The trajectory of $g(\mu)$ is defined inside that domain, and flowing from the UV to IR. The equation that governs its trajectory if the beta function of g

$$\beta_{ijkl}(g) = \mu \frac{\partial\, g_{ijkl}}{\partial\, \mu} \tag{G.5}$$

where at one-loop [226; 233]

$$\mu \frac{\partial\, g_{ijkl}}{\partial\, \mu} = -\epsilon\, g_{ijkl} + \frac{1}{2}\left(g_{ijpq}\, g_{pqkl} + i \leftrightarrow k + i \leftrightarrow l\right). \tag{G.6}$$

The stability of the vacuum is studied by characterizing the domain of boundedness from below of the effective potential, $V_{\text{eff}}(\phi)$.

Ref.[226] shows that the boundedness form below of the effective potential is equivalent to the positivity of the bare quartic form $g^0_{ijkl}\,\phi_i\phi_j\phi_k\phi_l$. This condition defines the domain P^+, where the bare quartic form is positive. The equivalent statement for the renormalized coupling constants, g_{ijkl}, has to consider that the renormalized interaction defines an asymptotically free model. This means two things

1. $\lim_{\mu\to\infty} g(\mu) = 0$,

2. $\beta(g) < 0$,

where $g(\phi,\mu) = g_{ijkl}(\mu)\,\phi_i\phi_j\phi_k\phi_l$. The first condition together with the condition on the bare coupling implies that a system is stable if and only if $g(\phi,\mu)$ is positive for all $\mu > \widetilde{\mu}$, for large enough $\widetilde{\mu}$. Second condition and Eq.G.6 allows to find the inequality

$$g(\phi,\mu) < \frac{2}{3}\,\epsilon. \tag{G.7}$$

H. Iacobson et al. [233] showed that may exist trajectories that start within P^+ and that eventually run away of the domain P^+ as $\mu \to 0$. In Fig.G.3 we show an allowed and a forbidden trajectory as examples.

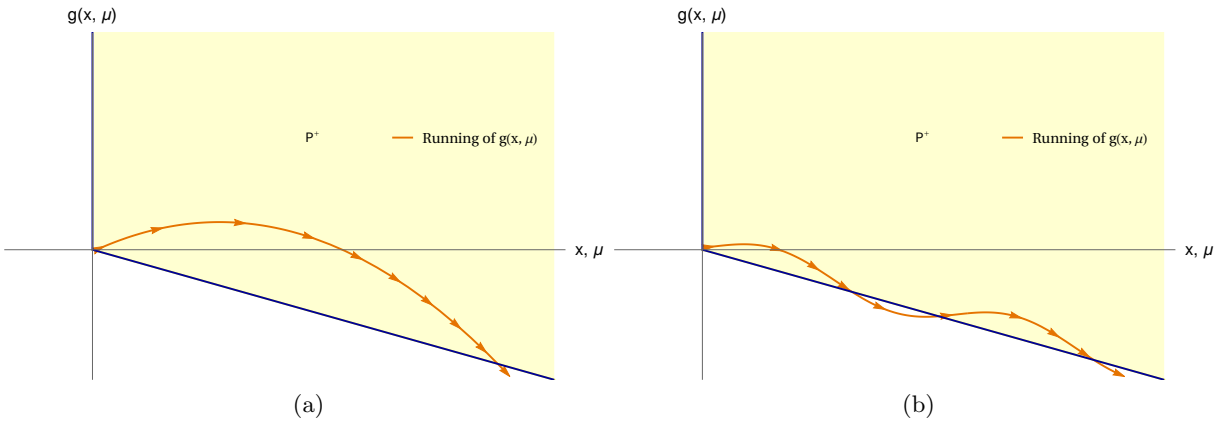

(a) (b)

Figure G.3: (a) Allowed trajectory. (b) Forbidden trajectory.

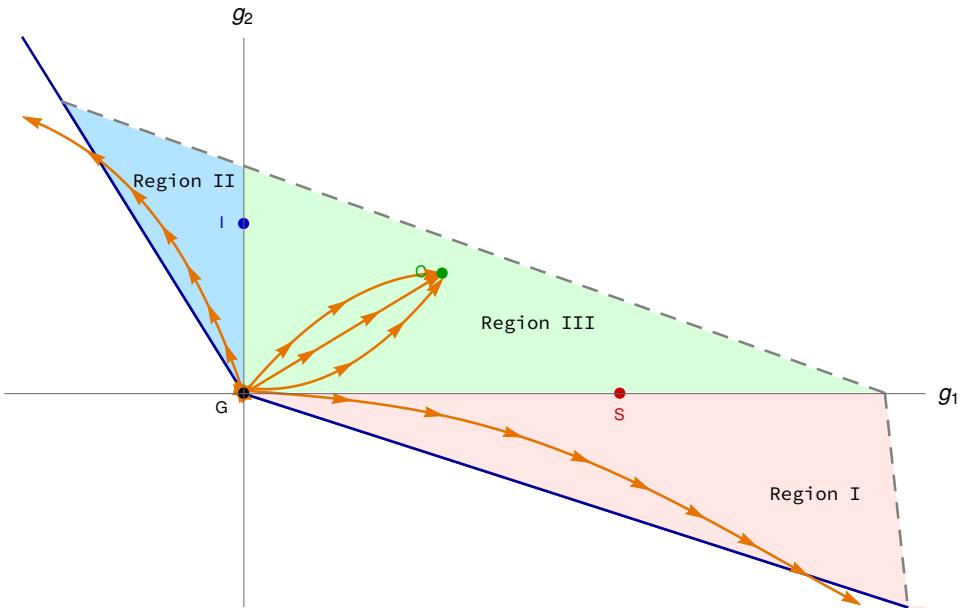

Figure G.4: Flow diagram for the particular case of cubic anisotropy [233].

A particular case of Eq.(G.3) (and the important for us) is the case of cubic anisotropy

$$\mathcal{L} = \frac{1}{2}(\partial\,\phi)^2 - \frac{r^2}{2}\,\phi^2 - \frac{1}{4}g_1^0(\phi^2)^2 - \frac{1}{4}g_2^0\sum_{i=1}^{n}\phi_i^4. \tag{G.8}$$

From Eq.(G.6) the renormalized coupling constant equations are

$$\mu\frac{\partial\,g_1}{d\,\mu} = -\epsilon\,g_1 + \frac{n+8}{6}\,g_1^2 + g_1\,g_2, \tag{G.9}$$

$$\mu\frac{\partial\,g_1}{d\,\mu} = -\epsilon\,g_2 + \frac{3}{2}\,g_2^2 + 2\,g_1\,g_2, \tag{G.10}$$

Ref.[233] stress that there are four fixed points in this case, they are

(a) gaussian $(g_1, g_2) = (0, 0)$,

(b) symmetric $(g_1, g_2) = (6\,\epsilon/(n+8), 0)$,

(c) Ising like $(g_1, g_2) = (0, \frac{2}{3}\,\epsilon)$,

(d) cubic $(g_1, g_2) = (2\,\epsilon/n, 2(n-4)\,\epsilon/3\,n)$.

The domain P^+ is defined by the lines L_1 and L_2 [226], which are respectively:

$$g_1 + g_2 = 0, \tag{G.11}$$

$$g_1 + g_2/n = 0. \tag{G.12}$$

The flow diagram is shown in Fig.G.4.As mentioned before, there are trajectories that, although start inside P^+, they run away of that domain as $\mu \to 0$. From Fig.G.4 we see that such trajectories are the ones very close to the boundaries L_1, L_2.

Using this results H. Iacobson et al. [233] computed the V_{eff} for the cubic anisotropy, and impose the condition $g_1 + g_2 = B\,\epsilon^2$, as $B > 0$. In other words, they focused on trajectories near the boundary. They showed that V_{eff} can satisfy the equations

$$\left.\frac{\partial V_{\text{eff}}}{\partial \phi}\right|_{\phi=\phi_1} = 0, \tag{G.13}$$

$$V_{\text{eff}}(\phi_1) = V_{\text{eff}}(0), \tag{G.14}$$

thus defining a FOPT.

After this Pisarski et al. [150] used that resu;ts to analyse the low energy effective field theory of a strongly interacting theory with N_f flavors and N_c colors, the linear sigma model:

$$\mathcal{L} = \frac{1}{2}\langle \partial\,\Phi^\dagger \partial\,\Phi\rangle - \frac{m_\Phi^2}{2}\langle \Phi^\dagger\,\Phi\rangle - \frac{\pi^2}{3} g_1 \left(\langle \Phi^\dagger\,\Phi\rangle\right)^2 - \frac{\pi^2}{3} g_2 \langle \left(\Phi^\dagger\,\Phi\right)^2\rangle \tag{G.15}$$

where we use the notation of Ref.[150]. Beta functions given by Eqs.(G.9) and (G.10) are slightly modified to

$$\beta_1 = -\epsilon\, g_1 + \frac{N_f^2 + 4}{3}\, g_1^2 + \frac{4N_f}{3} g_1\, g_2 + g_2^2, \tag{G.16}$$

$$\beta_2 = -\epsilon\, g_2 + \frac{2N_f}{3}\, g_2^2 + 2\, g_1\, g_2. \tag{G.17}$$

By analysing when the stability matrix $\omega_{ij} = \partial\beta_i/\partial g_j$ has no real and positive eigenvalues, which implies that there is no IR stable fixed points, they found that the PT remains first order if $N_f \geq 3$ [150].

References

[1] "2351: Standard model changes - explain xkcd." https://www.explainxkcd.com/wiki/index.php/2351:_Standard_Model_Changes. 5

[2] B. Gripaios, "Lectures on Physics Beyond the Standard Model," 3 2015. 5

[3] B. C. Allanach, "Beyond the Standard Model Lectures for the 2016 European School of High-Energy Physics," in *2016 European School of High-Energy Physics*, 9 2016. 5

[4] D. Kazakov, "Beyond the Standard Model' 17," *CERN Yellow Rep. School Proc.*, vol. 3, pp. 83–131, 2018. 5

[5] M. Y. Khlopov, "Beyond the Standard models of particle physics and cosmology," *Bled Workshops Phys.*, vol. 19, no. 2, pp. 314–326, 2018. 5

[6] A. Wulzer, "Behind the Standard Model," in *2015 European School of High-Energy Physics*, 1 2019. 5

[7] E. Fermi, "Tentativo di una teoria dell'emissione dei raggi beta," *Ric. Sci.*, vol. 4, pp. 491–495, 1933. 6, 12

[8] E. Fermi, "An attempt of a theory of beta radiation. 1.," *Z. Phys.*, vol. 88, pp. 161–177, 1934. 6, 12

[9] E. Fermi, "Trends to a Theory of beta Radiation. (In Italian)," *Nuovo Cim.*, vol. 11, pp. 1–19, 1934. 6, 12

[10] S. Betts *et al.*, "Development of a Relic Neutrino Detection Experiment at PTOLEMY: Princeton Tritium Observatory for Light, Early-Universe, Massive-Neutrino Yield," in *Community Summer Study 2013: Snowmass on the Mississippi*, 7 2013. 6, 40, 41, 42, 49, 52

[11] E. Baracchini *et al.*, "PTOLEMY: A Proposal for Thermal Relic Detection of Massive Neutrinos and Directional Detection of MeV Dark Matter," 8 2018. 6, 40, 41, 42

[12] "Quantum diaries." https://www.quantumdiaries.org/2011/11/11/effective-field-theory-for-turtles/. (Accessed on 03/25/2021). 8

[13] T. Appelquist and J. Carazzone, "Infrared Singularities and Massive Fields," *Phys. Rev. D*, vol. 11, p. 2856, 1975. 9, 10, 11, 12

[14] D. B. Chitwood *et al.*, "Improved measurement of the positive muon lifetime and determination of the Fermi constant," *Phys. Rev. Lett.*, vol. 99, p. 032001, 2007. 13

[15] W. Buchmuller and D. Wyler, "Effective Lagrangian Analysis of New Interactions and Flavor Conservation," *Nucl. Phys. B*, vol. 268, pp. 621–653, 1986. 17

[16] B. Grzadkowski, M. Iskrzynski, M. Misiak, and J. Rosiek, "Dimension-Six Terms in the Standard Model Lagrangian," *JHEP*, vol. 10, p. 085, 2010. 17, 18, 20, 46

[17] B. Henning, X. Lu, T. Melia, and H. Murayama, "2, 84, 30, 993, 560, 15456, 11962, 261485, ...: Higher dimension operators in the sm eft," 2019. 17, 20, 21, 22

[18] A. Helset and A. Kobach, "Baryon number, lepton number, and operator dimension in the smeft with flavor symmetries," *Physics Letters B*, vol. 800, p. 135132, Jan 2020. 18

[19] S. Weinberg, "Baryon- and lepton-nonconserving processes," *Phys. Rev. Lett.*, vol. 43, pp. 1566–1570, Nov 1979. 19

[20] A. Vicente, "Phenomenology of supersymmetric neutrino mass models," 2011. 19

[21] L. Lehman, "Extending the standard model effective field theory with the complete set of dimension-7 operators," *Physical Review D*, vol. 90, Dec 2014. 21

[22] L. Lehman and A. Martin, "Low-derivative operators of the standard model effective field theory via hilbert series methods," *Journal of High Energy Physics*, vol. 2016, Feb 2016. 21

[23] A. Hanany, E. E. Jenkins, A. V. Manohar, and G. Torri, "Hilbert series for flavor invariants of the standard model," *Journal of High Energy Physics*, vol. 2011, Mar 2011. 21

[24] A. V. Manohar, "Introduction to effective field theories," 2018. 21

[25] J. L. Cardy, "Operator content and modular properties of higher dimensional conformal field theories," *Nucl. Phys. B*, vol. 366, pp. 403–419, 1991. 21

[26] M. Gell-Mann and M. Levy, "The axial vector current in beta decay," *Nuovo Cim.*, vol. 16, p. 705, 1960. 21, 22

[27] A. Pich, "Effective field theory with nambu-goldstone modes," 2020. 23

[28] D. Croon, R. Houtz, and V. Sanz, "Dynamical Axions and Gravitational Waves," *JHEP*, vol. 07, p. 146, 2019. 25, 93, 96, 105, 108, 110, 137

[29] "Jorge s. diaz en twitter: "@danielandjorge "net mass infinitesimally insignificant" #neutrino oscillations: Am i a joke to you?" / twitter." https://twitter.com/DanielandJorge/status/1284143832435552257/photo/1. (Accessed on 03/25/2021). 26

[30] C. Quigg, "Cosmic Neutrinos," in *35th SLAC Summer Institute on Particle Physics: Dark matter: From the cosmos to the Laboratory*, 2 2008. 26, 29

[31] L. M. Krauss, S. L. Glashow, and D. N. Schramm, "Anti-neutrinos Astronomy and Geophysics," *Nature*, vol. 310, pp. 191–198, 1984. 27

[32] G. Fiorentini, M. Lissia, F. Mantovani, and R. Vannucci, "Geo-Neutrinos: A Short review," *Nucl. Phys. B Proc. Suppl.*, vol. 143, pp. 53–59, 2005. 27

[33] S. Abe *et al.*, "Precision Measurement of Neutrino Oscillation Parameters with KamLAND," *Phys. Rev. Lett.*, vol. 100, p. 221803, 2008. 27, 32, 33, 37

[34] W. Commons, "File:standard model of elementary particles.svg — wikimedia commons, the free media repository," 2019. [Online; accessed 2-July-2019]. 28

[35] R. H. Dicke, P. J. E. Peebles, P. G. Roll, and D. T. Wilkinson, "Cosmic Black-Body Radiation," *Astrophys. J.*, vol. 142, pp. 414–419, 1965. 33

[36] A. J. Long, C. Lunardini, and E. Sabancilar, "Detecting non-relativistic cosmic neutrinos by capture on tritium: phenomenology and physics potential," *JCAP*, vol. 08, p. 038, 2014. 35, 40, 43, 44, 45, 47, 50, 51, 113

[37] C. L. Bennett *et al.*, "First year Wilkinson Microwave Anisotropy Probe (WMAP) observations: Preliminary maps and basic results," *Astrophys. J. Suppl.*, vol. 148, pp. 1–27, 2003. 36

[38] P. A. R. Ade *et al.*, "Planck 2013 results. XVI. Cosmological parameters," *Astron. Astrophys.*, vol. 571, p. A16, 2014. 36

[39] "zerfall-transparent-10.gif (736544)." http://www.physics.utah.edu/~jui/5110/y2009m03d09/KATRIN.htm;_files/zerfall-transparent-10.gif. (Accessed on 07/02/2019). 38

[40] S. Weinberg, "Universal Neutrino Degeneracy," *Phys. Rev.*, vol. 128, pp. 1457–1473, 1962. 39, 49

[41] A. G. Cocco, G. Mangano, and M. Messina, "Probing low energy neutrino backgrounds with neutrino capture on beta decaying nuclei," *JCAP*, vol. 06, p. 015, 2007. 39, 40

[42] "Snowmass21-nf4_nf10_ptolemy-021.pdf." https://www.snowmass21.org/docs/files/summaries/NF/SNOWMASS21-NF4_NF10_PTOLEMY-021.pdf, 2021. 41

[43] M. Gell-Mann, P. Ramond, and R. Slansky, "Complex Spinors and Unified Theories," *Conf. Proc. C*, vol. 790927, pp. 315–321, 1979. 44

[44] V. Cirigliano, M. Gonzalez-Alonso, and M. L. Graesser, "Non-standard Charged Current Interactions: beta decays versus the LHC," *JHEP*, vol. 02, p. 046, 2013. 46, 47, 52, 53

[45] V. Cirigliano, S. Gardner, and B. Holstein, "Beta Decays and Non-Standard Interactions in the LHC Era," *Prog. Part. Nucl. Phys.*, vol. 71, pp. 93–118, 2013. 46, 52, 53

[46] P. O. Ludl and W. Rodejohann, "Direct Neutrino Mass Experiments and Exotic Charged Current Interactions," *JHEP*, vol. 06, p. 040, 2016. 47, 51, 55

[47] Y. A. Akulov and B. A. Mamyrin, "Determination of the ratio of the axial-vector to the vector coupling constant for weak interaction in triton beta decay," *Phys. Atom. Nucl.*, vol. 65, pp. 1795–1797, 2002. 47, 49

[48] M. González-Alonso and J. Martin Camalich, "Isospin breaking in the nucleon mass and the sensitivity of β decays to new physics," *Phys. Rev. Lett.*, vol. 112, no. 4, p. 042501, 2014. 47, 49

[49] T. Bhattacharya, V. Cirigliano, R. Gupta, H.-W. Lin, and B. Yoon, "Neutron Electric Dipole Moment and Tensor Charges from Lattice QCD," *Phys. Rev. Lett.*, vol. 115, no. 21, p. 212002, 2015. 47, 49

[50] S. S. Gershtein and Y. B. Zeldovich, "Meson corrections in the theory of beta decay," *Zh. Eksp. Teor. Fiz.*, vol. 29, pp. 698–699, 1955. 49

[51] R. P. Feynman and M. Gell-Mann, "Theory of Fermi interaction," *Phys. Rev.*, vol. 109, pp. 193–198, 1958. 49

[52] J. C. Hardy and I. S. Towner, "Superallowed 0+ —> 0+ nuclear beta decays: A New survey with precision tests of the conserved vector current hypothesis and the standard model," *Phys. Rev. C*, vol. 79, p. 055502, 2009. 52, 53

[53] V. Mateu and J. Portoles, "Form-factors in radiative pion decay," *Eur. Phys. J. C*, vol. 52, pp. 325–338, 2007. 52, 53

[54] T. Bhattacharya, V. Cirigliano, S. D. Cohen, A. Filipuzzi, M. Gonzalez-Alonso, M. L. Graesser, R. Gupta, and H.-W. Lin, "Probing Novel Scalar and Tensor Interactions from (Ultra)Cold Neutrons to the LHC," *Phys. Rev. D*, vol. 85, p. 054512, 2012. 52, 53

[55] N. Severijns, M. Beck, and O. Naviliat-Cuncic, "Tests of the standard electroweak model in beta decay," *Rev. Mod. Phys.*, vol. 78, pp. 991–1040, 2006. 52, 53

[56] O. Naviliat-Cuncic and M. González-Alonso, "Prospects for precision measurements in nuclear β decay at the LHC era," *Annalen Phys.*, vol. 525, pp. 600–619, 2013. 53

[57] B. A. Campbell and D. W. Maybury, "Constraints on scalar couplings from pi+- —> l+- nu(l)," *Nucl. Phys. B*, vol. 709, pp. 419–439, 2005. 53

[58] G. Duda, G. Gelmini, and S. Nussinov, "Expected signals in relic neutrino detectors," *Phys. Rev. D*, vol. 64, p. 122001, 2001. 56

[59] P. F. de Salas, S. Gariazzo, J. Lesgourgues, and S. Pastor, "Calculation of the local density of relic neutrinos," *JCAP*, vol. 09, p. 034, 2017. 57

[60] L. A. Anchordoqui, H. Goldberg, and G. Steigman, "Right-Handed Neutrinos as the Dark Radiation: Status and Forecasts for the LHC," *Phys. Lett. B*, vol. 718, pp. 1162–1165, 2013. 57, 58

[61] A. Solaguren-Beascoa and M. C. Gonzalez-Garcia, "Dark Radiation Confronting LHC in Z' Models," *Phys. Lett. B*, vol. 719, pp. 121–125, 2013. 57, 58

[62] J. Zhang and S. Zhou, "Relic Right-handed Dirac Neutrinos and Implications for Detection of Cosmic Neutrino Background," *Nucl. Phys. B*, vol. 903, pp. 211–225, 2016. 57, 58

[63] P. A. R. Ade *et al.*, "Planck 2015 results. XIII. Cosmological parameters," *Astron. Astrophys.*, vol. 594, p. A13, 2016. 58, 121

[64] M.-C. Chen, M. Ratz, and A. Trautner, "Nonthermal cosmic neutrino background," *Phys. Rev. D*, vol. 92, no. 12, p. 123006, 2015. 59

[65] "+: The periodic table of dark matter." http://www.terrycolon.com/2features/dark-matter.html. (Accessed on 03/31/2021). 60

[66] M. J. Strassler and K. M. Zurek, "Echoes of a hidden valley at hadron colliders," *Phys. Lett. B*, vol. 651, pp. 374–379, 2007. 60, 61

[67] M. J. Strassler and K. M. Zurek, "Discovering the Higgs through highly-displaced vertices," *Phys. Lett. B*, vol. 661, pp. 263–267, 2008. 60

[68] H. Beauchesne, E. Bertuzzo, G. Grilli Di Cortona, and Z. Tabrizi, "Collider phenomenology of Hidden Valley mediators of spin 0 or 1/2 with semivisible jets," *JHEP*, vol. 08, p. 030, 2018. 60, 61, 124

[69] M. Battaglieri *et al.*, "US Cosmic Visions: New Ideas in Dark Matter 2017: Community Report," in *U.S. Cosmic Visions: New Ideas in Dark Matter*, 7 2017. 60

[70] Z. Chacko, H.-S. Goh, and R. Harnik, "The Twin Higgs: Natural electroweak breaking from mirror symmetry," *Phys. Rev. Lett.*, vol. 96, p. 231802, 2006. 60

[71] G. Burdman, Z. Chacko, H.-S. Goh, and R. Harnik, "Folded supersymmetry and the LEP paradox," *JHEP*, vol. 02, p. 009, 2007. 60

[72] P. W. Graham, D. E. Kaplan, and S. Rajendran, "Cosmological relaxation of the electroweak scale," *Physical Review Letters*, vol. 115, 2015. 60, 77, 78, 82, 83, 86, 87, 97, 138, 140

[73] D. Curtin *et al.*, "Long-Lived Particles at the Energy Frontier: The MATHUSLA Physics Case," *Rept. Prog. Phys.*, vol. 82, no. 11, p. 116201, 2019. 60

[74] M. J. Strassler, "On the Phenomenology of Hidden Valleys with Heavy Flavor," 6 2008. 61

[75] R. J. Hill and M. P. Solon, "Universal behavior in the scattering of heavy, weakly interacting dark matter on nuclear targets," *Phys. Lett. B*, vol. 707, pp. 539–545, 2012. 62

[76] M. T. Frandsen, U. Haisch, F. Kahlhoefer, P. Mertsch, and K. Schmidt-Hoberg, "Loop-induced dark matter direct detection signals from gamma-ray lines," *JCAP*, vol. 10, p. 033, 2012. 62

[77] L. Vecchi, "WIMPs and Un-Naturalness," 12 2013. 62

[78] A. Crivellin, F. D'Eramo, and M. Procura, "New Constraints on Dark Matter Effective Theories from Standard Model Loops," *Phys. Rev. Lett.*, vol. 112, p. 191304, 2014. 62, 69

[79] F. D'Eramo and M. Procura, "Connecting Dark Matter UV Complete Models to Direct Detection Rates via Effective Field Theory," *JHEP*, vol. 04, p. 054, 2015. 62, 69, 71, 125

[80] F. D'Eramo, B. J. Kavanagh, and P. Panci, "You can hide but you have to run: direct detection with vector mediators," *JHEP*, vol. 08, p. 111, 2016. 62, 69

[81] J. Brod, A. Gootjes-Dreesbach, M. Tammaro, and J. Zupan, "Effective Field Theory for Dark Matter Direct Detection up to Dimension Seven," *JHEP*, vol. 10, p. 065, 2018. 62, 64

[82] J. Brod, B. Grinstein, E. Stamou, and J. Zupan, "Weak mixing below the weak scale in dark-matter direct detection," *JHEP*, vol. 02, p. 174, 2018. 62, 129

[83] A. Belyaev, E. Bertuzzo, C. Caniu Barros, O. Eboli, G. Grilli Di Cortona, F. Iocco, and A. Pukhov, "Interplay of the LHC and non-LHC Dark Matter searches in the Effective Field Theory approach," *Phys. Rev. D*, vol. 99, no. 1, p. 015006, 2019. 62

[84] H. Beauchesne, E. Bertuzzo, and G. Grilli Di Cortona, "Dark matter in Hidden Valley models with stable and unstable light dark mesons," *JHEP*, vol. 04, p. 118, 2019. 62, 63

[85] W. Chao, H.-K. Guo, and H.-L. Li, "Tau flavored dark matter and its impact on tau Yukawa coupling," *JCAP*, vol. 02, p. 002, 2017. 62

[86] E. Bertuzzo, C. J. Caniu Barros, and G. Grilli di Cortona, "MeV Dark Matter: Model Independent Bounds," *JHEP*, vol. 09, p. 116, 2017. 62

[87] F. D'Eramo, B. J. Kavanagh, and P. Panci, "rundm (version 1.0) [computer software] doi:10.5281/zenodo.823249 https://github.com/bradkav/rundm/." 62

[88] F. Bishara, J. Brod, B. Grinstein, and J. Zupan, "DirectDM: a tool for dark matter direct detection," 8 2017. 62

[89] J. Kile and A. Soni, "Flavored Dark Matter in Direct Detection Experiments and at LHC," *Phys. Rev. D*, vol. 84, p. 035016, 2011. 62

[90] B. Batell, J. Pradler, and M. Spannowsky, "Dark Matter from Minimal Flavor Violation," *JHEP*, vol. 08, p. 038, 2011. 62

[91] J. F. Kamenik and J. Zupan, "Discovering Dark Matter Through Flavor Violation at the LHC," *Phys. Rev. D*, vol. 84, p. 111502, 2011. 62

[92] P. Agrawal, S. Blanchet, Z. Chacko, and C. Kilic, "Flavored Dark Matter, and Its Implications for Direct Detection and Colliders," *Phys. Rev. D*, vol. 86, p. 055002, 2012. 62

[93] L. Lopez-Honorez and L. Merlo, "Dark matter within the minimal flavour violation ansatz," *Phys. Lett. B*, vol. 722, pp. 135–143, 2013. 62

[94] J. Kile, "Flavored Dark Matter: A Review," *Mod. Phys. Lett. A*, vol. 28, p. 1330031, 2013. 62

[95] Y. Bai and J. Berger, "Fermion Portal Dark Matter," *JHEP*, vol. 11, p. 171, 2013. 62

[96] B. Batell, T. Lin, and L.-T. Wang, "Flavored Dark Matter and R-Parity Violation," *JHEP*, vol. 01, p. 075, 2014. 62

[97] M. A. Gomez, C. B. Jackson, and G. Shaughnessy, "Dark Matter on Top," *JCAP*, vol. 12, p. 025, 2014. 62

[98] P. Agrawal, M. Blanke, and K. Gemmler, "Flavored dark matter beyond Minimal Flavor Violation," *JHEP*, vol. 10, p. 072, 2014. 62

[99] T. Abe, J. Kawamura, S. Okawa, and Y. Omura, "Dark matter physics, flavor physics and LHC constraints in the dark matter model with a bottom partner," *JHEP*, vol. 03, p. 058, 2017. 62

[100] M. Blanke and S. Kast, "Top-Flavoured Dark Matter in Dark Minimal Flavour Violation," *JHEP*, vol. 05, p. 162, 2017. 62, 124

[101] M. Blanke, S. Das, and S. Kast, "Flavoured Dark Matter Moving Left," *JHEP*, vol. 02, p. 105, 2018. 62

[102] W. Chao, H.-K. Guo, H.-L. Li, and J. Shu, "Electron Flavored Dark Matter," *Phys. Lett. B*, vol. 782, pp. 517–522, 2018. 62

[103] F. Bishara, J. Brod, B. Grinstein, and J. Zupan, "Renormalization Group Effects in Dark Matter Interactions," *JHEP*, vol. 03, p. 089, 2020. 62, 76, 129

[104] Y. Hochberg, E. Kuflik, T. Volansky, and J. G. Wacker, "Mechanism for Thermal Relic Dark Matter of Strongly Interacting Massive Particles," *Phys. Rev. Lett.*, vol. 113, p. 171301, 2014. 63

[105] S. Okawa, M. Tanabashi, and M. Yamanaka, "Relic Abundance in a Secluded Dark Matter Scenario with a Massive Mediator," *Phys. Rev. D*, vol. 95, no. 2, p. 023006, 2017. 63

[106] C. P. Burgess, M. Pospelov, and T. ter Veldhuis, "The Minimal model of nonbaryonic dark matter: A Singlet scalar," *Nucl. Phys. B*, vol. 619, pp. 709–728, 2001. 64

[107] N. Arkani-Hamed, D. P. Finkbeiner, T. R. Slatyer, and N. Weiner, "A Theory of Dark Matter," *Phys. Rev. D*, vol. 79, p. 015014, 2009. 64

[108] A. Falkowski, J. Juknevich, and J. Shelton, "Dark Matter Through the Neutrino Portal," 8 2009. 64

[109] E. Bertuzzo, S. Jana, P. A. N. Machado, and R. Zukanovich Funchal, "Neutrino Masses and Mixings Dynamically Generated by a Light Dark Sector," *Phys. Lett. B*, vol. 791, pp. 210–214, 2019. 64

[110] F. D'Eramo, B. J. Kavanagh, and P. Panci, "Probing Leptophilic Dark Sectors with Hadronic Processes," *Phys. Lett. B*, vol. 771, pp. 339–348, 2017. 69

[111] M. E. Machacek and M. T. Vaughn, "Two Loop Renormalization Group Equations in a General Quantum Field Theory. 1. Wave Function Renormalization," *Nucl. Phys. B*, vol. 222, pp. 83–103, 1983. 69, 127

[112] M. E. Machacek and M. T. Vaughn, "Two Loop Renormalization Group Equations in a General Quantum Field Theory. 2. Yukawa Couplings," *Nucl. Phys. B*, vol. 236, pp. 221–232, 1984. 69, 127

[113] Z.-z. Xing, H. Zhang, and S. Zhou, "Impacts of the Higgs mass on vacuum stability, running fermion masses and two-body Higgs decays," *Phys. Rev. D*, vol. 86, p. 013013, 2012. 71

[114] J. F. Kamenik and C. Smith, "FCNC portals to the dark sector," *JHEP*, vol. 03, p. 090, 2012. 75

[115] G. Aad *et al.*, "Observation of a new particle in the search for the Standard Model Higgs boson with the ATLAS detector at the LHC," *Phys. Lett.*, vol. B716, pp. 1–29, 2012. 77, 80

[116] S. Chatrchyan *et al.*, "Observation of a New Boson at a Mass of 125 GeV with the CMS Experiment at the LHC," *Phys. Lett. B*, vol. 716, pp. 30–61, 2012. 77

[117] B. P. Abbott *et al.*, "Observation of Gravitational Waves from a Binary Black Hole Merger," *Phys. Rev. Lett.*, vol. 116, no. 6, p. 061102, 2016. 77

[118] B. Abbott, R. Abbott, T. Abbott, F. Acernese, K. Ackley, C. Adams, T. Adams, P. Addesso, R. Adhikari, V. Adya, and et al., "Gw170817: Observation of gravitational

waves from a binary neutron star inspiral," *Physical Review Letters*, vol. 119, Oct 2017. 77

[119] J. R. Espinosa, C. Grojean, G. Panico, A. Pomarol, O. Pujolàs, and G. Servant, "Cosmological Higgs-Axion Interplay for a Naturally Small Electroweak Scale," *Phys. Rev. Lett.*, vol. 115, no. 25, p. 251803, 2015. 78

[120] S. P. Patil and P. Schwaller, "Relaxing the Electroweak Scale: the Role of Broken dS Symmetry," *JHEP*, vol. 02, p. 077, 2016. 78

[121] E. Hardy, "Electroweak relaxation from finite temperature," *JHEP*, vol. 11, p. 077, 2015. 78, 99

[122] J. Jaeckel, V. M. Mehta, and L. T. Witkowski, "Musings on cosmological relaxation and the hierarchy problem," *Phys. Rev. D*, vol. 93, no. 6, p. 063522, 2016. 78

[123] R. S. Gupta, Z. Komargodski, G. Perez, and L. Ubaldi, "Is the Relaxion an Axion?," *JHEP*, vol. 02, p. 166, 2016. 78

[124] O. Matsedonskyi, "Mirror Cosmological Relaxation of the Electroweak Scale," *JHEP*, vol. 01, p. 063, 2016. 78

[125] L. Marzola and M. Raidal, "Natural relaxation," *Mod. Phys. Lett. A*, vol. 31, p. 1650215, 2016. 78

[126] S. Di Chiara, K. Kannike, L. Marzola, A. Racioppi, M. Raidal, and C. Spethmann, "Relaxion Cosmology and the Price of Fine-Tuning," *Phys. Rev. D*, vol. 93, no. 10, p. 103527, 2016. 78

[127] L. E. Ibanez, M. Montero, A. Uranga, and I. Valenzuela, "Relaxion Monodromy and the Weak Gravity Conjecture," *JHEP*, vol. 04, p. 020, 2016. 78

[128] A. Fowlie, C. Balazs, G. White, L. Marzola, and M. Raidal, "Naturalness of the relaxion mechanism," *JHEP*, vol. 08, p. 100, 2016. 78

[129] T. Kobayashi, O. Seto, T. Shimomura, and Y. Urakawa, "Relaxion window," *Mod. Phys. Lett. A*, vol. 32, no. 27, p. 1750142, 2017. 78

[130] K. Choi and S. H. Im, "Constraints on Relaxion Windows," *JHEP*, vol. 12, p. 093, 2016. 78

[131] T. Flacke, C. Frugiuele, E. Fuchs, R. S. Gupta, and G. Perez, "Phenomenology of relaxion-Higgs mixing," *JHEP*, vol. 06, p. 050, 2017. 78

[132] A. Nelson and C. Prescod-Weinstein, "Relaxion: A Landscape Without Anthropics," *Phys. Rev. D*, vol. 96, no. 11, p. 113007, 2017. 78

[133] K. S. Jeong and C. S. Shin, "Peccei-Quinn Relaxion," *JHEP*, vol. 01, p. 121, 2018. 78

[134] O. Davidi, R. S. Gupta, G. Perez, D. Redigolo, and A. Shalit, "Nelson-Barr relaxion," *Phys. Rev. D*, vol. 99, no. 3, p. 035014, 2019. 78

[135] O. Davidi, R. S. Gupta, G. Perez, D. Redigolo, and A. Shalit, "The hierarchion, a relaxion addressing the Standard Model's hierarchies," *JHEP*, vol. 08, p. 153, 2018. 78

[136] S. A. Abel, R. S. Gupta, and J. Scholtz, "Out-of-the-box Baryogenesis During Relaxation," *Phys. Rev. D*, vol. 100, no. 1, p. 015034, 2019. 78

[137] R. S. Gupta, J. Y. Reiness, and M. Spannowsky, "All-in-one relaxion: A unified solution to five particle-physics puzzles," *Phys. Rev. D*, vol. 100, no. 5, p. 055003, 2019. 78

[138] T. Higaki, N. Takeda, and Y. Yamada, "Cosmological relaxation and high scale inflation," *Phys. Rev. D*, vol. 95, no. 1, p. 015009, 2017. 78, 99

[139] T. You, "A Dynamical Weak Scale from Inflation," *JCAP*, vol. 09, p. 019, 2017. 78

[140] W. Tangarife, K. Tobioka, L. Ubaldi, and T. Volansky, "Relaxed Inflation," 6 2017. 78

[141] W. Tangarife, K. Tobioka, L. Ubaldi, and T. Volansky, "Dynamics of Relaxed Inflation," *JHEP*, vol. 02, p. 084, 2018. 78

[142] A. Hook and G. Marques-Tavares, "Relaxation from particle production," *JHEP*, vol. 12, p. 101, 2016. 78

[143] M. Son, F. Ye, and T. You, "Leptogenesis in Cosmological Relaxation with Particle Production," *Phys. Rev. D*, vol. 99, no. 9, p. 095016, 2019. 78

[144] N. Fonseca and E. Morgante, "Relaxion Dark Matter," *Phys. Rev. D*, vol. 100, no. 5, p. 055010, 2019. 78

[145] K. Kadota, U. Min, M. Son, and F. Ye, "Cosmological Relaxation from Dark Fermion Production," *JHEP*, vol. 02, p. 135, 2020. 78

[146] M. Ibe, Y. Shoji, and M. Suzuki, "Fast-Rolling Relaxion," *JHEP*, vol. 11, p. 140, 2019. 78

[147] N. Fonseca, E. Morgante, R. Sato, and G. Servant, "Axion fragmentation," *JHEP*, vol. 04, p. 010, 2020. 78

[148] N. Fonseca, E. Morgante, R. Sato, and G. Servant, "Relaxion Fluctuations (Self-stopping Relaxion) and Overview of Relaxion Stopping Mechanisms," *JHEP*, vol. 05, p. 080, 2020. [Erratum: JHEP 01, 012 (2021)]. 78

[149] N. Fonseca, E. Morgante, and G. Servant, "Higgs relaxation after inflation," *JHEP*, vol. 10, p. 020, 2018. 78

[150] R. D. Pisarski and F. Wilczek, "Remarks on the Chiral Phase Transition in Chromodynamics," *Phys. Rev. D*, vol. 29, pp. 338–341, 1984. 79, 105, 138, 145, 151

[151] E. Witten, "Cosmic Separation of Phases," *Phys. Rev. D*, vol. 30, pp. 272–285, 1984. 79

[152] C. Caprini, M. Hindmarsh, S. Huber, T. Konstandin, J. Kozaczuk, G. Nardini, J. M. No, A. Petiteau, P. Schwaller, G. Servant, and et al., "Science with the space-based interferometer elisa. ii: gravitational waves from cosmological phase transitions," *Journal of Cosmology and Astroparticle Physics*, vol. 2016, pp. 001–001, Apr 2016. 79, 95, 96

[153] C. Caprini, M. Chala, G. C. Dorsch, M. Hindmarsh, S. J. Huber, T. Konstandin, J. Kozaczuk, G. Nardini, J. M. No, K. Rummukainen, and et al., "Detecting gravitational waves from cosmological phase transitions with lisa: an update," *Journal of Cosmology and Astroparticle Physics*, vol. 2020, pp. 024–024, Mar 2020. 79, 95

[154] K. Kuroda, W.-T. Ni, and W.-P. Pan, "Gravitational waves: Classification, methods of detection, sensitivities and sources," *International Journal of Modern Physics D*, vol. 24, p. 1530031, Dec 2015. 79, 108

[155] W.-T. NI, "Astrod-gw: Overview and progress," *International Journal of Modern Physics D*, vol. 22, p. 1341004, Jan 2013. 79, 108

[156] W.-T. Ni, "Gravitational wave detection in space," *International Journal of Modern Physics D*, vol. 25, p. 1630001, Dec 2016. 79, 108

[157] L. Badurina, E. Bentine, D. Blas, K. Bongs, D. Bortoletto, T. Bowcock, K. Bridges, W. Bowden, O. Buchmueller, C. Burrage, and et al., "Aion: an atom interferometer observatory and network," *Journal of Cosmology and Astroparticle Physics*, vol. 2020, pp. 011–011, May 2020. 79, 108

[158] P. W. Graham, J. M. Hogan, M. A. Kasevich, S. Rajendran, and R. W. Romani, "Mid-band gravitational wave detection with precision atomic sensors," 2017. 79, 108

[159] M. Maggiore, C. V. D. Broeck, N. Bartolo, E. Belgacem, D. Bertacca, M. A. Bizouard, M. Branchesi, S. Clesse, S. Foffa, J. García-Bellido, and et al., "Science case for the einstein telescope," *Journal of Cosmology and Astroparticle Physics*, vol. 2020, pp. 050–050, Mar 2020. 79, 108

[160] D. Reitze, R. X. Adhikari, S. Ballmer, B. Barish, L. Barsotti, G. Billingsley, D. A. Brown, Y. Chen, D. Coyne, R. Eisenstein, M. Evans, P. Fritschel, E. D. Hall, A. Lazzarini, G. Lovelace, J. Read, B. S. Sathyaprakash, D. Shoemaker, J. Smith, C. Torrie, S. Vitale, R. Weiss, C. Wipf, and M. Zucker, "Cosmic explorer: The u.s. contribution to gravitational-wave astronomy beyond ligo," 2019. 79, 108

[161] S. Chatrchyan *et al.*, "Observation of a New Boson at a Mass of 125 GeV with the CMS Experiment at the LHC," *Phys. Lett. B*, vol. 716, pp. 30–61, 2012. 80

[162] "Measurement of the Higgs boson mass in the $H \to ZZ^* \to 4\ell$ and $H \to \gamma\gamma$ channels with $\sqrt{s}$=13TeV pp collisions using the ATLAS detector," 7 2017. 81

[163] R. Barbieri, "Electroweak theory after the first Large Hadron Collider phase," *Phys. Scripta T*, vol. 158, p. 014006, 2013. 81, 82

[164] S. P. Martin, "A Supersymmetry Primer," 81

[165] M. Quiros, "Introduction to extra dimensions," in *41st Rencontres de Moriond on Electroweak Interactions and Unified Theories*, 6 2006. 81

[166] R. Contino, "Tasi 2009 lectures: The higgs as a composite nambu-goldstone boson," 2010. 81

[167] M. Dine, "TASI lectures on the strong CP problem," in *Theoretical Advanced Study Institute in Elementary Particle Physics (TASI 2000): Flavor Physics for the Millennium*, 6 2000. 86

[168] A. Hook, "Tasi lectures on the strong cp problem and axions," 2018. 86

[169] H. Beauchesne, E. Bertuzzo, and G. Grilli di Cortona, "Constraints on the relaxion mechanism with strongly interacting vector-fermions," *JHEP*, vol. 08, p. 093, 2017. 87, 106, 139

[170] A. Mazumdar and G. White, "Review of cosmic phase transitions: their significance and experimental signatures," *Rept. Prog. Phys.*, vol. 82, no. 7, p. 076901, 2019. 88, 93, 94, 95

[171] A. D. Linde, "Decay of the False Vacuum at Finite Temperature," *Nucl. Phys. B*, vol. 216, p. 421, 1983. [Erratum: Nucl.Phys.B 223, 544 (1983)]. 89, 91, 92, 130

[172] S. R. Coleman, "The Fate of the False Vacuum. 1. Semiclassical Theory," *Phys. Rev. D*, vol. 15, pp. 2929–2936, 1977. [Erratum: Phys.Rev.D 16, 1248 (1977)]. 91, 92, 130

[173] M. Breitbach, J. Kopp, E. Madge, T. Opferkuch, and P. Schwaller, "Dark, cold, and noisy: constraining secluded hidden sectors with gravitational waves," *Journal of Cosmology and Astroparticle Physics*, vol. 2019, pp. 007–007, Jul 2019. 93

[174] H.-K. Guo, K. Sinha, D. Vagie, and G. White, "Phase transitions in an expanding universe: Stochastic gravitational waves in standard and non-standard histories," 2020. 93

[175] J. R. Espinosa, T. Konstandin, J. M. No, and G. Servant, "Energy budget of cosmological first-order phase transitions," *Journal of Cosmology and Astroparticle Physics*, vol. 2010, pp. 028–028, Jun 2010. 93, 96

[176] J. Ellis, M. Lewicki, J. M. No, and V. Vaskonen, "Gravitational wave energy budget in strongly supercooled phase transitions," *Journal of Cosmology and Astroparticle Physics*, vol. 2019, pp. 024–024, Jun 2019. 93, 95, 97

[177] A. J. Helmboldt, J. Kubo, and S. van der Woude, "Observational prospects for gravitational waves from hidden or dark chiral phase transitions," *Phys. Rev. D*, vol. 100, no. 5, p. 055025, 2019. 93, 96, 105, 107, 108, 115

[178] A. Kosowsky, M. S. Turner, and R. Watkins, "Gravitational radiation from colliding vacuum bubbles," *Phys. Rev. D*, vol. 45, pp. 4514–4535, 1992. 94

[179] C. Caprini and D. G. Figueroa, "Cosmological Backgrounds of Gravitational Waves," *Class. Quant. Grav.*, vol. 35, no. 16, p. 163001, 2018. 95

[180] A. J. Helmboldt, J. Kubo, and S. van der Woude, "Observational prospects for gravitational waves from hidden or dark chiral phase transitions," *Physical Review D*, vol. 100, Sep 2019. 95

[181] X. Wang, F. P. Huang, and X. Zhang, "Phase transition dynamics and gravitational wave spectra of strong first-order phase transition in supercooled universe," *Journal of Cosmology and Astroparticle Physics*, vol. 2020, p. 045045, May 2020. 95

[182] X. Wang, F. P. Huang, and X. Zhang, "The energy budget and the gravitational wave spectra beyond the bag model," 2020. 95

[183] M. Hindmarsh, S. J. Huber, K. Rummukainen, and D. J. Weir, "Numerical simulations of acoustically generated gravitational waves at a first order phase transition," *Physical Review D*, vol. 92, Dec 2015. 96

[184] J. Ellis, M. Lewicki, and J. M. No, "On the Maximal Strength of a First-Order Electroweak Phase Transition and its Gravitational Wave Signal," *JCAP*, vol. 04, p. 003, 2019. 96, 97

[185] B. Batell, G. F. Giudice, and M. McCullough, "Natural Heavy Supersymmetry," *JHEP*, vol. 12, p. 162, 2015. 98

[186] J. L. Evans, T. Gherghetta, N. Nagata, and Z. Thomas, "Naturalizing Supersymmetry with a Two-Field Relaxion Mechanism," *JHEP*, vol. 09, p. 150, 2016. 98

[187] J. L. Evans, T. Gherghetta, N. Nagata, and M. Peloso, "Low-scale D -term inflation and the relaxion mechanism," *Phys. Rev. D*, vol. 95, no. 11, p. 115027, 2017. 98

[188] B. Batell, M. A. Fedderke, and L.-T. Wang, "Relaxation of the Composite Higgs Little Hierarchy," *JHEP*, vol. 12, p. 139, 2017. 98

[189] N. Fonseca, B. Von Harling, L. De Lima, and C. S. Machado, "A warped relaxion," *JHEP*, vol. 07, p. 033, 2018. 98

[190] K. Choi and S. H. Im, "Realizing the relaxion from multiple axions and its UV completion with high scale supersymmetry," *JHEP*, vol. 01, p. 149, 2016. 98

[191] D. E. Kaplan and R. Rattazzi, "Large field excursions and approximate discrete symmetries from a clockwork axion," *Phys. Rev. D*, vol. 93, no. 8, p. 085007, 2016. 98

[192] G. F. Giudice and M. McCullough, "A Clockwork Theory," *JHEP*, vol. 02, p. 036, 2017. 98

[193] N. Craig, I. Garcia Garcia, and D. Sutherland, "Disassembling the Clockwork Mechanism," *JHEP*, vol. 10, p. 018, 2017. 98

[194] K. Choi, H. Kim, and T. Sekiguchi, "Dynamics of the cosmological relaxation after reheating," *Phys. Rev. D*, vol. 95, no. 7, p. 075008, 2017. 99

[195] A. Banerjee, H. Kim, and G. Perez, "Coherent relaxion dark matter," *Phys. Rev. D*, vol. 100, no. 11, p. 115026, 2019. 99, 103

[196] S. Hannestad, "What is the lowest possible reheating temperature?," *Phys. Rev. D*, vol. 70, p. 043506, 2004. 104

[197] A. Hebecker, J. Jaeckel, F. Rompineve, and L. T. Witkowski, "Gravitational waves from axion monodromy," *Journal of Cosmology and Astroparticle Physics*, vol. 2016, pp. 003–003, Nov 2016. 105

[198] J. Brown, W. Cottrell, G. Shiu, and P. Soler, "Tunneling in axion monodromy," *Journal of High Energy Physics*, vol. 2016, Oct 2016. 105

[199] Z. Zhou, J. Yan, A. Addazi, Y.-F. Cai, A. Marciano, and R. Pasechnik, "Probing new physics with multi-vacua quantum tunnelings beyond standard model through gravitational waves," 2020. 105

[200] O. Antipin and M. Redi, "The Half-composite Two Higgs Doublet Model and the Relaxion," *JHEP*, vol. 12, p. 031, 2015. 106, 139

[201] D. Barducci, S. De Curtis, M. Redi, and A. Tesi, "An almost elementary Higgs: Theory and Practice," *JHEP*, vol. 08, p. 017, 2018. 106, 139

[202] P. Amaro-Seoane, S. Aoudia, S. Babak, P. Bintruy, E. Berti, A. Boh, C. Caprini, M. Colpi, N. J. Cornish, K. Danzmann, J.-F. Dufaux, J. Gair, O. Jennrich, P. Jetzer, A. Klein, R. N. Lang, A. Lobo, T. Littenberg, S. T. McWilliams, G. Nelemans, A. Petiteau, E. K. Porter, B. F. Schutz, A. Sesana, R. Stebbins, T. Sumner, M. Vallisneri, S. Vitale, M. Volonteri, and H. Ward, "elisa: Astrophysics and cosmology in the millihertz regime," 2012. 108

[203] Y. Aoki *et al.*, "Light composite scalar in eight-flavor QCD on the lattice," *Phys. Rev. D*, vol. 89, p. 111502, 2014. 109

[204] Y. Aoki *et al.*, "Light flavor-singlet scalars and walking signals in $N_f = 8$ QCD on the lattice," *Phys. Rev. D*, vol. 96, no. 1, p. 014508, 2017. 109

[205] T. Appelquist *et al.*, "Strongly interacting dynamics and the search for new physics at the LHC," *Phys. Rev. D*, vol. 93, no. 11, p. 114514, 2016. 109

[206] T. Appelquist *et al.*, "Nonperturbative investigations of SU(3) gauge theory with eight dynamical flavors," *Phys. Rev. D*, vol. 99, no. 1, p. 014509, 2019. 109

[207] Z. Fodor, K. Holland, J. Kuti, D. Nogradi, and C. H. Wong, "Can a light Higgs impostor hide in composite gauge models?," *PoS*, vol. LATTICE2013, p. 062, 2014. 109

[208] Z. Fodor, K. Holland, J. Kuti, S. Mondal, D. Nogradi, and C. H. Wong, "Toward the minimal realization of a light composite Higgs," *PoS*, vol. LATTICE2014, p. 244, 2015. 109

[209] Z. Fodor, K. Holland, J. Kuti, S. Mondal, D. Nogradi, and C. H. Wong, "Status of a minimal composite Higgs theory," *PoS*, vol. LATTICE2015, p. 219, 2016. 109

[210] R. C. Brower, A. Hasenfratz, C. Rebbi, E. Weinberg, and O. Witzel, "Composite Higgs model at a conformal fixed point," *Phys. Rev. D*, vol. 93, no. 7, p. 075028, 2016. 109

[211] A. Athenodorou, E. Bennett, G. Bergner, and B. Lucini, "Recent results from SU(2) with one adjoint Dirac fermion," *Int. J. Mod. Phys. A*, vol. 32, no. 35, p. 1747006, 2017. 109

[212] T. A. Ryttov and F. Sannino, "Conformal Windows of SU(N) Gauge Theories, Higher Dimensional Representations and The Size of The Unparticle World," *Phys. Rev. D*, vol. 76, p. 105004, 2007. 110

[213] T. Appelquist *et al.*, "Linear Sigma EFT for Nearly Conformal Gauge Theories," *Phys. Rev. D*, vol. 98, no. 11, p. 114510, 2018. 110

[214] Y. Meurice, "Linear sigma model for multiflavor gauge theories," *Phys. Rev. D*, vol. 96, no. 11, p. 114507, 2017. 110, 135

[215] M. Blennow, "Prospects for cosmic neutrino detection in tritium experiments in the case of hierarchical neutrino masses," *Phys. Rev. D*, vol. 77, p. 113014, 2008. 113, 118

[216] Y. F. Li, Z.-z. Xing, and S. Luo, "Direct Detection of the Cosmic Neutrino Background Including Light Sterile Neutrinos," *Phys. Lett. B*, vol. 692, pp. 261–267, 2010. 113, 118

[217] A. Bhattacharyya, "On a measure of divergence between two statistical populations defined by their probability distributions," *Bull. Calcutta Math. Soc.*, vol. 35, pp. 99–109, 1943. 119

[218] I. Esteban, M. C. Gonzalez-Garcia, M. Maltoni, I. Martinez-Soler, and T. Schwetz, "Updated fit to three neutrino mixing: exploring the accelerator-reactor complementarity," *JHEP*, vol. 01, p. 087, 2017. 119

[219] P. Agrawal, M. Blanke, and K. Gemmler, "Flavored dark matter beyond Minimal Flavor Violation," *JHEP*, vol. 10, p. 072, 2014. 124

[220] M. Blanke, S. Das, and S. Kast, "Flavoured Dark Matter Moving Left," *JHEP*, vol. 02, p. 105, 2018. 124

[221] J. Gasser and H. Leutwyler, "Chiral Perturbation Theory: Expansions in the Mass of the Strange Quark," *Nucl. Phys. B*, vol. 250, pp. 465–516, 1985. 136

[222] D. Curtin, P. Meade, and H. Ramani, "Thermal resummation and phase transitions," 2016. 137, 138

[223] Y. Bai, A. J. Long, and S. Lu, "Dark quark nuggets," *Physical Review D*, vol. 99, Mar 2019. 137

[224] A. Banerjee, H. Kim, O. Matsedonskyi, G. Perez, and M. S. Safronova, "Probing the Relaxed Relaxion at the Luminosity and Precision Frontiers," *JHEP*, vol. 07, p. 153, 2020. 143

[225] J. Wirstam, "Chiral symmetry in two color QCD at finite temperature," *Phys. Rev. D*, vol. 62, p. 045012, 2000. 145

[226] E. Brézin, J. C. Le Guillou, and J. Zinn-Justin, "Discussion of critical phenomena for general n-vector models," *Phys. Rev. B*, vol. 10, pp. 892–900, Aug 1974. 145, 147, 148, 149, 151

[227] K. G. Wilson, "Renormalization group and critical phenomena. 1. Renormalization group and the Kadanoff scaling picture," *Phys. Rev. B*, vol. 4, pp. 3174–3183, 1971. 145

[228] K. G. Wilson, "Feynman graph expansion for critical exponents," *Phys. Rev. Lett.*, vol. 28, pp. 548–551, 1972. 145

[229] K. G. Wilson and J. B. Kogut, "The Renormalization group and the epsilon expansion," *Phys. Rept.*, vol. 12, pp. 75–199, 1974. 145

[230] E. Brezin, "Wilson's renormalization group: a paradigmatic shift," 2 2014. 145

[231] P. Bak, S. Krinsky, and D. Mukamel, "First-order transitions, symmetry, and the ϵ expansion," *Phys. Rev. Lett.*, vol. 36, pp. 52–55, Jan 1976. 145, 146, 147

[232] "Amazon.com: Quantum field theory: An integrated approach (9780691149080): Fradkin, eduardo: Books." https://www.amazon.com/-/es/Eduardo-Fradkin/dp/0691149089. 147

[233] H. H. Iacobson and D. J. Amit, "First order transitions induced by fluctuations in general 4-theories," *Annals of Physics*, vol. 133, no. 1, pp. 57 – 78, 1981. 147, 148, 149, 150, 151

[234] M. Arteaga, E. Bertuzzo, C. Caniu Barros, and Z. Tabrizi, "Operators from flavored dark sectors running to low energy," *Phys. Rev. D*, vol. 99, no. 3, p. 035022, 2019.

[235] P. W. Graham, D. E. Kaplan, and S. Rajendran, "Cosmological Relaxation of the Electroweak Scale," *Phys. Rev. Lett.*, vol. 115, no. 22, p. 221801, 2015.

[236] D. Barducci, E. Bertuzzo, and M. Arteaga-Tupia, "Gravitational tests of electroweak relaxation," 2020.